Alma Mater Studiorum · Università di Bologna

Scuola di Scienze
Dipartimento di Fisica e Astronomia
Laurea Magistrale in Astrofisica e Cosmologia

Updating Jupiter's Shape integrating novel gravity experiment results and radio occultation measurements.

Relatore:
Chiar.mo Prof.
Paolo Tortora

Correlatori:
Prof. Marco Zannoni
Dott. Andrea Caruso

Presentata da:
Matteo Fonsetti

Anno Accademico 2023/2024

ABSTRACT

This dissertation presents a methodology for precisely determining the shape of Jupiter, integrating the most updated gravity results collected by the Juno probe and radio occultation measurements obtained by Pioneer 10, Pioneer 11, Voyager 1, and Voyager 2 probes, along with recent findings from Juno. Our analysis includes the cloud-level zonal wind profiles collected from the Hubble Space Telescope's Wide Field Camera 3 in the years 2009, 2012, 2015, 2016, 2017, and 2019, and from Voyager 2 in 1979. Initially, the study estimates the dynamical height, accounting for the contributions of gravitational zonal harmonics and the perturbation effects introduced by cloud-level zonal winds. Gravitational harmonics analysis highlights the significant impact of J_2 and J_4 coefficients on Jupiter's shape, with minimal contribution from odd zonal harmonics. Cloud-level winds' variation effects on the shape are evaluated, as well as the analysis of the effects due to uncertainties associated with the gravitational coefficients, zonal winds, and the planet's polar radius and rotation rate. In the second part of this work, we perform a comparison between the calculated shape and radio occultation measurements, to estimate the polar radius from the results obtained through radio occultations. We find a promising improvement in the consistency between the estimated dynamical height and radio occultations, with a root mean square error of the calculated dynamical height approximately 3 km lower with respect to the value currently accepted in literature, although non-negligible uncertainties associated with radio occultations and the internal models employed to describe Jupiter's dynamics persist.

SOMMARIO

Questa tesi propone un metodo per determinare con precisione la shape di Giove, integrando i risultati più recenti degli esperimenti di gravità della sonda Juno e le misurazioni di radio occultazione effettuate dalle sonde Pioneer 10, Pioneer 11, Voyager 1 e Voyager 2, insieme ai risultati preliminari raccolti dalla Juno stessa. L'analisi include le misurazioni dei venti zonali, effettuate con il Wide Field Camera 3 del telescopio spaziale Hubble negli anni 2009, 2012, 2015, 2016, 2017 e 2019, così come i dati raccolti da Voyager 2 nel 1979. Inizialmente, abbiamo stimato la dynamical height considerando gli effetti delle armoniche gravitazionali e dei venti zonali, analizzando in seguito i contributi relativi ai singoli coefficienti, ai modelli di vento, alle incertezze sul raggio polare e a quelle sul periodo rotazionale del pianeta. L'analisi delle armoniche gravitazionali ha evidenziato l'importanza dei coefficienti J_2 e $J4$, mentre l'influenza delle armoniche dispari risulta trascurabile. Nella seconda parte del lavoro, abbiamo confrontato la dynamical height con i risultati ottenuti delle radio occultazioni e abbiamo effettuato una nuova stima del raggio polare che tiene conto sia dei risultati delle radio occultazioni che degli esperimenti di gravità, includendo infine l'analisi degli effetti derivanti dalle incertezze associate alle armoniche gravitazionali J_2 e $J4$ e al profilo di vento da noi utilizzato. La nuova stima ottenuta sembra rappresentare un promettente miglioramento nella consistenza tra i risultati degli esperimenti di gravità e quelli di radio occultazione, rispetto a quanto ottenuto in letteratura, con un RMSE che mostra una riduzione di circa 3 km rispetto al valore finora accettato, anche se persistono incertezze non trascurabili associate alle occultazioni radio e ai modelli interni utilizzati per descrivere la dinamica di Giove.

Contents

1 Introduction **1**

2 Introducing Planet Jupiter **3**
2.1 Overview . . . 4
2.2 Atmosphere . . . 6
2.2.1 Shallow Models . . . 7
2.2.2 Deep Models . . . 8
2.3 Exploration of Jupiter . . . 9
2.3.1 Pioneer 10 . . . 10
2.3.2 Pioneer 11 . . . 12
2.3.3 Voyager 1 . . . 14
2.3.4 Voyager 2 . . . 15
2.3.5 Juno . . . 17
2.3.6 Hubble Space Telescope . . . 18

3 Theoretical background **19**
3.1 Shape Calculation of a Fluid, Rotating Celestial Body . . . 20
3.2 Measurement of Jupiter's gravity field . . . 23
3.3 Zonal Wind Models . . . 25
3.3.1 The Global Method . . . 25
3.3.2 The Datasets . . . 26
3.3.3 Some Preliminary Observations . . . 27
3.4 Planetary Radio Occultations . . . 30
3.4.1 Geometry of a Radio Occultation . . . 30
3.4.2 Frequency Shifts in Radio Occultations . . . 31
3.4.3 From Refractivity to Pressure Profile . . . 32
3.4.4 Sources of Uncertainties in Radio Occultations . . . 34

4 Shape Determination Of Jupiter **37**
4.1 Shape Computation - Rotating Solid Body . . . 38
4.1.1 Effects of Gravitational Harmonics . . . 40
4.2 Shape Computation - Effect of Cloud-Level Winds . . . 42
4.3 Sources of Uncertainty . . . 44
4.3.1 Polar Radius . . . 44

4.3.2 Cloud-level Winds . . . 45
4.3.3 Rotation Rate . . . 49
4.4 Shape Update including Radio Occultations . . . 50
4.5 Sources of Uncertainty . . . 52
4.5.1 Effects of Gravitational Harmonics . . . 52
4.5.2 Effect of Cloud-level Winds . . . 53

5 Conclusions **55**
5.1 Future assessments . . . 56

A Derivation of the Taylor-Proudman Theorem **59**

B Our Results **61**

References **75**

List of Tables

3.1 Datasets used in this thesis 26

4.1 Bulk parameters used in our study. 38
4.2 Jupiter's gravity harmonic coefficients (unnormalized and with reference radius 71492 km). The J2 coefficient includes a tidal component predicted from interior models and, according to Durante et al. (2020), is currently estimated at $6.72\text{x}10^{-8}$ with uncertainties of 3σ. 38
4.3 Gravitational coefficients' combinations chosen for our analysis. 40
4.4 Radio occultation data available for this study. 51

B.1 Our results. 62
B.2 Our results. 63
B.3 Our results. 64
B.4 Our results. 65
B.5 Our results. 66
B.6 Our results. 67
B.7 Our results. 68
B.8 Our results. 69
B.9 Our results. 70
B.10 Our results. 71
B.11 Our results. 72
B.12 Our results. 73

List of Figures

2.1 Juno's Great Red Spot and atmospheric dynamical features. Credits: NASA. . . . 3
2.2 Image of Jupiter taken by Hubble Space Telescope. Credits: NASA, ESA. 5
2.3 Jupiter's zones and belts. The equatorial prograde jet is visible above the GRS. The image also reveals a rare wave structure just north of the planet's equator. Credits: NASA, HST. 6
2.4 The Great Red Spot, Jupiter's most renowned feature. The first confirmed observation of this storm dates back to 1831[1], indicating that this atmospheric phenomenon is at least two centuries old. Image obtained by Juno. Credits: NASA. 7
2.5 Jupiter's equatorial prograde jet. Image obtained by Juno. Credits: NASA 8
2.6 An excerpt from Galileo's Sidereus Nuncius, showing Jupiter and three of its moons. Source: International Astronomical Union. 9
2.7 Pioneer 10 image of Jupiter taken at a distance of 2,965,000 km produced by assembling on Earth successive scans captured by the probe. Image taken by Smithsonian National Air and Space Museum. Credits: NASA. 11
2.8 Jupiter's crescent-shape, termed as the "Sunrise on Jupiter". Credits: NASA. . . . 11
2.9 Jupiter's northern polar region as observed by Pioneer 11 from an altitude of 1,079,000 km. Credits: NASA. 12
2.10 The illustration of the plaque installed onboard Pioneer 10 and Pioneer 11 probes. From top to bottom, and from left to right, it depicts the hyperfine transition of neutral hydrogen, the Sun and galactic landmarks, the Solar System with the Earth location flagged as the probe's departure point, the silhouette of the spacecraft, and the figures of a man and a woman. Credits: NASA. 13
2.11 Illustration depicting the Pioneer program. Credits: NASA. 13
2.12 First observation of Jupiter's planetary rings. Credits: NASA JPL. 14
2.13 Eruption plume of the volcano Loki rising over 160 km over the limb of Io. Credits: NASA. 14
15figure.caption.17
2.15 A color mosaic of Europa. Bright areas are probably ice deposits, while shaded areas could indicate either rocky terrain or patches with a less uniform distribution of ice. Credits: NASA. 15
2.16 The Voyager Golden Record. Credits: NASA. 16
2.17 One of the pictures contained in Voyager Golden Records, representing a book of Newton's System of the World, published into the author's Mathematical Principles of Natural Philosophy. Image taken by the NASA/JPL Voyager database. 16

2.18 Cows graze in front of the multiple radio dishes of Canberra's Deep Space Communication Complex. Credits: NASA/JPL-Caltech. 17
2.19 WFC3 preparing for its departure aboard STS-125. Credits: NASA. 18

3.1 A geoid and its perturbation due to a zonal jet with eastward velocity $V_{wind} \neq 0$. Image taken from the method described by Lindal, Sweetnam, and V. Eshleman (1985). 23
3.2 Scheme of a gravity experiment. Image taken from spaceflight101.com and re-edited. 24
3.3 An example of how maps are organized into latitude strips in the 1D correlation method. In this case, the map has also been divided into two hemispheres to optimize the observation time. Image taken by J. Tollefson et al. (2017). 25
3.4 Left: Comparison of the average Zonal Wind Profiles (ZWPs) from datasets collected by Hubble in 2009 and 2012. Right: Difference between the compared ZWPs (black) and total RMS (red). Differences outside the red region are significant. . . 27
3.5 Same as Figure 3.4, but considering HST 2009 and HST 2016 datasets. 28
3.6 Same as Figure 3.4, but considering HST 2012 and HST 2016 datasets. 28
3.7 Left: Comparison between 2009 ZWPs for different hemispheres. Right: Difference between the compared zonal wind profiles (black) and total RMS (red). 29
3.8 Same as Figure 3.7, but considering the 2012 dataset. 29
3.9 Geometry of a radio occultation experiment. Image from AJ Kliore et al. (2004). . 31
3.10 Block-diagram of a one-way radio occultation experiment. Image from Withers (2010). 35

4.1 The 1-bar equipotential shape of Jupiter obtained in our study and by Dustin R Buccino et al. (2020) in the approximation of a rotating solid body (left) and the corresponding residuals (right). The average difference is of the order of the meter over 10^4 km, corresponding to a relative difference of 10^{-6}. This discrepancy arises from digit approximation choices. Overall, this comparison affirms the correctness of our computational method. 39
4.2 Difference between the shape computed including J_4 and that of a reference ellipsoid. We can appreciate the symmetry relative to the equator, a characteristic of the even-numbered gravity coefficients greater than J_2. 40
4.3 Effects of J_6. The difference is between the shape up to J_6 and the shape up to J_4. 41
4.4 Effects of J_8 (left), J_{10} (centre), and J_{12} (right). For each panel, the difference is computed between the shape up to the J_n term and that up to the term J_{n-2}. . . . 41
4.5 Jupiter's 2019 zonal wind profile as measured by Hubble's Wide Field Camera 3 (azure) and its associated uncertainty (light grey). 42
4.6 Our obtained dynamical height considering Hubble's 2019 zonal wind profile. The black dashed line represents the reference level which corresponds to the shape computed assuming rigid body rotation only. 43
4.7 Resulting shapes considering the average polar radius R_p (green), and a polar radius equal to R_p - 10 km and R_p + 10 km, red and blue, respectively; black horizontal line represents a difference of 10 km. 44
4.8 Differences in dynamical heights due to the uncertainty associated with the polar radius. The black dashed line represents the reference level, derived using the average value of R_p. This value is subtracted from the results obtained with R_p - 10 km (red) and R_p + 10 km (blue), respectively. The green curve represents the maximum difference between the two dynamical heights calculated using R_p + 10 km and R_p - 10 km. 45

4.9 Dynamical height computed in Section 4.2 (azure) with its associated uncertainty (light grey). . . . 46
4.10 Results on the dynamical heights obtained by considering all the zonal wind profiles presented in Section 3.3.2. We can observe that the dynamical height associated with Voyager 2 deviates more significantly from the others. . . . 46
4.11 Differences in shape considering the wind models presented in Section 3.3.2. The dashed black line represents the reference profile obtained by averaging all the calculated shapes . . . 47
4.12 Left: Same as Figure 4.11, but considering only Hubble dataset. Right: Difference between lower and upper limit discrepancies. . . . 47
4.13 Analysis of the RMSE profiles associated with Voyager 2 (blue) and HST (red) datasets. The two RMSE profiles are similar. On the bottom-mid are reported the average RMSE values. . . . 48
4.14 Difference in the dynamical height due to the hypothetical uncertainty in the rotation rate. The red curve is obtained by subtracting the dynamical height profile obtained considering the nominal rotation rate from the dynamical height profile obtained considering the hypothetical rotation rate. . . . 49
4.15 Overall shape inferred from radio occultations. Colored dots represent the radii obtained from occultation measurements of Pioneer 10 (P10), Pioneer 11 (P11), Voyager 1 (V1), Voyager 2 (V2) and Juno at 100 mbar. The 'PJ53' and 'PJ54' flags for Juno mark perijove 53 and perijove 54, respectively. . . . 50
4.16 Dynamical height considering Hubble 2019 results. Colored points represent radio occultation data. Horizontal bars represent the uncertainties associated with radio occultations, as reported in Table 4.4. . . . 51
4.17 Variations in the shape considering the uncertainties on the gravity coefficients listed in Table 4.2. Panel A): Shape computed using $J_2 + \Delta J_2$ minus the shape obtained considering the average J_2. Panel B): Same as A), except we used $J_2 - \Delta J_2$ instead of $J_2 + \Delta J_2$. Panel C): Shape computed using $J_4 + \Delta J_4$ minus the shape obtained considering the average J_4. The J_2 coefficient is set to its average value. Panel D): Same as C), except we used $J_4 - \Delta J_4$ instead of $J_4 + \Delta J_4$. Points corresponding poles equator are highlighted in azure and green, respectively, and flagged with arrows of the same color. . . . 52
4.18 Dynamical height considering Hubble 2019 results (azure) and total RMSE associated with each latitude (light gray region). Colored points represent radio occultation data. Horizontal bars represent the uncertainties associated with radio occultations, as reported in Table 4.4. . . . 53

5.1 Jupiter's South Pole and Vincent Van Gogh Starry Night. . . . 58

CHAPTER 1

Introduction

Named after the Roman god of sky and thunder, Jupiter is the most massive planet of the Solar System. As the first planet to form, Jupiter was probably born much closer to the Sun before migrating to its current position about four billion years ago, scattering asteroids and comets with its gravity in the process. Some of those asteroids and comets collided with early Earth, possibly bringing water in the process, the key ingredient for life as we know it. Many of the exoplanets that have been discovered are Jupiter-like worlds close to their stars, reinforcing the idea that the gas giant may have moved from its original position. An important aspect of gas giants' physics revolves around determining their precise shape, as this factor significantly impacts the accuracy of radio occultation experiments. Radio occultations stand as a widely employed technique in interplanetary missions which aim at delving into the atmospheres of celestial bodies. Advancing our understanding of Jupiter's shape is of primary importance for refining the precision of radio occultations. This, in turn, would lead to a more accurate characterization of Jupiter's atmosphere and enhanced orbit determination. Furthermore, in the realm of fundamental physics, deepening our grasp on Jupiter's shape enables us to better constrain interior models, thereby enhancing our comprehension of the dynamics underlying gas giants and other celestial bodies, including Earth. This would also provide valuable insights into the formation of our stellar system and, by extension, similar planetary systems, as well as facilitate the characterization of exoplanetary atmospheres. Jupiter's shape closely resembles that of an oblate spheroid, primarily influenced by its rotation rate and internal density distribution, the latter manifested in the planet's gravity field. Thanks to NASA's Juno mission, we now have access to high-precision measurements of the giant's gravity field, along with observations of zonal winds, enabling us to achieve accurate calculations. The most recent studies in the field have been published by Dustin R Buccino et al. (2020) and Eli Galanti, Yohai Kaspi, and Tristan Guillot (2023). In both studies, a correlation between the dynamical height computed using gravity experiments and the results suggested by radio occultation experiments has not been found. In, particular, as discussed in Eli Galanti, Yohai Kaspi, and Tristan Guillot (2023), among the six available radio occultation datasets analyzed, only two exhibited a significant correlation. The remaining four not only fell entirely outside the confidence interval but also showed an opposing sign compared to that of the dynamical height, indicating the presence of other factors that may contribute to the mismatch. In this study, we try to mitigate this uncertainty by leveraging newly available data on Jupiter's gravity field, cloud-level zonal winds, and radio occultations. We aim to provide an updated estimate that can serve as a new checkpoint, from which, through the results of forthcoming occultations, a solution that is consistent with both gravity measurements and radio occultations can finally be achieved.

This thesis is organized as follows:

- Chapter 2 provides an introductory overview of Jupiter, presenting its general characteristics, and atmospheric dynamics, and offering a review of past and ongoing scientific missions dedicated to exploring the gas giant;
- Chapter 3 delves into the necessary theoretical principles to derive the physical parameters that will be used in our computational approach, as well as the methodologies employed for their investigation;
- Chapter 4 illustrates our proposed method to compute the shape of Jupiter including the results of the gravity experiments, radio occultations, and zonal winds, as well as the analysis of the correspondent uncertainties;
- Chapter 5 presents the conclusions drawn from our study, along with avenues for future research.

This work was carried out at CIRI Aerospace in Forlì.

CHAPTER 2

Introducing Planet Jupiter

This chapter provides a concise introduction to Jupiter focusing on its atmosphere and its exploration. In Section 2.1 we present some basic foundational concepts regarding Jupiter's origin and the conditions necessary for the development of an atmosphere on a celestial body. Jupiter's atmosphere bears striking resemblance to the primordial nebula from which the Solar System formed, as well as to many of the exoplanets discovered in recent years. This makes the Jovian system particularly intriguing in the context of studying the origin of the Solar System, and by extension, other similar stellar systems. Jupiter's atmosphere features a complex array of colorful bands, powerful jets, and geometric storms boasting winds reaching speeds of up to 150 m/s. These winds, known as *zonal winds* or *cloud-level winds*, play a crucial role in shaping the gas giant's shape. In Section 2.2, we provide a brief overview of the two major macro-models aimed at explaining the intriguing features that characterize Jupiter's atmosphere. Finally, Section 2.3 delves into interplanetary exploration, where we introduce past and ongoing scientific missions that have explored the Jovian system, and whose data have been included in this dissertation.

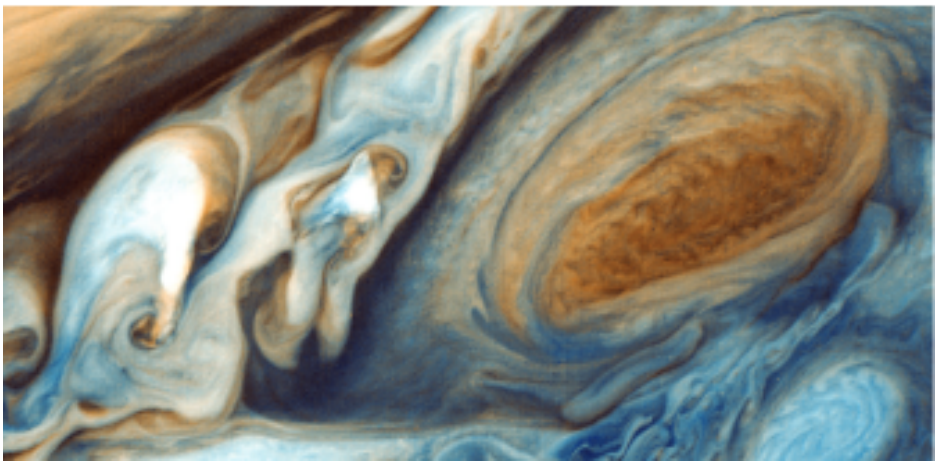

Figure 2.1. Juno's Great Red Spot and atmospheric dynamical features. Credits: NASA.

2.1 Overview

Jupiter is the fifth planet from the Sun and the largest planet in the Solar System.
Its mass is estimated to be 1,898.13 $\times$ 10^{24}, more than two times that of all the other planets combined[1], a feature which made him play a key role in shaping our primordial stellar system. The formation of Jupiter, along with all the other gas giants, poses a long-standing challenge, and as of now, there is still no theory that can provide a fully consistent framework for how the planet formed. One of the most promising models, known as the 'Grand Tack Hypothesis', proposes a scenario in which Jupiter may have formed near the ice line, at a distance of $\sim$ 3.5 AU from the Sun before migrating inward to 1.5 AU where capturing Saturn in an orbital resonance would have made him reverse his course and stabilize near its current orbit at 5.2 AU[2].

The most peculiar feature of Jupiter is its atmosphere, the largest in the Solar System, home to rare and not yet fully understood turbulent phenomena. Here we briefly present the essential reason behind the atmospheric compositions of Jupiter, as illustrated in Sanchez-Lavega (2010). Planetary atmospheres can form when the gravitational force of a celestial body is high enough to retain the gases against a variety of processes that favor their escape, the main of which, according to Sanchez-Lavega (2010), are thermal (or Jeans) escape, non-thermal (or photochemical) escape, hydrodynamical escape, geometrical escape, and impacts[3].
In order, for a planet, to retain an atom or a molecule, it must hold that:

$$\frac{GM_p}{R_p} \geq k_B T \tag{2.1}$$

where M_p and R_p are the mass and the radius of the celestial body, k_B is the Boltzmann's constant, and T is the absolute gas temperature. The escape velocity v_{esc} for an atom or molecule - i.e., the velocity needed to abandon the body's gravitational field - is defined as

$$v_{esc} = \sqrt{\frac{2GM_p}{R_p}} \tag{2.2}$$

while the atom or molecule kinetic energy, represented by the thermal velocity, v_{th}, is given by

$$v_{th} = \sqrt{\frac{2k_B T}{m_a}} \tag{2.3}$$

Equations (2.1), (2.2), and (2.3) together, contain the information needed to explain the light element abundances observed in the gas giants' atmospheres. Lighter and more abundant elements, such as hydrogen and helium, reach higher thermal velocities with respect to heavier ones. Consequently, according to Eq. (2.1), only massive, cold planets can effectively retain these elements. These atmospheres, aptly termed *primary atmospheres*, sustain chemical abundances of hydrogen and helium around 90% and 10%, respectively[4], offering valuable insights into the conditions prevalent in the primordial nebula from which the Solar System originated. Nevertheless, as presented in S. Atreya et al. (2003), carbon and nitrogen are enriched by a factor 2-4 relative to the Sun, and the noble gases (Ne, Ar, Kr, and Xe) are present with abundances within a factor 10 to the solar composition, this complicates the detailed modeling of the formation of these atmospheres.

[1] cf. https://science.nasa.gov/jupiter/.
[2] cf. http://earthmoonsystem.com/papers/dbe_Solar_System_Formation.pdf?view=Fit&scrollbar=1&toolbar=1&navpanes=1&pagemode=bookmarks.
[3] cf. https://www.researchgate.net/publication/328562725_An_Introduction_to_Planetary_

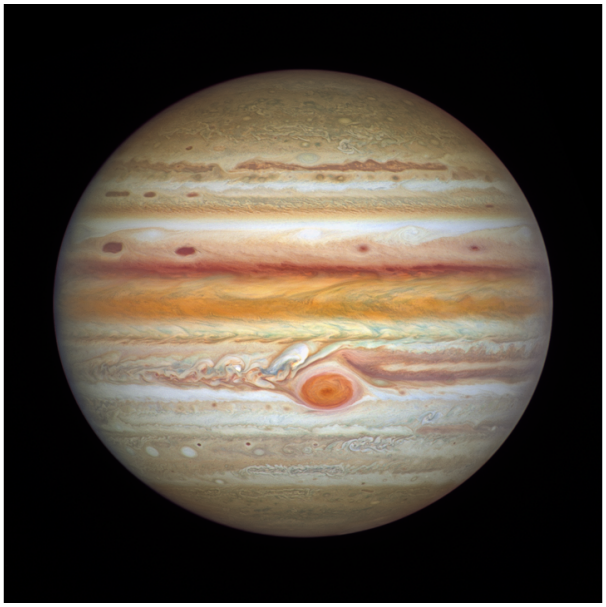

Figure 2.2. Image of Jupiter taken by Hubble Space Telescope.
Credits: NASA, ESA.

Constructing a model that accurately describes Jupiter's internal conditions poses a significant challenge due to the limited availability of comprehensive laboratory data on the properties of hydrogen and helium at the extreme temperatures and pressures found near the planet's core. Estimates suggest that the central temperature approaches 20,000 K, with a pressure estimated around 4,000 GPa[5], at which hydrogen is believed to exist in an exotic, highly conductive state known as liquid metallic hydrogen. Hydrogen constitutes approximately 70% of Jupiter's overall mass composition, while helium, according to measurements performed by the Galileo orbiter, and presented in the work of Von Zahn, Hunten, and Lehmacher (1998), accounts for around 24%, a value 4% less than the average helium composition of the Sun and the primordial nebula. This deficit in helium may indicate, as suggested by Sanders (2012), that some helium may have dissolved in the fluid hydrogen within Jupiter's interior, descending towards the planet's core and leading to the atmosphere being depleted of helium. This ongoing precipitation phenomenon would persist as the planet steadily cools down and would contribute, along with the gradual release of primordial heat via the Kelvin-Helmholtz mechanism [6], to an internal source of heat that allows Jupiter to radiate about twice as much as the energy it receives from the Sun. However, the exact nature of this heat source has not yet been completely resolved.

Atmospheres.

[4]cf. https://lasp.colorado.edu/mop/files/2015/08/jupiter_ch4-1.pdf.

[5]For more information, see "The Interior of Jupiter".

[6]The Kelvin-Helmholtz mechanism is a fundamental physical process that manifests when the surface of a star or planet experiences cooling. As the surface temperature decreases, it leads to a reduction in internal pressure within the celestial body. This drop in pressure initiates a compression of the core, resulting in an increase in temperature.

2.2 Atmosphere

A comprehensive theory of Jupiter's atmospheric dynamic has, at present, not been developed. According to Vasavada and Showman (2005)[7], any such theory needs to explain the following facts:

- The existence of narrow stable bands and jets which are symmetric with respect to the planet's equator (Figure 2.3);
- The strong prograde jet observed at the equator (Figure 2.3);
- The difference between zones and belts (Figure 2.3);
- The origin of persistent geometric storms (Figure 2.4).

As explained in its work by Vasavada and Showman (2005)[8], theoretical approaches to understanding Jupiter's atmospheric dynamics can be broadly categorized into two main classes: *shallow* and *deep*. Shallow theories propose that the observed circulation primarily occurs within a thin outer layer, known as the *weather layer*, which sits atop a stable interior. In contrast, deep theories suggest that the observed atmospheric movements represent only surface manifestations of much deeper circulation patterns within Jupiter's outer molecular envelope. As discussed by Heimpel, Aurnou, and Wicht (2005), neither theory alone fully captures the complexity of Jupiter's atmospheric dynamics, as each has its strengths and limitations, which may indicate that the most accurate explanation will likely integrate elements from both models.

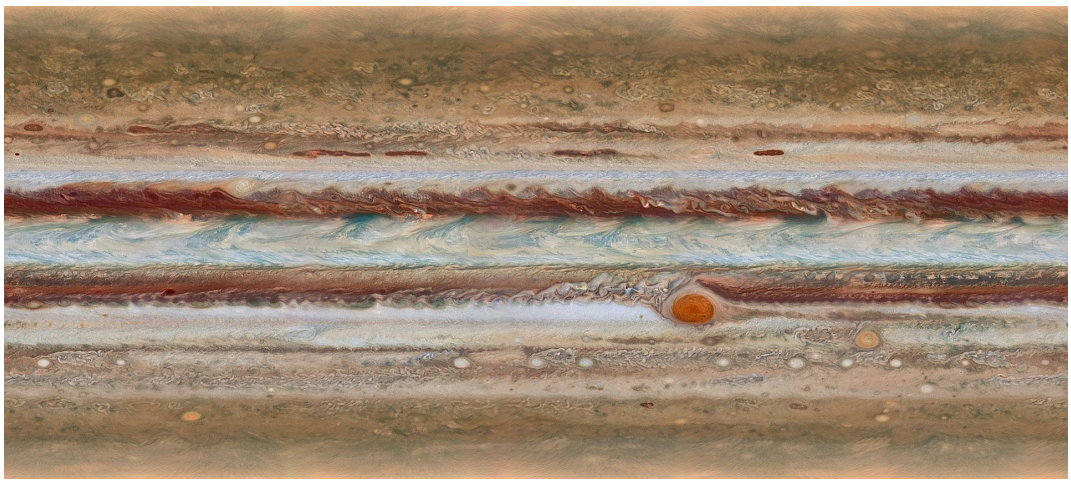

Figure 2.3. Jupiter's zones and belts. The equatorial prograde jet is visible above the GRS. The image also reveals a rare wave structure just north of the planet's equator. Credits: NASA, HST.

[7] In particular, see pp. 1942-1974.
[8] See pp. 1943-1945.

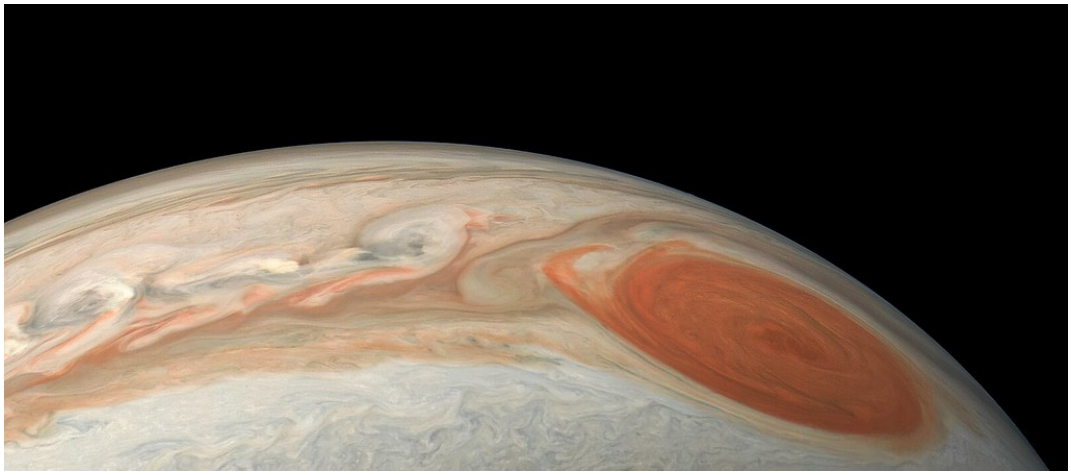

Figure 2.4. The Great Red Spot, Jupiter's most renowned feature. The first confirmed observation of this storm dates back to 1831[1], indicating that this atmospheric phenomenon is at least two centuries old. Image obtained by Juno. Credits: NASA.

2.2.1 Shallow Models

The exploration of Jovian atmospheric dynamics begins in the 1960s with pioneering works that drew inspiration from established Earth meteorology[9]. These early models assumed that Jupiter's jets were fueled by turbulent processes, driven by moist convection in the outer layers of its atmosphere, above the water clouds[10]. In these models, the formation of Jupiter's jets was attributed to *inverse cascade*, a well-known phenomenon related to two-dimensional turbulence in which small structures merge to form larger ones[11]. However, the finite size of Jupiter imposes a limit on the size of these structures, known as the Rhines scale, beyond which energy transfers to Rossby waves[12]. These waves, governed by anisotropic dispersion relations due to Jupiter's spherical and rapidly rotating nature, contribute to the production of large-scale elongated structures aligned with the equator. In this framework, as explained in the work of Vasavada and Showman (2005), vortices feed the jets and should eventually disappear by merging into them. These types of models prove quite solid in explaining narrow jets but fail in explaining large prograde jets, as the one observed at the equatorial latitude. Furthermore, interpretations by Tristan Guillot et al. (2018) and Y. e. Kaspi et al. (2018) of the odd gravity harmonics measured by Juno, seem to suggest that Jupiter's zonal winds may penetrate to depths up to 3,000 km inside the planet.

[1] *Cf.* https://www.britannica.com/biography/Samuel-Heinrich-Schwabe.

[9] As an example, the reader can refer to the work of Ingersoll and Cuzzi (1969).

[10] *Cf.* Ingersoll et al. (1969) and Vasavada (2005), pp. 1943-1945.

[11] *Cf.* Xiao et al. (2009).

[12] *Cf.* https://web.ics.purdue.edu/~dchavas/download/teaching/EAPS53600_S20/EAPS53600_S20_Lec19_RhinesSverdrupGrossMoistStability_minis_recorded.pdf.

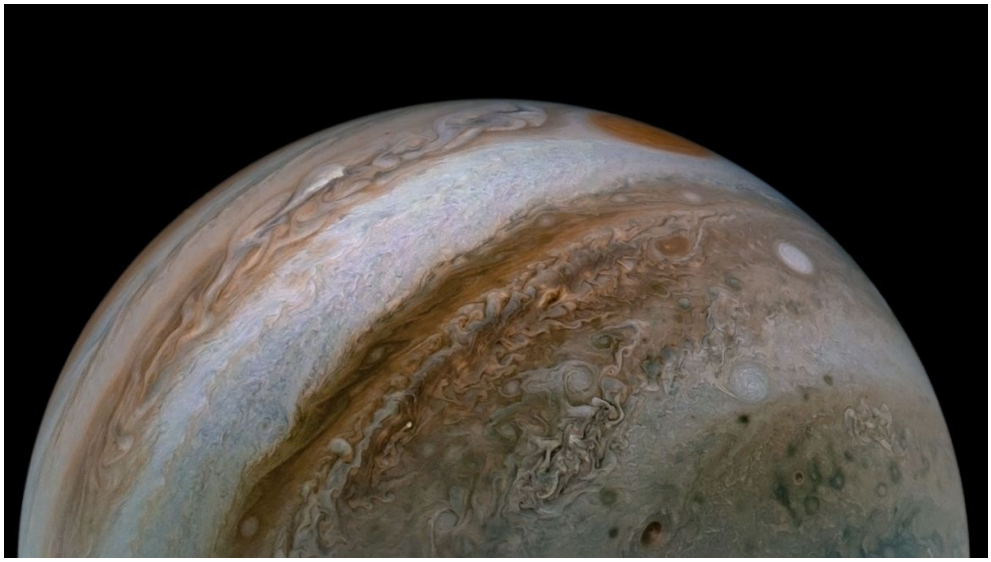

Figure 2.5. Jupiter's equatorial prograde jet. Image obtained by Juno. Credits: NASA

2.2.2 Deep Models

The concept at the basis of deep modes builds its foundation upon the Taylor-Proudman theorem which states that if a rigid body is moved slowly within a steadily rotating fluid with high angular velocity, the velocity associated to the fluid is uniform along any line parallel to the rotation axis[13]. This theorem suggests that in a rapidly rotating barotropic ideal fluid, the flow organizes into cylindrical structures parallel to the axis of rotation. In the case of Jupiter's fluid interior, which likely meets the conditions of the theorem, it is theorized that the planet's molecular hydrogen mantle can be partitioned into such cylinders, each with its independent circulation [(Vasavada and Showman (2005))]. In this framework, the latitudes where these cylindrical boundaries intersect with Jupiter's visible surface correspond to the observed jets, while the cylinders themselves manifest as the distinct zones and belts seen on the planet. This assumption serves as a cornerstone for the computational approach presented in this dissertation, as the mathematical framework outlined in Section 3.1, which constitutes the mathematical core underlying the algorithm detailed in Chapter 4, is based on the assumption that zonal winds exhibit negligible variation with altitude, implying that Jupiter's flow would need to penetrate deeply into the planet. This is crucial, because the equations we will employ in the first part of our algorithm enable the determination of isobar heights, while the results obtained from radio occultation measurements, included in the second part, provide insight into the shape of the isopycnic surface and, as highlighted by Lindal, Sweetnam, and V. Eshleman (1985), the two shapes coincide only when the relevant region can be considered barotropic.
One of the strengths of the deep models is, as explained by Vasavada and Showman (2005)[14] the ability to explain the presence of the robust prograde equatorial jet observed on Jupiter (Figure 2.5); however, always as illustrated by Vasavada and Showman (2005), deep models present significant limits, as they tend to generate a limited number of broad jets, which may not fully align with observations. The fact that both shallow and deep models exhibit strengths and weaknesses suggests that, as often occurs, a future more in-depth model will likely be represented by a combination of the two, to maximize the advantages and minimize the drawbacks.

[13] For a more detailed illustration of the Taylor-Proudman theorem, we refer the reader to Appendix A.
[14] *Cf.* pp. 1966-1972.

2.3 Exploration of Jupiter

Although Jupiter has been known since ancient times, the first observations of the planet, along with some of its moons, were conducted by Galileo Galilei in 1610 using a small telescope[15]

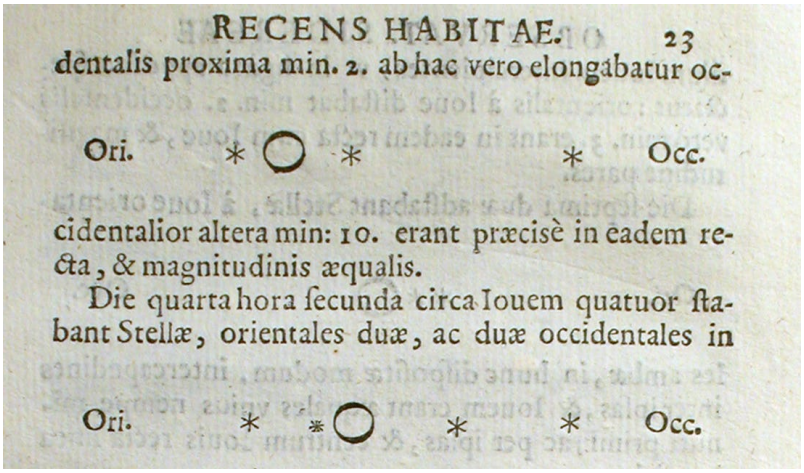
RECENS HABITAE. 23
dentalis proxima min. 2. ab hac vero elongabatur oc-
Ori. * ○ * * Occ.
cidentalior altera min: 10. erant præcisè in eadem re-
cta, & magnitudinis æqualis.
Die quarta hora secunda circa Iouem quatuor sta-
bant Stellæ, orientales duæ, ac duæ occidentales in
Ori. * * ○ * * Occ.

Figure 2.6. An excerpt from Galileo's Sidereus Nuncius, showing Jupiter and three of its moons. Source: International Astronomical Union.

Jupiter's exploration era begins in December 1973[16] with the arrival of the first spacecraft, Pioneer 10, followed by Pioneer 11 a year later[17]. Voyager 1 started its photographic documentation of Jupiter in January 1979, culminating in its closest approach on March 5, 1979, at a distance of 349,000 km from Jupiter's center[18]. Voyager 2 began transmitting images of Jupiter on April 24, 1979, and realized its closest encounter at 22:29 UT on July 9, 1979, at a distance of about 645,000 km[19]. The first orbiter to study the gas giant was Galileo, which entered Jupiter's orbit on December 7, 1995, and also deployed a probe into its atmosphere[20]. Jupiter's intense gravity field can provide a boost and trajectory change for spacecraft heading to further destinations or towards the internal Solar System: Ulysses solar probe flew past Jupiter's north pole at a distance of 451,000 km to perform a swing-by maneuver to attain the inclination required to inject into a final orbit around the Sun's north and south poles[21]. In 2000, the Cassini probe, en route to Saturn, conducted a flyby of Jupiter, capturing high-resolution images of the planet[22]. Similarly, the New Horizons probe, en route to Pluto, utilized a gravity assist from Jupiter in 2007[23]. At present, the planet is being studied by Juno, the first probe to peer below the planet's dense clouds[24]. In the context of this thesis, we leverage data derived from gravity experiments conducted by Juno, complemented by information obtained from the radio occultation measurements of Pioneer 10, Pioneer 11, Voyager 1, and Voyager 2, as well as new occultation data obtained by Juno itself. This section provides an overview of the key characteristics of these probes and the instrumentation employed during their respective missions for the collection of such data.

[15] *Cf.* https://science.nasa.gov/jupiter/exploration/.
[16] *Cf.* https://science.nasa.gov/mission/pioneer-10/.
[17] *Cf.* https://science.nasa.gov/mission/pioneer-11/.
[18] *Cf.* https://science.nasa.gov/mission/voyager/voyager-1/.
[19] *Cf.* https://science.nasa.gov/mission/voyager/voyager-2/.
[20] *Cf.* https://science.nasa.gov/mission/galileo/.
[21] *Cf.* Smith, Wenzel, and Page (1992).
[22] *Cf.* Hansen et al. (2004).
[23] *Cf.* Stern (2009).
[24] *Cf.* https://science.nasa.gov/mission/juno/.

2.3.1 Pioneer 10

Pioneer 10 marked humanity's first exploration into the outer reaches of the Solar System. Launched on March 2, 1972 [25], its primary mission was to explore Jupiter, aiming to study various aspects of the gas giant, including its atmosphere, magnetic field, radiation belts, and moons. Upon approaching Jupiter, the spacecraft commenced initial tests of its photographic instruments on November 6, 1973, from a distance of about 25 million kilometers. These tests confirmed the functionality of the instruments, setting the stage for further observations [(Fimmel, Van Allen, and Burgess, 1980)]. On November 8, Pioneer 10 crossed the orbit of Sinope, Jupiter's outermost known moon at the time, and later encountered Jupiter's magnetosphere's bow shock on November 16, evidenced by a decrease in solar wind velocity. Notably, observations revealed that Jupiter's magnetic field was opposite Earth's [(Fimmel, Van Allen, and Burgess, 1980)]. During its flyby, Pioneer 10 captured over 500 images of Jupiter, with its photopolarimeter producing images in red and blue wavelengths, later combined to create true-color images. By December 2, the quality of these images surpassed those obtainable from telescopes on Earth [(Fimmel, Van Allen, and Burgess, 1980)]. Despite encountering intense radiation levels, Pioneer 10 successfully photographed Jupiter's moons Ganymede and Europa, providing valuable data on their surface characteristics. Venturing close to Jupiter's magnetic equatorial plane, the spacecraft experienced the highest concentration of ion radiation in the planet's magnetosphere, peaking at levels 10,000 times stronger than those around Earth [(Fimmel, Van Allen, and Burgess, 1980)]. Starting from December 3rd, radiation intensity reached levels that caused errors in Pioneer's commands. While many of these errors were rectified through emergency interventions, some images of Io and close-up shots of Jupiter were lost. Similar false commands occurred during the spacecraft's departure from the planet. The image of Ganymede revealed a low albedo in the central and southern polar regions, with the northern pole appearing brighter. Due to its distance, detailed images of Europa were unattainable, leading to some illusory albedo features [(Fimmel, Van Allen, and Burgess, 1980)]. The spacecraft's trajectory was strategically chosen to allow for observations of Io from behind, enabling the analysis of its atmosphere through radio occultation experiments. These observations revealed the presence of an ionosphere approximately 700 kilometers above Io's sunlit surface, with a density of 60,000 electrons per cubic centimeter on the daytime side and 9,000 on the nighttime side. A surprising discovery was made regarding Io's orbit within a hydrogen cloud spanning 805,000 kilometers, with dimensions of 402,000 kilometers in height and width. Similar readings near Europa suggested a comparable structure, albeit smaller, extending about 110,000 kilometers [(Fimmel, Van Allen, and Burgess, 1980)]. At its closest approach, Pioneer 10 achieved a velocity of 126,000 kilometers per hour, passing at a distance of 132,354 kilometers from Jupiter's cloud tops[26], and capturing images of the Great Red Spot and of the terminator before losing communication as it passed behind the planet. Data from radio occultation enabled the measurement of vertical temperature structures in Jupiter's upper atmosphere, revealing a temperature inversion at specific altitudes [(Fimmel, Van Allen, and Burgess, 1980)]. As the spacecraft moved away from the planet, it captured images of Jupiter's crescent [27](Figure 2.8) and once again crossed the bow shock during its outward journey, traversing it a total of 17 times before exiting completely from Jupiter's magnetosphere [(Fimmel, Van Allen, and Burgess, 1980)].

[25] cf. https://science.nasa.gov/mission/pioneer-10/.
[26] See 25.
[27] cf. https://science.nasa.gov/resource/pioneer-10-at-jupiter/.

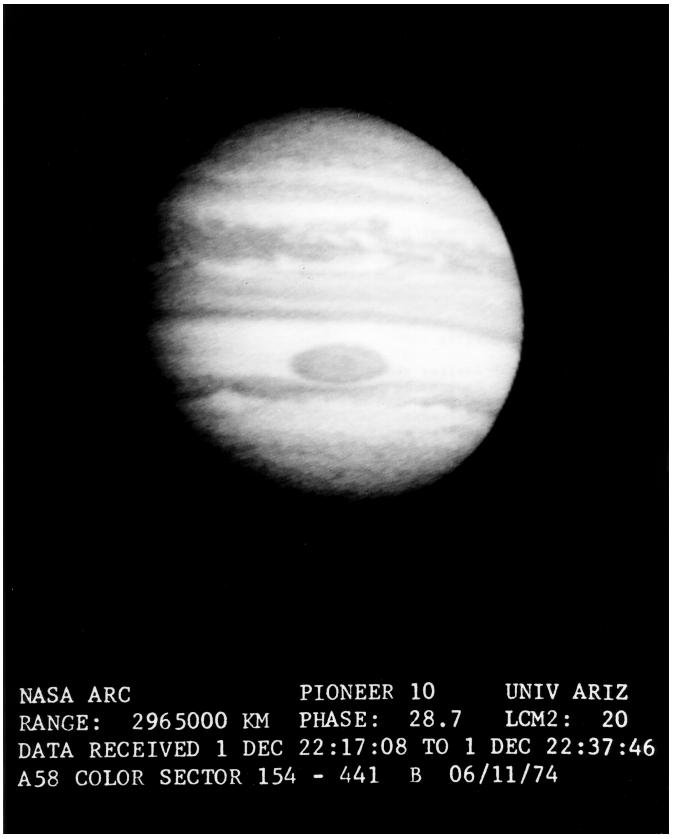

Figure 2.7. Pioneer 10 image of Jupiter taken at a distance of 2,965,000 km produced by assembling on Earth successive scans captured by the probe. Image taken by Smithsonian National Air and Space Museum. Credits: NASA.

Figure 2.8. Jupiter's crescent-shape, termed as the "Sunrise on Jupiter". Credits: NASA.

2.3.2 Pioneer 11

Pioneer 11 was the first probe to observe Jupiter's polar regions (Figure 2.9).
Launched on April 5, 1973, the probe entered the Jovian system on December 3, 1974[28], marking the second visit of a human-made spacecraft to the gas giant. By mid-March 1974, Pioneer 11 safely navigated through the asteroid belt without sustaining any damage[29]. Subsequently, on April 26, 1974, the spacecraft underwent a midcourse correction, following an earlier adjustment on April 11, 1973[30]. These corrections aimed to guide Pioneer 11 on a trajectory that would bring it much closer to Jupiter than its predecessor to ensure a polar flyby. On November 25, 1974, at 03:39 UT, Pioneer 11 crossed Jupiter's bow shock[31], marking the beginning of its encounter with the gas giant. Its closest approach occurred at 05:22 UT on December 3, 1974, at a distance of about 42,500 kilometers from the planet's upper clouds[32], a distance three times closer than its predecessor. At this point, the probe was traveling at a speed of over 171,000 kilometers per hour[33], making it the fastest human-made object at the time. Because of its higher velocity, even though Pioneer 11's distance from Jupiter was smaller than that of Pioneer 10, the time exposure of the probe to Jupiter's radiation belts was shorter. Pioneer 11 repeatedly crossed Jupiter's bow shock, indicating dynamic changes in the boundaries of the Jovian magnetosphere under the influence of the solar wind. The probe collected numerous images of Jupiter, including improved pictures of the GRS, as well as approximately 200 images of Jupiter's moons[34].

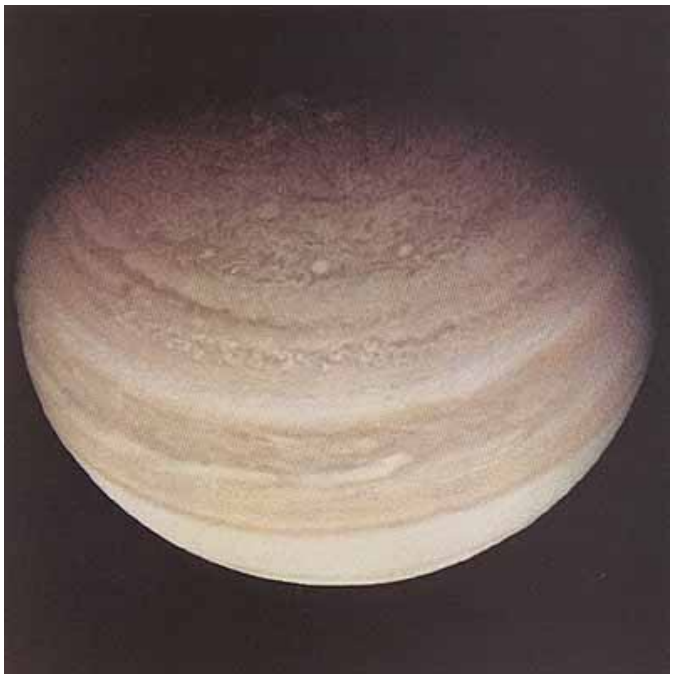

Figure 2.9. Jupiter's northern polar region as observed by Pioneer 11 from an altitude of 1,079,000 km. Credits: NASA.

Both Pioneer probes carry aboard two identical gold-anodized aluminum plaques featuring a pictorial message (Figure 2.10) in case either Pioneer 10 or Pioneer 11 is intercepted by intelligent extraterrestrial life.

[28] cf. https://science.nasa.gov/mission/pioneer-11/.
[29] cf. https://www.nasa.gov/solar-system/planets/saturn/40-years-ago-pioneer-11-first-to-explore-saturn/.
[30] See 28.
[31] See 28.
[32] See 28.
[33] See 28.
[34] See 28.

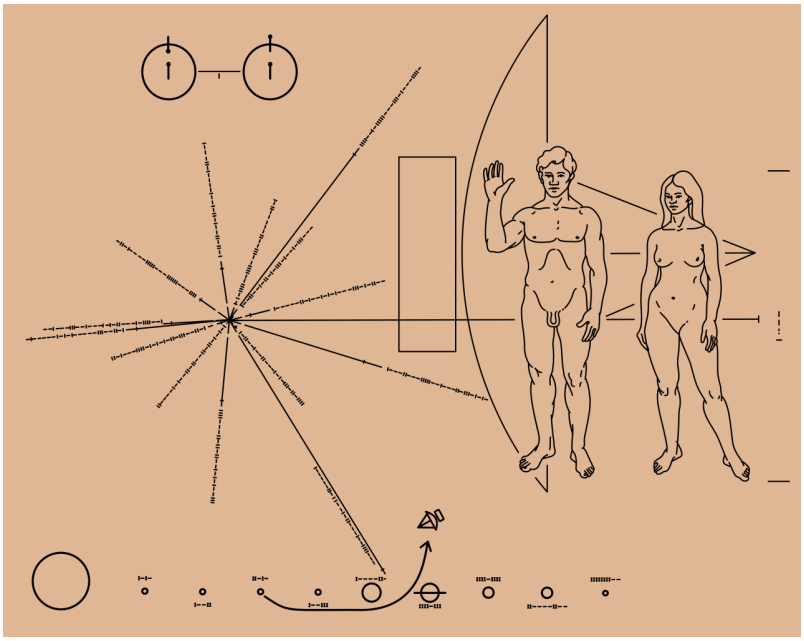

Figure 2.10. The illustration of the plaque installed onboard Pioneer 10 and Pioneer 11 probes. From top to bottom, and from left to right, it depicts the hyperfine transition of neutral hydrogen, the Sun and galactic landmarks, the Solar System with the Earth location flagged as the probe's departure point, the silhouette of the spacecraft, and the figures of a man and a woman. Credits: NASA.

Figure 2.11. Illustration depicting the Pioneer program. Credits: NASA.

2.3.3 Voyager 1

Voyager 1 is one of the first probes to ever explore the outer Solar System and, at present, is the most distant human-made object from Earth [35]. As part of the Voyager program, the probe was launched on September 5, 1977, from Cape Canaveral Launch Complex 41, and entered the Jovian system in January 1979, reaching the closest approach on March 5 of the same year at a distance of about 280,000 kilometers from the planet's center[36]. During Voyager 1 data acquisition, which took place until April 1979, the probe observed a rich collection of geological dynamical features, the most surprising of which was the discovery of volcanic activity on Jupiter's satellite Io. This marked the first time active volcanoes had been observed outside planet Earth [(Strom and Schneider, 1982)]. Voyager 1, together with Voyager 2, also observed for the first time Jupiter's ring system and provided high-resolution analysis of the gas giant's moons, radiation belts, and atmospheric dynamical features[37].

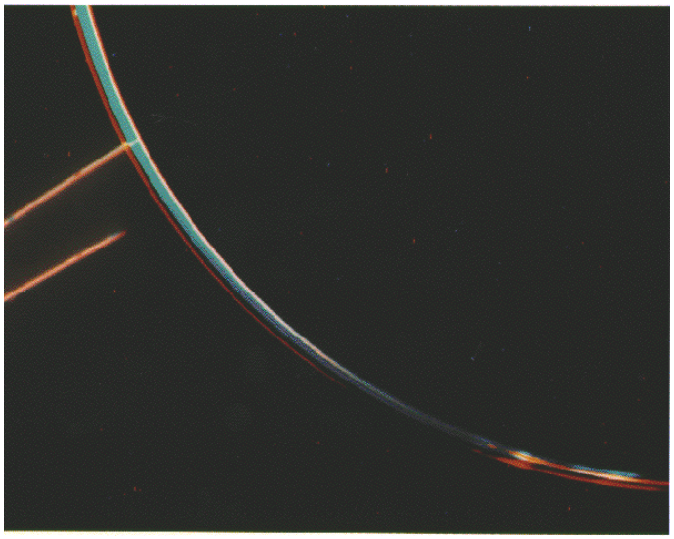

Figure 2.12. First observation of Jupiter's planetary rings. Credits: NASA JPL.

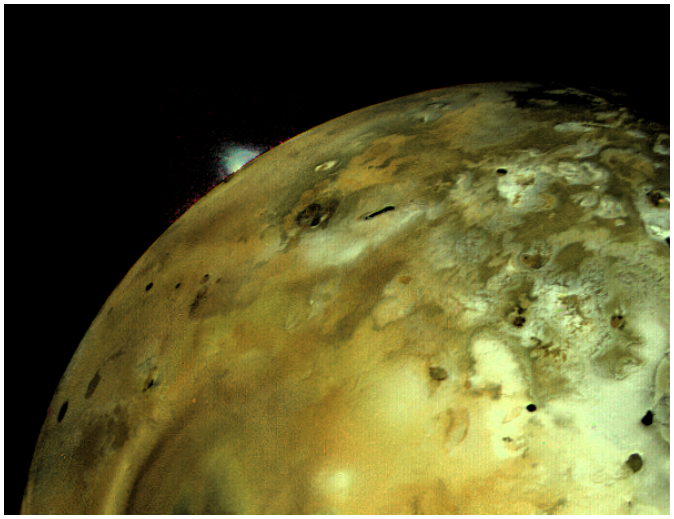

Figure 2.13. Eruption plume of the volcano Loki rising over 160 km over the limb of Io. Credits: NASA.

[35] cf. https://voyager.jpl.nasa.gov/mission/status/.
[36] cf. https://science.nasa.gov/mission/voyager/voyager-1/.
[37] cf. https://news.cornell.edu/stories/1998/09/jupiters-rings-formed-dust-its-satellites.

2.3.4 Voyager 2

Part of the Voyager program as its sibling, Voyager 2 is one of the first probes to explore the outer Solar System and, at present, the first and only probe to have visited Uranus and Neptune. Launched on August 20, 1977[38], Voyager 2 was injected into a trajectory that took longer to reach Jupiter and Saturn but allowed further encounters with the ice giants[39]. Voyager 2 closest approach to Jupiter occurred on July 9, 1979, at a distance of 570,000 km from the planet's cloud tops[40]. The probe returned new detailed images of Jupiter's dynamical features, as well as of Jovian moons Amaltea, Io, Callisto, and Europa (Fig. 2.15). Notably, Voyager 2's 10-hour observation of Io confirmed the volcanic activity discovered by Voyager 1 (Figure 2.14) and, as presented in Strom and Schneider (1982), revealed further ongoing volcanic processes between the two flybys. During its exploration of the Jovian system, Voyager 2 also discovered three new satellites: Adrastea, Metis, and Thebe[41]. Additionally, it conducted intensive studies of Europa, providing the first indications of the presence of water beneath its icy crust.

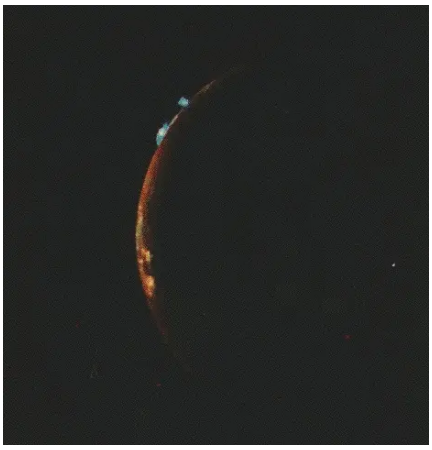

Figure 2.14. Picture of Io taken by Voyager 2 on the evening of July 9, 1979 at a distance of 1.2 million kilometers. Blue plumes represent two volcanic eruptions about 100 km high[42]. Credits: NASA/JPL.

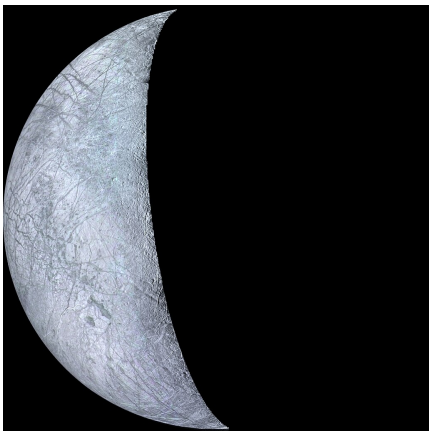

Figure 2.15. A color mosaic of Europa. Bright areas are probably ice deposits, while shaded areas could indicate either rocky terrain or patches with a less uniform distribution of ice. Credits: NASA.

[38] cf. https://voyager.jpl.nasa.gov/mission/status/.
[39] cf. https://voyager.jpl.nasa.gov/mission/timeline/.
[40] cf. https://voyager.jpl.nasa.gov/mission/science/jupiter/.
[41] cf. https://www.esa.int/Science_Exploration/Space_Science/Juice/A_history_of_Jupiter_exploration_the_journey_to_Juice.

Both Voyager probes carry aboard two identical phonographs, known as Voyager Golden Records (Figure 2.16, containing electronically inserted sounds and images that portray the diversity of life and culture on Earth. The content of the records, meant as a time capsule, was selected by a committee of Cornell University led by Carl Sagan[43].

Figure 2.16. The Voyager Golden Record. Credits: NASA.

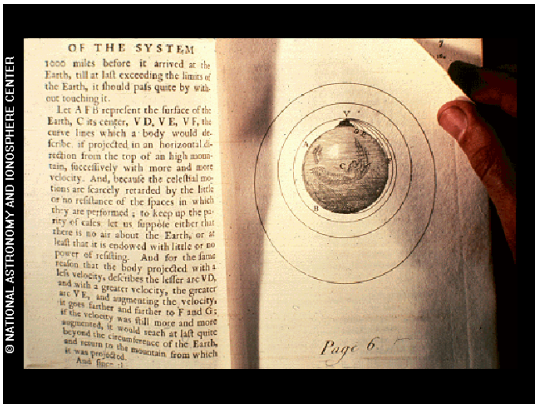

Figure 2.17. One of the pictures contained in Voyager Golden Records, representing a book of Newton's System of the World, published into the author's Mathematical Principles of Natural Philosophy.
Image taken by the NASA/JPL Voyager database.

[43] cf. https://voyager.jpl.nasa.gov/golden-record/.

2.3.5 Juno

Launched on August 5, 2011, from the Cape Canaveral Air Force Station as part of the New Frontiers [44] program, the probe entered orbit around Jupiter on July 4, 2016[45].
Juno's primary mission consists of gathering data regarding Jupiter's composition, gravitational field, magnetic field, and polar magnetosphere. Additionally, Juno aims to uncover insights into Jupiter's formation, such as the eventual presence of a rocky core, the amount of water in the deep atmosphere, the mass distribution, and the characteristics of the planet's powerful deep winds[46].
Following Galileo, which operated from 1995 to 2003[47], Juno represents the second human-made orbiter to study the Jovian system. Unlike previous outer planetary missions, Juno relies on solar panels, a common feature in Earth's orbiting satellites and inner Solar System missions but rarely used for outer planetary missions due to the high distances from the Sun. In particular, Juno mounts three 9-meter-long solar panels which play a crucial role in both stabilizing the spacecraft and generating power for its operations[48]. In the context of this thesis, Juno already achieved outstanding results, by having already acquired updated estimates in both gravity measurements [(Durante et al., 2020)] and radio occultations [(Caruso et al., 2023)].
Common denominator for all the missions presented is the Deep Space Network (Figure 2.18), an international array of radio telescopes located at Goldstone (United States), Madrid (Spain), and Canberra (Australia), that supports interplanetary and near-Earth missions, as well as radio and radar astrophysics[49].

Figure 2.18. Cows graze in front of the multiple radio dishes of Canberra's Deep Space Communication Complex. Credits: NASA/JPL-Caltech.

[44] The New Frontiers program is a series of space exploration missions being conducted by NASA to further the understanding of the Solar System. There are currently three New Frontiers missions in progress and one in development. New Horizons, which was launched in 2006 and reached Pluto in 2015, Juno, which was launched in 2011 and entered Jupiter orbit in 2016, and OSIRIS-REx, launched in September 2016 towards asteroid Bennu for detailed studies from 2018 to 2021 and a sample return to Earth in 2023.
On June 27, 2019, Dragonfly was selected to become the fourth mission of the program.
[45] cf. https://www.jpl.nasa.gov/missions/juno.
[46] cf. https://science.nasa.gov/mission/juno/.
[47] cf. https://science.nasa.gov/mission/galileo/.
[48] cf. https://www.jpl.nasa.gov/news/nasas-juno-spacecraft-breaks-solar-power-distance-record.
[49] cf. https://www.nasa.gov/directorates/somd/space-communications-navigation-program/what-is-the-deep-space-network/.

2.3.6 Hubble Space Telescope

Hubble Space Telescope is one of the largest and most versatile space telescopes ever built. Funded in the 1970s by NASA with contributions from the European Space Agency, it was launched into low-Earth orbit on April 24, 1990, starting its service on May 20 of the same year[50]. After over 33 years of mission duration, the telescope is still in activity at an altitude of approximately 525 km[51] performing top-notch research in all the main fields of modern astrophysics. In this thesis, with the exception of the measurements obtained in 1979 during the Voyager 2 fly-by, all the included zonal wind profile data have been collected by Hubble via observations performed with the Wide Field Camera 3 (WFC3), an instrument installed onboard on May 14, 2009[52]. Wide Field Camera 3 is a fourth-generation UVIS/IR imager capable, as suggested by the name, of observing in both UV/visible channels and near-infrared. Its UV/optical channel employs a pair of CCDs, each with a resolution of 2048×4096 pixels, capable of capturing images in the 200 to 1000 nm range. Meanwhile, the near-infrared channel features a 1024x1024 detector array, covering wavelengths from 800 to 1700 nm. The optical channel provides a field of view of 164 by 164 arcsec, while the NIR channel offers a slightly smaller field of view at 135 by 127 arcsec. Notably, the IR channel is designed to be insensitive beyond 1700 nm to avoid noise from thermal emission generated by the telescope's instrumentation. This innovative idea avoids the need for cryogenic cooling solutions, with the detector instead cooled through a thermo-electric cooler, simplifying the instrument's architecture and ensuring WFC3 an extended operational life.

Figure 2.19. WFC3 preparing for its departure aboard STS-125. Credits: NASA.

[50] *Cf.* https://science.nasa.gov/mission/hubble/.
[51] *Cf.* https://science.nasa.gov/mission/hubble/.
[52] *Cf.* https://www.stsci.edu/hst/instrumentation/wfc3.

CHAPTER 3

Theoretical background

Accurate computation of the shape of a fluid, rotating celestial body requires a comprehensive analysis which includes gravitational forces, planetary rotation, and atmospheric wind effects. Within this Chapter, we present the theoretical foundations essential for deriving the physical parameters needed in the computation outlined in Chapter 4, as well as the methodologies employed to investigate them. In Section 3.1, we introduce the method to determine the shape of a co-rotating gaseous celestial body considering data regarding both the gravitational field and the zonal winds. Subsequently, in Section 3.2, we delve into the technique utilized to measure zonal harmonics in interplanetary gravity experiments. These harmonics are crucial in accurately modeling the gravitational field of celestial bodies and, consequently, their shapes. In Section 3.3, we introduce the technique used in determining cloud-level wind measurements in gaseous planets. Lastly, in Section 3.4, we explore the fundamental principles underlying radio occultation experiments. These experiments represent precious tools for probing the atmospheric structure of celestial bodies, providing essential data for refining our computational models.

3.1 Shape Calculation of a Fluid, Rotating Celestial Body

Data from the gravitational field of a fluid, rotating celestial body can be used, once properly paired with the information regarding zonal wind velocities, to calculate its shape.
Jupiter's internal structure models suggest that the predominant component of the planet's gravitational field displays symmetry concerning the spin axis, as expected for a fluid in hydrostatic equilibrium, as presented by W. Hubbard (1982) and William B Hubbard and Militzer (2016), hence the acceleration produced by the gravity field can be thought of as a vector contained within the local meridian plane. When calculating the gravitational acceleration for an object co-rotating with the atmospheric gas, it's essential to account for both the external gravitational field and the centrifugal force. Consequently, the resulting acceleration can be described considering its radial and latitudinal components, as illustrated in Lindal, Sweetnam, and V. Eshleman (1985)]:

$$\mathbf{g} = \mathbf{u}_r g_r + \mathbf{u}_\phi g_\phi \tag{3.1}$$

where $\mathbf{u}_r$ and $\mathbf{u}_\phi$ represent the unit vectors in the radial and latitudinal directions, respectively.

Let us consider the well-known result

$$\mathbf{g} = -\nabla U \tag{3.2}$$

under the assumption of axial symmetry, Eq. (3.1) vector components can be written as:

$$g_r(r,\phi) = -\frac{GM}{r^2}\left(1 - \sum_{i=2}^{\infty}(i+1)J_i\left(\frac{R}{r}\right)^i P_i(\sin\phi) + \frac{2}{3}\omega^2 r[1 - P_2(\sin\phi)]\right) \tag{3.3}$$

$$g_\phi(r,\phi) = -\frac{GM}{r^2}\sum_{i=2}^{\infty} J_i\left(\frac{R}{r}\right)^i \frac{dP_i(\sin\phi)}{d\phi} - \frac{1}{3}\omega^2 r\frac{dP_2(\sin\phi)}{d\phi} \tag{3.4}$$

where G is the universal gravitational constant, M is the mass of the celestial body, J_i is the i-th zonal harmonic coefficient, R is the reference radius to which the zonal harmonic coefficients have been normalized, P_i are the Legendre polynomials of degree i, r is the distance from the center of mass, ϕ is the planetocentric latitude, and ω is the angular velocity, expressed as

$$\omega = \omega_{\mathrm{III}} + \frac{V_{\mathrm{wind}}}{r\cos\phi} \tag{3.5}$$

where ω_{III} denotes the angular velocity corresponding to the System III[1] rotation period, representing the rigid body contribution, and the second term encompasses the centrifugal part, including the effect of eastward zonal winds [(Lindal, Sweetnam, and V. Eshleman, 1985)].
In particular, the term V_{wind} represents the cloud-level wind projected barotropically parallel to the spin axis of the celestial body, and is a function of the planetographic latitude, which is simply equal to $\phi + \psi$, where

$$\psi = \arctan\left(\frac{g_\phi}{g_r}\right). \tag{3.6}$$

[1]The System III reference frame for Jupiter is a coordinate system commonly used in planetary astrophysics to track features on the planet's surface as it rotates. In the context of Jupiter, System III is a fixed reference frame where the planet's rotation period at the equator is precisely defined as 9 hours, 55 minutes, and 29.71 seconds. This system provides a consistent way to describe the positions of atmospheric phenomena, such as storms and cloud patterns, as they move across Jupiter's surface over time. It serves as a crucial tool for astrophysicists and planetary scientists to study the dynamics and evolution of Jupiter's atmosphere.

The gravity potential associated to a uniformly rotating fluid may be calculated by integrating $\mathbf{g}$ from a point of interest to a point at infinity on the spin axis

$$U(r,\phi) - U(\infty, \frac{\pi}{2}) = \int_{(r,\phi)}^{(\infty,\frac{\pi}{2})} \mathbf{g}\,\mathbf{ds} \tag{3.7}$$

with $\mathbf{ds}$ infinitesimal vector representing an elemental displacement along the path of integration.
Considering a fluid with a uniform angular velocity

$$\omega = \omega_{\mathrm{III}} \tag{3.8}$$

and setting the constant of integration such as on the spin axis

$$\lim_{r\to 0} U(r,\phi) = 0 \tag{3.9}$$

Eq. (3.7) leads to the result [Lindal, Sweetnam, and V. Eshleman (1985)]:

$$U(r,\phi) = -\frac{GM}{r}\left(1 - \sum_{i=2}^{\infty} J_i \left(\frac{R}{r}\right)^i P_i(\sin\phi) - \frac{1}{2}\omega_{\mathrm{III}}^2 r^2 \cos^2(\phi)\right). \tag{3.10}$$

where the gravitational harmonic J_i is determined through interplanetary gravity experiments.

The shape of gaseous celestial bodies can be calculated along equipotential surfaces.
To initiate the computation, a starting point on the equipotential surface needs to be determined, hence the first step consists in assuming rigid-body approximation and determining the gravity potential of the reference geoid using Eq. (3.10) and setting a reference radius R_{ref} equal to the polar radius[2]:

$$U_{\mathrm{ref}} = U(r_p, \frac{\pi}{2}). \tag{3.11}$$

Next, we set a grid of latitudes and, for each latitude, an arbitrary radius for which we calculate, using again Eq. (3.10), the corresponding potential

$$U(r,\phi) = U' \tag{3.12}$$

and we compute its deviation from the reference equipotential surface defined in Eq. (3.11) by subtracting the latter from the newly calculated potential:

$$\Delta(U) = U' - U_{ref} \tag{3.13}$$

The obtained $\Delta(U)$ is used to compute the correction required in the radius at the latitude ϕ, by using the equation:

$$\Delta(r) = \frac{\Delta U}{g_r} \tag{3.14}$$

where g_r can be calculated by substituting ω_{III} to ω in Eq. (3.3).

[2] According to Lindal, Sweetnam, and V. Eshleman (1985), although the uncertainty concerning the polar radius is greater than that concerning the equator, the choice of the polar radius as reference radius is convenient since, at the poles, the effects due to the centrifugal term in Eq. (3.5) are smaller.

The idea now consists of iterating the algorithm with the updated radius value, $r + \Delta r$, until the desired accuracy is attained, a condition met when

$$\Delta(U) = U^{(n)} - U_{ref} < \epsilon \tag{3.15}$$

where $U^{(n)}$ represents the n-th computed gravitational potential and ϵ denotes a selected threshold value, chosen to be sufficiently small.

Once this has been performed for all latitudes ϕ, it is time to include the effects of the winds. Figure (3.1) illustrates how eastward zonal winds perturb a geoid.
A zonal jet with eastward velocity $V_{wind} \neq 0$ perturbs the acceleration of gravity at a point (r, ϕ) by an amount:

$$\Delta g_{\text{wind}} = |\mathbf{g} - \mathbf{g}_{\text{ref}}| = V_{\text{wind}} \left(2\omega_0 + \frac{V_{\text{wind}}}{r \cos \phi} \right) \tag{3.16}$$

with Δg_{wind} vector inside the meridian plane which is parallel to the equatorial plane.
Considering the line integral of $\mathbf{g}$ from a point L_1 on the geoid down the local field line to a point L_2 on the reference geoid, and then along the reference geoid to the spin axis, it can be shown that [Lindal, Sweetnam, and V. Eshleman (1985)]

$$\int_{\phi}^{\frac{\pi}{2}} \Delta g_{\text{wind}} \sin(\phi + \psi_{\text{ref}}) \frac{r_{\text{ref}}(\phi)\, d\phi}{\cos(\psi_{\text{ref}})} = \int_0^{h(\phi)} |\mathbf{g}|\ dh \tag{3.17}$$

where ψ_{ref} can be computed using Eq. (3.6), (3.3), and (3.4) by setting ω equals to ω_{III}.
This equation can be considered strictly correct only under the assumption that deviations from hydrostatic equilibrium and horizontal stratification are negligible for all the geodetic levels traversed by the integration path.

Solving Eq. (3.17) with respect to the altitude of the geoid yields to:

$$h(\phi) = \frac{1}{\langle g \rangle} \int_{\phi}^{\frac{\pi}{2}} V_{wind} \left[2\omega_0 + \frac{V_{wind}}{r_{ref}(\phi) \cos(\phi)} \right] \frac{\sin(\phi + \psi_{ref})}{\cos(\psi_{ref})} r_{ref}(\phi)\, d\phi \tag{3.18}$$

where $\langle g \rangle$ represents the average acceleration of gravity along the field line connecting points L_1 and L_2, and $h(\phi)$ is referred to as the *dynamical height*, a value that quantifies the perturbation on the shape we would have by solid body rotation only due to the effects of the zonal winds.
Note that $\langle g \rangle$ is a slowly varying function of h; this, combined with the highly iterative structure defining the algorithm, makes this computational method well-suited for implementation on a computer. Equation (3.18) assumes that winds do not vary with altitude. Considering a gas giant, this implies that the zonal winds would need to penetrate very deep into the structure of the planet. Interpretations of Jupiter's zonal harmonics presented by Tristan Guillot et al. (2018) and Y. e. Kaspi et al. (2018) show that the measured Jupiter's gravitational coefficients can be explained if the observed winds penetrate to depths of $\sim$ 3000 km into the planet. Although Kong et al. (2018) and Qin et al. (2020) claim that the interpretation is not unique, this scenario is supported both by the even and odd zonal harmonics and by studies on the magnetic data, as documented in Eli Galanti, Hao Cao, and Yohai Kaspi (2017).

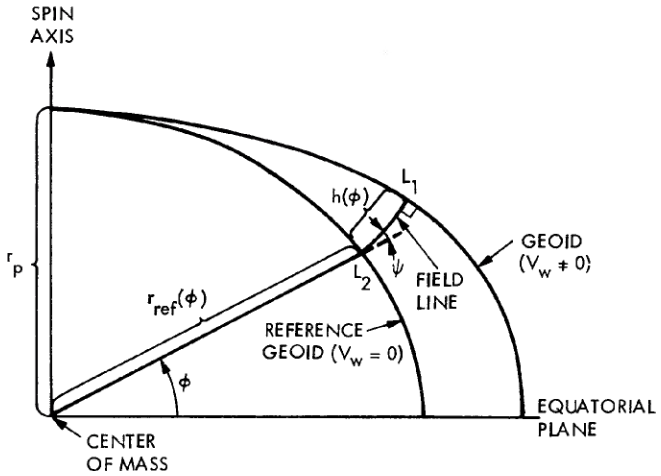

Figure 3.1. A geoid and its perturbation due to a zonal jet with eastward velocity $V_{wind} \neq 0$. Image taken from the method described by Lindal, Sweetnam, and V. Eshleman (1985).

3.2 Measurement of Jupiter's gravity field

The external, harmonic, gravitational potential of a celestial body can be expanded into a series of complex spherical harmonic functions, Y_{nm}, of degree n and order m, multiplied by a scaling factor $\frac{R}{r}$ which depends on the normalized radial distance from the center of the body [(Luciano Iess et al., 2018)]:

$$U(r,\theta,\phi) = -\frac{GM}{r}\left[1 + \sum_{n\geq 2}\left(\frac{R}{r}\right)^n \sum_{m=-n}^{n} U_{nm} Y_{nm}(\theta,\phi)\right] \tag{3.19}$$

where G is the gravitational constant, M is the mass of the body and R is a reference radius, typically chosen as the equatorial radius. In the case the internal density of the body is known, the harmonic coefficients U_{nm} can be obtained, as illustrated in the work of Bertotti, Farinella, and Vokrouhlicky (2012), by integrating over the volume of the body

$$U_{nm} = \frac{1}{(2n+1)MR^n}\int_V (r')^n\, Y^*_{nm}(\theta',\phi')\rho(r',\theta',\phi')\, dV' \tag{3.20}$$

which, in the case ρ does not depend on longitude, yields to

$$J_n = -\frac{1}{MR^l}\int_V (r')^l\, P_n(\theta')\rho(r',\theta')\, dV' = -\sqrt{2n+1}U_{l0} \tag{3.21}$$

This result indicates that zonal coefficients J_n bear valuable information regarding how density distribution organizes inside a celestial body. As described by Luciano Iess et al. (2018), the gravity harmonics of a fluid and rotating celestial body can be decomposed into a static component, which arises from solid-body rotation, and a dynamic component which arises from flows.
In the absence of internal dynamics, the gravity field exhibits axial and hemispherical symmetry and is dominated by even zonal gravity harmonics, J_{2n}, which are approximately proportional to q^n, where q represents the ratio between centrifugal acceleration and gravity referred to the body's equator. This means that, as described by W. Hubbard (1999) and Yohai Kaspi (2013), any asymmetry in the gravity field may be interpreted as a hint of differential rotation and deep internal flows. On the other hand, as illustrated by Lanzano (1974) and W. Hubbard (1999), odd harmonics may be thought of as indicators regarding zonal wind depths in the atmosphere.

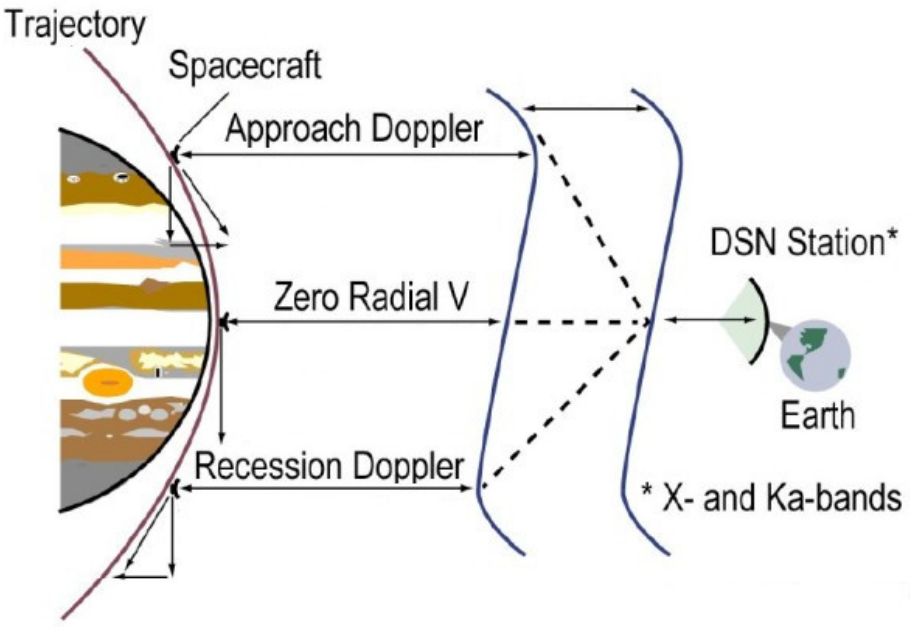

Figure 3.2. Scheme of a gravity experiment. Image taken from spaceflight101.com and re-edited.

Measurement of gravity harmonics occurs during interplanetary missions' gravity experiments. As presented in Luciano Iess et al. (2018), a typical gravity experiment consists of Doppler shift measurements between a probe acting as a test particle falling into the gravity field of the celestial body, and a ground antenna located to the Earth. A scheme depicting the experimental setup is illustrated in Figure 3.2. In this thesis, we use the state-of-the-art in the determination of Jupiter's gravity harmonics, presented in Durante et al. (2020). These measurements were conducted using the Deep Space Network's DSS 25 antenna located at NASA's Goldstone complex, in the United States, and the Canberra Deep Space Communication Complex, in Australia. The setup involved simultaneous transmission of X-band (7.2 GHz) and Ka-band (34 GHz) radio signals by DSS 25. These signals were then returned with preserved phase coherence through Juno's Small Deep Space Transponder and Ka-band Translator System, operating at frequencies of X-band (8.4 GHz) and Ka-band (32 GHz), respectively. The advantage of Ka-band radio links lies, as explained by Luciano Iess et al. (2018), in their excellent resistance to detrimental effects due to charged particles along the propagation path, including those emanating from the Io torus, a potential source of bias in gravity estimates. Data collected at the Goldstone complex for each observation arc is supported by measurements obtained at the Canberra DSN complex after the completion of Goldstone's tracking pass. By comparing the transmitted and received frequencies, the Doppler shift is thus numerically computed[3] including all the known effects which significantly contribute to Juno's motion about Jupiter, listed in Luciano Iess et al. (2018) and Durante et al. (2020). According to models of Jupiter's interior structure proposed by W. Hubbard (1982) and William B Hubbard and Militzer (2016), the planet's gravity is primarily governed by an axially and hemispherically symmetric component, attributed to solid-body rotation. This component, represented by even zonal harmonic coefficients, J_{2n}, is determined by the radial density distribution within the rotating planet. However, the presence of atmospheric and internal dynamics, as discussed in studies by Yohai Kaspi et al. (2010), Yohai Kaspi (2013), and Tristan Guillot et al. (2018), may lead to small density perturbations which give rise to a more intricate gravity field, potentially involving odd and tesseral harmonics, along with minor adjustments to the even zonal harmonics.

[3]The computation includes the use of two independent software packages: MONTE, developed by JPL [Evans et al. (2018)], and ORBIT14, developed at the University of Pisa [Daniele Serra et al. (2019)].

3.3 Zonal Wind Models

The most striking feature of Jupiter is its banded structure, home to swaths of bright, colorful clouds and vortices. The zonal flow, the average east-west winds across the visible cloud deck represents, as presented in Ingersoll, Dowling, et al. (2004) a crucial constraint on Jupiter's atmospheric circulation. Jupiter's zonal wind profile has been a subject of intense study since the Voyager missions. Historically, there have been two primary methods for measuring Jupiter's zonal flow. The first, and more widely used, is known as the *global* method and involves the direct computation of zonal velocities from image or mosaic pairs, bypassing the need to first determine individual two-dimensional velocity vectors that constitute the velocity fields. The second method, referred to as *local*, entails determining zonal velocities by tracking large-scale features over extended periods, generating one-dimensional or two-dimensional velocity fields which are then averaged over their east-west components. The zonal wind profiles used in this thesis are derived through the global method and are presented in Limaye (1986) and J. Tollefson et al. (2017). In the following subsection, we present the fundamental concepts that underlie this technique.

3.3.1 The Global Method

According to J. Tollefson et al. (2017), the global method consists of deriving directly the zonal velocity from pairs of images or mosaics, bypassing the need to initially calculate individual two-dimensional velocity vectors. Instead, the zonal flow is assessed by identifying longitudinal correlations among clouds within the image or mosaic pair's coverage area. This area typically spans a broad range in longitude, often encompassing the entire planetary circumference while maintaining a minimal latitude range. Specifically, the zonal wind profiles used in this thesis are derived through a variant of the global method known as the 1D correlation method. In this approach, maps are divided into latitude strips, as depicted in Figure 3.3, and correlations are derived by measuring the horizontal shift between a pair of such strips. The zonal wind velocity is hence determined by dividing a specific horizontal shift by the time interval between the map strips. Correlations are calculated for each point where a pair of time-separated maps covers a given longitude and, by identifying the velocities which maximize such correlations, it is possible to determine the zonal velocities associated with each latitude bin.

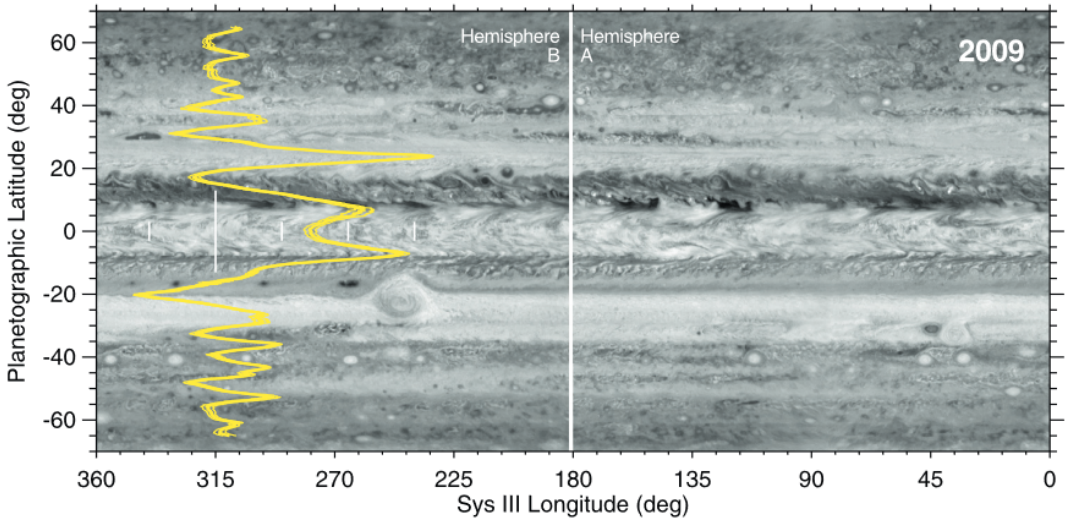

Figure 3.3. An example of how maps are organized into latitude strips in the 1D correlation method. In this case, the map has also been divided into two hemispheres to optimize the observation time. Image taken by J. Tollefson et al. (2017).

To compute the aforementioned correlations, each map is initially cropped to a particular longitude range around the central meridian and latitude range. Subsequently, all the significant features such as large vortices and other dynamical features which do not follow the background flow and may affect the accuracy of the measurements are excluded through masking. Throughout this process, the computation is constrained to a specific acquisition time interval, typically between 5 and 15 hours, corresponding to approximately 0.5-1.5 planet's rotations [J. Tollefson et al. (2017)]. This is crucial because if the acquisition time is too short the correlation becomes large, since the displacements in the advected image remain close to the reference one. On the other hand, if the acquisition time is too long, correlations become small due to inherent morphological changes and displacement amplifications arising from non-zonal velocity sources.

3.3.2 The Datasets

The dataset of zonal wind profiles we included in this thesis spans 40 years of observations, from measurements collected from Voyager 2 during its flyby in 1979, to observations performed through the Wide Field Camera 3 (WFC3) onboard Hubble Space Telescope in the years 2009, 2012, 2015, 2016, 2017, and 2019. The 2009 dataset marked the inaugural global mapping effort using WFC3 after its installation during Hubble's final servicing mission and involved the separate observation of two hemispheres on September 18-19 and 22-23 to enhance HST scheduling flexibility. The 2012 dataset took place on September 19-20 and again involved the observation of two different hemispheres. Datasets from 2015 and early 2016 are part of the Outer Planet Atmospheres Legacy (OPAL) program, a project started in 2014 that consists of annual observations of each giant planet to study storm activity, wind field variability, and changes in aerosol distributions and spectral properties. Datasets regarding December 2016, January and February 2017, and April 2019 are part of the Wide Field Coverage for Juno (WFCJ) program, synchronized with perijove passes of the NASA Juno mission. The complete dataset, together with the sources where the data are stored, are presented in Table 3.1:

Table 3.1: Datasets used in this thesis

Dataset	Mission	Program
July 1979[1]	Voyager 2	Voyager
18-23 Sept 2009[2]	Hubble (WFC3)	-
19-20 Sept 2012[2]	Hubble (WFC3)	-
19 Jan 2015[2]	Hubble (WFC3)	OPAL
9-10 Feb 2016[2]	Hubble (WFC3)	OPAL
11-12 Dec 2016[2]	Hubble (WFC3)	WFCJ (PJ3)
11-12 Jan 2017[3]	Hubble (WFC3)	WFCJ (PJ3b)
1-2 Feb 2017[3]	Hubble (WFC3)	WFCJ (PJ4)
9-10 Apr 2019[3]	Hubble (WFC3)	WFCJ (PJ19)

[1] Limaye (1986).
[2] J. Tollefson et al. (2017).
[3] Wong et al. (2020).

3.3.3 Some Preliminary Observations

Given the extensive dataset available, we found it worthwhile to conduct a preliminary analysis on the zonal wind profiles to identify any notable macroscopic features that may characterize them. As a first step, we analyzed the zonal wind profiles listed in Table 3.1 to assess the stability of Jupiter's dynamics over time. Our findings reveal significant temporal stability in Jupiter's winds, with velocities reaching up to 150 m s^{-1} and exhibiting variability of about 10 m s^{-1}[4]. For clarity, we present the analysis limited to the three measurements from 2009, 2012, and 2016; the results are depicted in Figures 3.4, 3.5, and 3.6, respectively, and are fully consistent with the conclusions found by J. Tollefson et al. (2017):

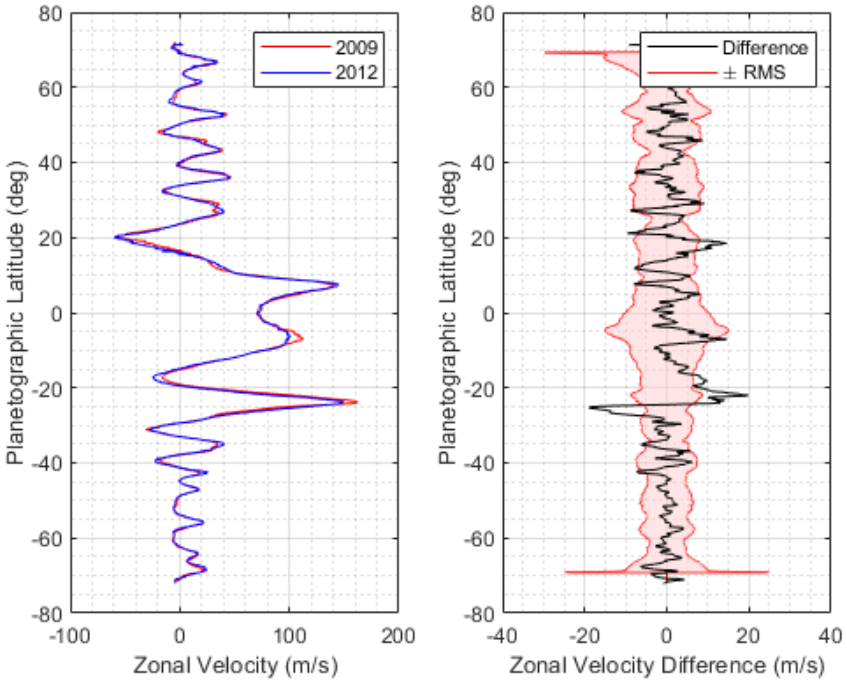

Figure 3.4. Left: Comparison of the average Zonal Wind Profiles (ZWPs) from datasets collected by Hubble in 2009 and 2012. Right: Difference between the compared ZWPs (black) and total RMS (red). Differences outside the red region are significant.

[4]In contrast, Neptune's cloud formations have displayed distinctive dynamics since the derivation of Neptune's Zonal Wind Profile (ZWP) from Voyager 2 data, as documented by (Limaye and Sromovsky, 1991). This may suggest the possibility of different internal driving mechanisms between the two planets.

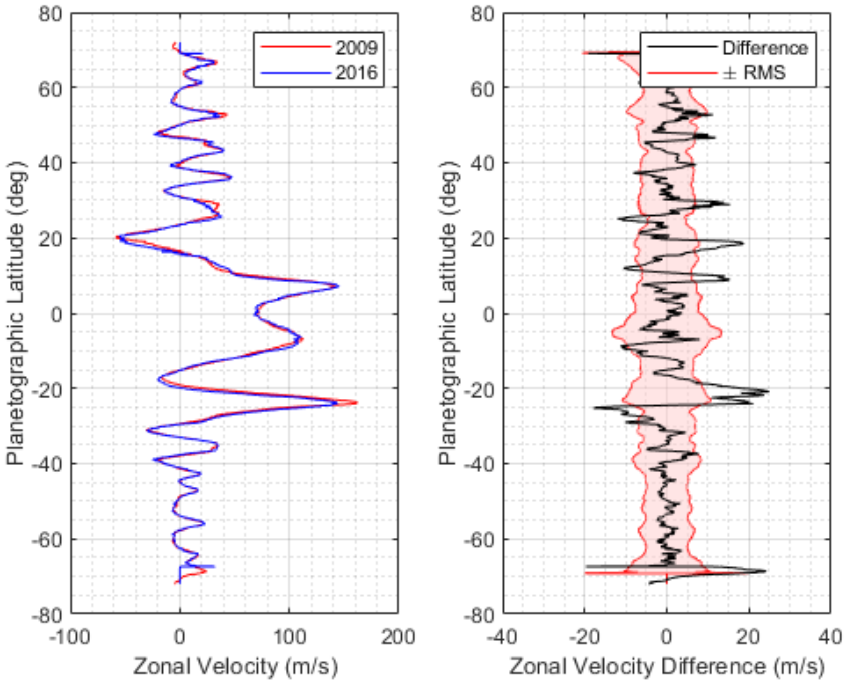

Figure 3.5. Same as Figure 3.4, but considering HST 2009 and HST 2016 datasets.

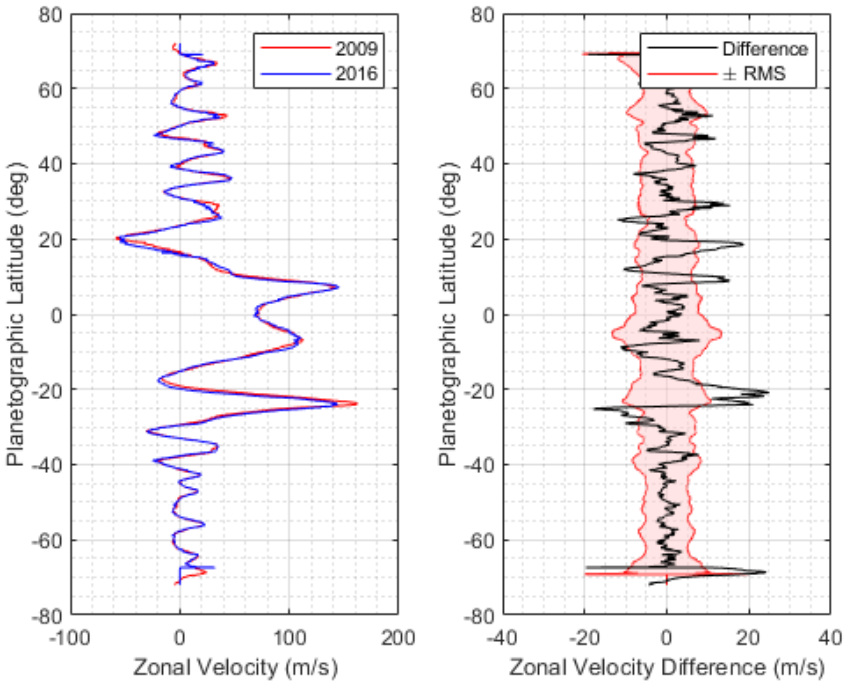

Figure 3.6. Same as Figure 3.4, but considering HST 2012 and HST 2016 datasets.

Data from 2009 and 2012 were collected by dividing Jupiter's map into two hemispheres to optimize the observation time, hence, we conducted a second preliminary analysis by comparing these winds to ascertain whether significant variability may exist between hemispheres. The results, shown in Figures 3.7 and 3.8, respectively, indicate that differences between hemispheres are negligible, suggesting that ZWPs derived from data covering a single hemisphere may be just as accurate as ZWPs derived from data with full global coverage; again, this is fully consistent with the results found by J. Tollefson et al. (2017):

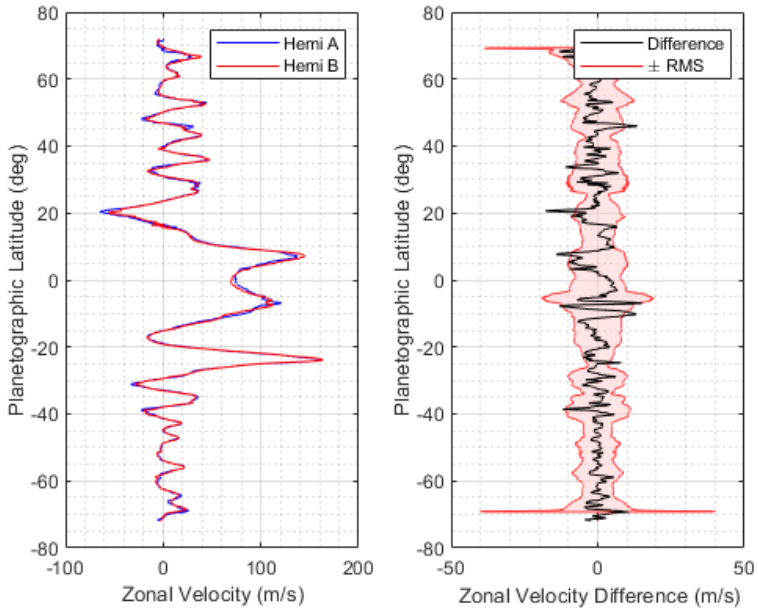

Figure 3.7. Left: Comparison between 2009 ZWPs for different hemispheres.
Right: Difference between the compared zonal wind profiles (black) and total RMS (red).

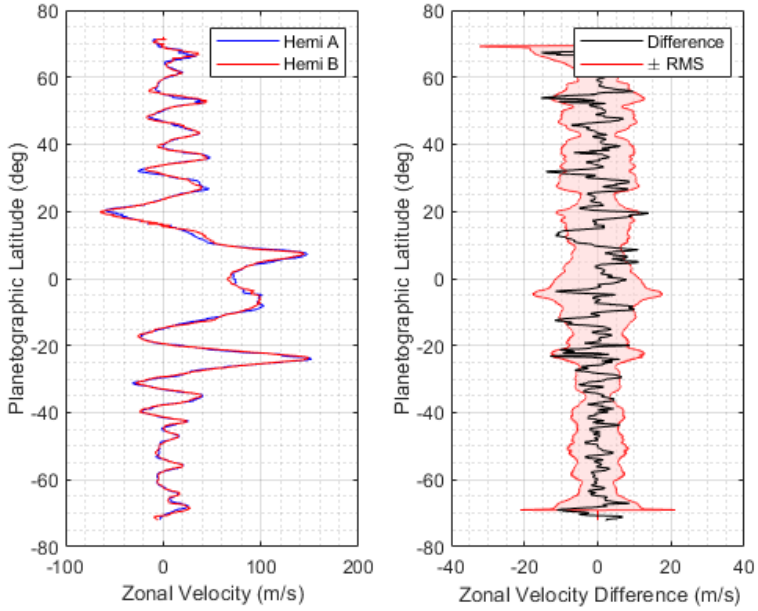

Figure 3.8. Same as Figure 3.7, but considering the 2012 dataset.

3.4 Planetary Radio Occultations

Radio occultation investigations have become a fundamental component of planetary science missions since Mariner 4 reached Mars in 1965 [Arvydas Kliore et al. (1965)] and represent one of the main tools at our disposal to study the atmospheres of celestial bodies, as well as their planetary ring systems. This technique allows us to derive, from time series measurements of the received radio frequency, both neutral gas number density and ionospheric plasma electron density vertical profiles with, in addition, the corresponding profiles of neutral mass density, pressure, and temperature. As stated in Withers et al. (2014), neutral atmospheric profiles obtained through radio occultation experiments offer a superior vertical resolution compared to most other techniques and remain unaffected by instrument calibration issues. In the following sections, we present the main principles underlying radio occultations which are useful for this dissertation.

3.4.1 Geometry of a Radio Occultation

In this section, we introduce the typical geometry of a radio occultation experiment by providing some basic definitions as presented in the work of Withers et al. (2014).
A radio occultation experiment involves two radio elements and a celestial body (Figure 3.9).
The first radio element transmits a signal that passes close to the celestial body before being received by the second; the second element can either serve as a receiver only or retransmit to the first a signal potentially correlated with the one received: the first scenario is called *one-way* radio occultation, the second scenario is called *two-way* radio occultation.
In the case where the radio elements are a satellite and an antenna located on Earth, we define the signal transmitted from the antenna to the satellite as *uplink* and the signal transmitted from the satellite to the antenna as *downlink*. We define *ingress* radio occultation if it occurs when, from the perspective of one radio element, the other radio element disappears behind the celestial body, and *egress* radio occultation if it occurs when the other radio element reappears from behind the celestial body. At any given moment, there is a point along the path of the radio signal closest to the center of mass of the planet. This point, known as *closest approach*, defines the trajectory of the signal, and its altitude determines whether the signal can traverse the atmosphere.
When atmospheric passage occurs, the signal undergoes refraction.
The overall path of the signal can be divided into three steps:

- 1. Initial straight path before entering the atmosphere;
- 2. Non-straight path within the atmosphere;
- 3. Final straight path from the moment of atmospheric exit to the moment of reception.

The radial distance of closest approach that the ray would have in absence of refraction is called *impact parameter*, while the angle which connects points 1. and 3. is called *bending angle*.
We define *baseline* the time interval during which the signal does not traverse the planet's atmosphere. At each timestep, the impact parameter can be determined by knowing the trajectories of the two radio elements.

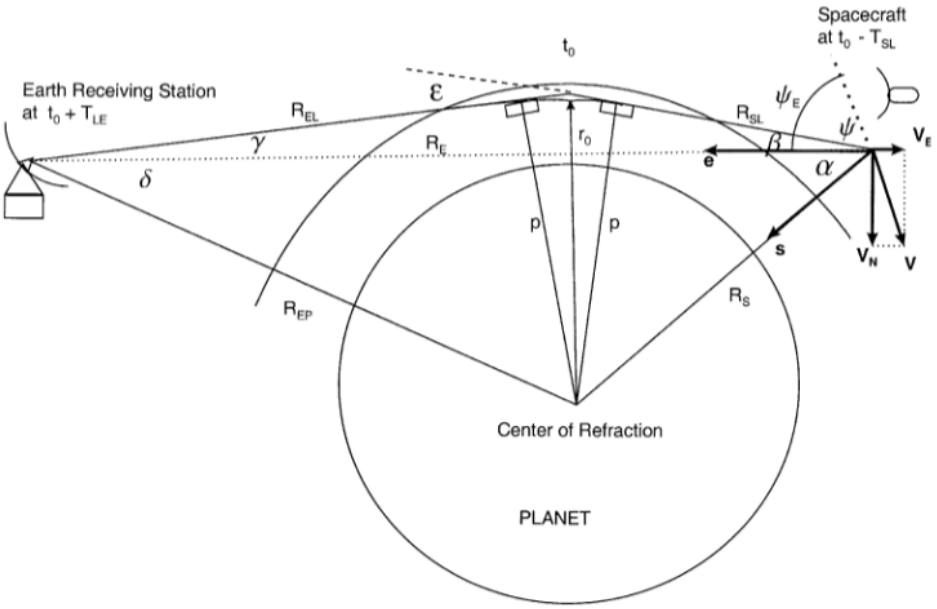

Figure 3.9. Geometry of a radio occultation experiment. Image from AJ Kliore et al. (2004).

3.4.2 Frequency Shifts in Radio Occultations

Planetary radio occultations depend on the interaction of a radio signal and a planetary atmosphere[5]. In most cases, geometrical optic provides a sufficiently accurate description of the interaction, hence the signal can be considered as a ray. The propagation of a radio signal through a planetary atmosphere can be described by the medium's complex refractive index, defined as:

$$\underline{n} = \mu + ik \tag{3.22}$$

where the real part, μ, represents the refractive index and controls the phase speed, and the imaginary part k, called *absorption coefficient*, represents the amount of attenuation the signal undergoes as it passes through the atmosphere. Thus, a variation in the absorption coefficient leads to different signal's attenuations, and a variation in the refractive index leads to ray bending.

In radio occultation experiments it is often convenient to separate the overall atmosphere of the planet into two sub-parts, the neutral atmosphere and the ionosphere, and consider their contributions separately. As illustrated in Withers et al. (2014), the real part of the complex refraction index of neutral atmospheres is always greater than 1, while that of ionospheres is always smaller than 1, thus the complex refractive index may be real or imaginary.
By defining *plasma frequency*, f_p, the quantity:

$$f_p^2 = \frac{N_e e^2}{4\pi^2 m_e \epsilon_0} \tag{3.23}$$

where N_e is the electrons' density, e is the elementary charge, m_e is the electron's mass, ϵ_0 is the permittivity of free space, and f is frequency, we have that a radio signal that propagates from a region of low electron density to a region of high electron density undergoes reflection when its

[5]The term *planetary* is required because, in general, radio occultations can be used in a broad range of applications which extend beyond the study of planetary atmospheres, spanning from ring systems to comets' tails to single dynamical features such as Encelado's plumes.

frequency, f, is equal to f_p, and never propagates when f is smaller than f_p; typically occultation experiments are designed such that the signal's frequency is higher than that of plasma.

Let us consider a generic signal transmitted from one of the two radio elements to the other, at a frequency f_T. Let f_R be the frequency of the signal as received by the other radio element. According to Withers et al. (2014), f_R will not coincide with f_T, instead, it will appear shifted mainly due to classical Doppler shift and refraction during the passage through the planet's atmosphere. Considering small bending angles, the magnitude of this shift can be approximated as illustrated by Hinson et al. (1999):

$$\frac{\Delta f}{f} \approx \frac{v\alpha}{c} \tag{3.24}$$

where v represents the relative speed of the two radio elements. α is the bending angle, and c is the speed of light. The value of Δf may change greatly among different atmospheres, spanning from a few Hz in the rarefied atmosphere of Mars to over 1 kHz at a pressure of 1 bar in the denser atmospheres of Venus, Jupiter, and Titan, as reported by Withers (2010). It is important to underline that Eq. (3.24) holds only for small bending angles, as it neglects some minor geometrical considerations which must be taken into account when the bending angle becomes sufficiently large. Thus, according to Withers et al. (2014), Eq. (3.24) should not be used to derive bending angles from measured frequency shifts.

3.4.3 From Refractivity to Pressure Profile

We define *refractivity*, ν, the quantity:

$$\nu = \mu - 1 \tag{3.25}$$

where μ is the refractive index as defined in subsection 3.4.2.
The refractive index of a planetary atmosphere, hence the refractivity, is determined by the amount of neutral gas and plasma contained inside the atmosphere itself. The refractive index of neutral atmospheres, μ_n, satisfies, as described in Von R Eshleman (1973), the following relation:

$$\mu_n - 1 = \sum_{i=1}^{n} \kappa_i n_{n,i} \tag{3.26}$$

where κ_i and $n_{n,i}$ represent the refractive volume and number density of the i-th constituent, respectively. Given Eq. (3.25), we can rewrite the relation above as

$$\nu_n = \sum_{i=1}^{n} \kappa_i n_{n,i} \tag{3.27}$$

hence $n_n(r)$ can be obtained from $\nu_n(r)$. Note that ν_n does not depend on frequency.
In the case the chemical composition of the atmosphere is known, it is convenient to define a mean refractive volume, κ, such that

$$\nu_n = \kappa n_n. \tag{3.28}$$

Regarding ionospheres, let E be a generic time-varying electric field representing the radio signal sent towards the ionosphere itself:

$$E = E_m \sin(\omega t) \tag{3.29}$$

with E_m maximum amplitude, ω angular frequency and t time.
As explained in Withers et al. (2014), refraction in ionospheric plasma is almost entirely due to electrons, so we can safely consider just the contributions given by electrons.
The inductive current associated to the electric field is given by

$$I_i = N_e q v_e \tag{3.30}$$

with N_e number of charges crossing the area in the considered time interval, q charge of the moving electron measured in Coulombs and v_e velocity of the electron measured in m s^{-1}.
This current generates a force

$$m_e \frac{dv_e}{dt} = qE_m \sin(\omega t) \tag{3.31}$$

that once integrated over v and t gives

$$v = -\frac{qE_m}{m_e} \frac{\cos(\omega t)}{\omega} \tag{3.32}$$

which once put into Eq. (3.30) gives

$$I_i = -N_e \frac{q^2 E_m}{m_e \omega} \cos(\omega t). \tag{3.33}$$

The capacitive current is defined as:

$$I_c = \frac{dD}{dt} = \epsilon_0 E_m \omega \cos(\omega t) \tag{3.34}$$

with ϵ_0 permittivity of free space, hence

$$I = I_i + I_c = E_m \omega \cos(\omega t) \epsilon \tag{3.35}$$

where we define ϵ as

$$\epsilon = \epsilon_0 - \frac{N_e q^2}{m_e \omega^2}. \tag{3.36}$$

The refractive index of a medium is related to its dielectric properties through the relation

$$\mu = \sqrt{\frac{\epsilon}{\epsilon_0}} \tag{3.37}$$

hence we obtain

$${\mu_e}^2 = 1 - \frac{N_e q^2}{4\pi^2 m_e \epsilon_0 f^2}. \tag{3.38}$$

According to Withers et al. (2014), for typical radio occultation experiments in planetary ionospheres the real part of the ionospheric refractive index, μ_e, satisfies $|\mu_e - 1| << 1$, hence by Taylor-expanding and rearranging Eq. (3.38) we finally get:

$$\mu_e - 1 = \nu_e = -\frac{N_e q^2}{8\pi^2 m_e \epsilon_0 f^2} \tag{3.39}$$

which represents the expression of ionospheric refractivity. Note that ν_e depends on frequency.

From this result, it is possible to derive estimates regarding density, pressure, and temperature of the considered atmosphere. The density profile, $\rho(r)$, can be obtained from Eq. (3.27) once the atmosphere's chemical composition is known. The pressure profile, $p(r)$, can be derived from the density profile, the gravitational field, and a proper boundary upper condition using the equation of hydrostatic equilibrium. The temperature profile, T_r, can be derived from the pressure profile, the atmospheric composition, and either Eq. (3.27) or the density profile through a proper equation of state. Thus, refractivity allows to determine the density profile, which in turn allows to determine the pressure profile, which in turn allows to determine, together with refractivity or the density profile, the temperature profile. In the context of our dissertation, this represents a result of primary importance, as it enables to fix a reference pressure at which extracting an estimate of the celestial body's radius corresponding to that given pressure.
This is the keystone that, in Section 4.4, will allow us to compare the shape calculated from gravity experiments with the results obtained from radio occultations.

3.4.4 Sources of Uncertainties in Radio Occultations

A radio occultation experiment represents a complex system wherein multiple components play a role in shaping the overall outcome. As illustrated in Figure (3.10), a large number of electronic components are involved, thus, each of them is a source of noise. Although each of these sources should be accurately considered in an actual radio occultation experiment, in our dissertation we focus on presenting the main sources of uncertainty: *thermal noise* and *phase noise*.

Thermal Noise

Every electronic system operating at a temperature above absolute zero, such as the spacecraft transponder and its Ultra-Stable Oscillator[6], generates a noise component due to the thermal agitation of electrons in the conductor. The uncertainty in frequency due to thermal noise, $\sigma_{thermal}$, is shown in M. K. Simon and Yuen (1983) to be:

$$\sigma_{thermal} = \frac{\sqrt{\frac{2BN_0}{C}}}{2\pi\tau_{thermal}} \tag{3.40}$$

where $2B$ is the noise bandwidth in Hz, N_0 is the noise power density expressed in W Hz^{-1}, C is the signal power in W and $\tau_{thermal}$ is the measurement interval in s. Ground-based electronic equipment responsible for recording signals and transmitting uplinks typically operates under cryogenic conditions to minimize thermal noise. As a result, the signal-to-noise ratio at the receiver consistently surpasses that at the transmitter.

[6] An Ultra-Stable Oscillator (USO) is a highly precise electronic device designed to generate an extremely stable and accurate frequency signal. In the context of interplanetary explorations, USOs play a primary role not only in orbital determination but also in radio occultation experiments, as they allow one-way radio occultations, which are simpler to perform compared to two-way occultations.

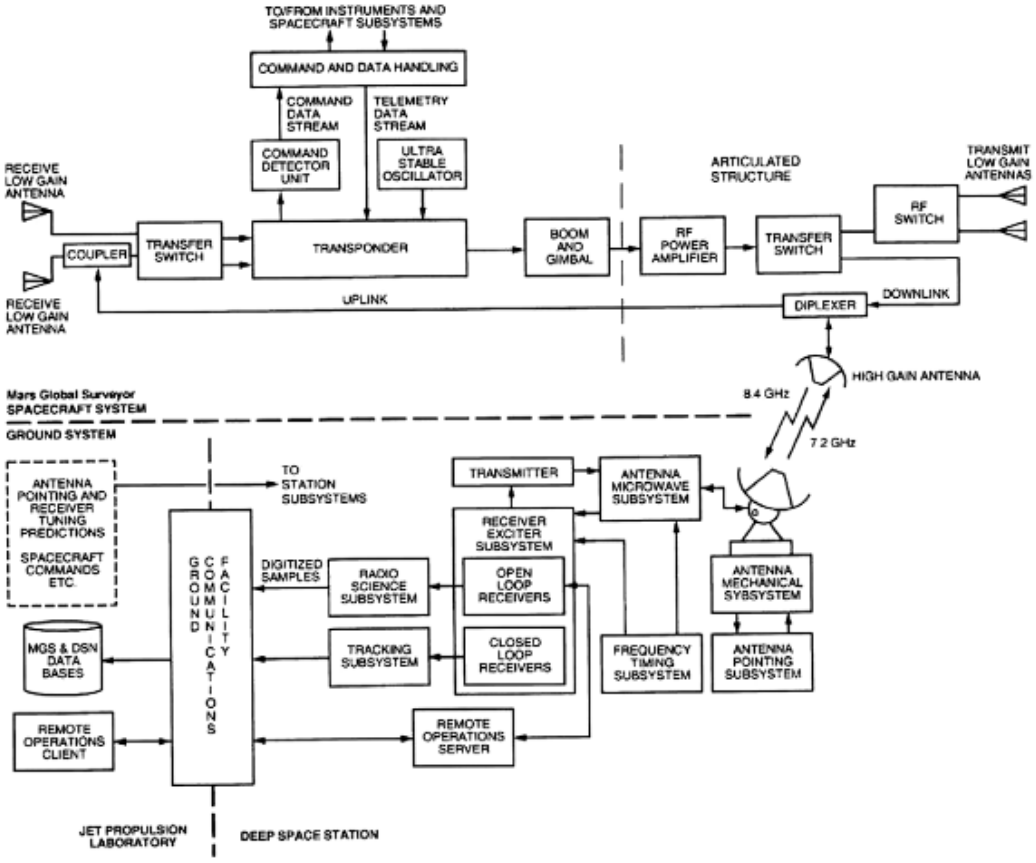

Figure 3.10. Block-diagram of a one-way radio occultation experiment. Image from Withers (2010).

Phase Noise

As the name suggests, phase noise impacts the term describing the phase of a wave.
As explained by Withers (2010), primary contributors of phase noise include USOs instabilities, variations in the refractive indices of neutral atmosphere and Earth's ionosphere, and refraction effects due to solar plasma in the interstellar medium. Ultra Stable Oscillators (USOs), characterized by exceptionally stable output frequencies, are often utilized in space-based probes and satellites. In one-way experiments, instabilities in both transmitting and receiving reference oscillators contribute to phase noise. In two-way experiments, the more stable element acts as the transmitter, while the less stable one serves as the receiver and retransmits a coherent signal. The neutral atmosphere and Earth's ionosphere can also introduce phase noise, which can be mitigated by introducing baseline corrections referencing measurements in vacuum conditions. Turbulence in interplanetary plasma, mainly from the solar corona and solar wind, is a significant source of phase noise, particularly due to variations in plasma column density, as shown in Tinto (2002). These variations, violating geometric optics assumptions, have a relevant length scale of approximately 100 km for signal wavelengths of a few centimeters and a separation of 1 AU, as reported in Withers (2010).

CHAPTER 4

Shape Determination Of Jupiter

In this chapter, we outline the algorithm employed to obtain an updated estimate of Jupiter's shape, leveraging recent findings from both the gravity experiment and radio occultation studies. We start by providing a comprehensive explanation of the process involved in deriving the shape estimate, assuming a rotating rigid body. This foundational step forms the basis of our analysis, allowing us to establish a reference point before considering atmospheric winds.
Following this, we introduce the effects of atmospheric winds into our shape estimation.
We highlight the considerations and adjustments made to the initial estimate, recognizing the dynamic nature of Jupiter's atmosphere and its impact on the planet's overall shape.
Concluding this chapter, we offer a thorough overview of the sources of uncertainty inherent in our results with the aim to provide a comprehensive understanding of the reliability and limitations of our shape model for Jupiter.

4.1 Shape Computation - Rotating Solid Body

The first step of our work consists in developing an algorithm to compute the shape of Jupiter in the approximation of a rotating solid body with constant rotation rate neglecting wind effects. The parameters required for this calculation include the gravitational parameter, GM, the planet's rotation rate, ω_0, the equatorial radius, R_e, the polar radius, R_p, and the zonal harmonics, J_n.

Table 4.1: Bulk parameters used in our study.

Parameters	Values
GM	126.687×10^6 km^{3}s^{-2} (NASA database)
ω_0	1.759×10^{-4} rad s^{-1} (Lindal, Sweetnam, and V. Eshleman, 1985)
R_e	71,492 ± 4 km (Dustin R Buccino et al., 2020)
R_p	66,854 ± 10 km (Lindal, Sweetnam, and V. Eshleman, 1985)[1] 66,896 ± 10 km (Eli Galanti, Yohai Kaspi, and Tristan Guillot, 2023)[2]

[1] Value evaluated at 1 bar pressure level.
[2] Value evaluated at 100 mbar pressure level.

Zonal harmonics	Values
$J_2 \times 10^{-6}$	14,696.5735 ± 0.0017
$J_3 \times 10^{-6}$	-0.0450 ± 0.0033
$J_4 \times 10^{-6}$	-586.6085 ± 0.0024
$J_5 \times 10^{-6}$	-0.0723 ± 0.0042
$J_6 \times 10^{-6}$	34.2007 ± 0.0067
$J_7 \times 10^{-6}$	0.120 ± 0.012
$J_8 \times 10^{-6}$	-2.422 ± 0.021
$J_9 \times 10^{-6}$	-0.113 ± 0.036
$J_{10} \times 10^{-6}$	0.181 ± 0.065
$J_{11} \times 10^{-6}$	0.016 ± 0.111
$J_{12} \times 10^{-6}$	0.062 ± 0.190

Table 4.2: Jupiter's gravity harmonic coefficients (unnormalized and with reference radius 71492 km). The J2 coefficient includes a tidal component predicted from interior models and, according to Durante et al. (2020), is currently estimated at 6.72x10^{-8} with uncertainties of 3σ.

The gravity solutions have been obtained, as presented in Durante et al. (2020), through radio tracking of Juno in the K$_a$ band during perijove transits[1], and represent the most precise results available at present.

The shape of a gaseous celestial body can be calculated along equipotential surfaces.
To begin our computation, we must first select a reference starting point from which to compute the potential. The choice falls either on the equatorial radius or the polar radius. Although the uncertainty in the polar radius is higher than that of the equatorial radius, Eq. (3.18) implies that the effect of the dynamical height is more pronounced at the equator and negligible at the poles. Therefore, in a subsequent stage of our analysis, when we will be considering the effects of zonal winds, it will be convenient to have chosen the polar radius as the reference point. Consequently, we opted for the polar radius at 1 bar pressure level[2] and computed the associated potential

[1] The Juno probe has been orbiting Jupiter since 4 July 2016, completing perijove passes (PJ) once every 53 days. The mid-point of Juno's nominal mission has been reached after PJ17, on 21 December 2018. In that time frame, 10 perijove passes have been dedicated to the study of Jupiter's gravitational field.

[2] The reason we chose to start with the value at 1 bar is because this value is typically adopted in literature as a reference point for gas giants. The value at 100 mbar will come in handy later on.

using Eq. (3.10) and setting the rotation rate equal to ω_0, thus identifying the initial point on our reference potential surface. Following this, we selected a latitude close to the reference and arbitrarily set a new radius on this latitude. By applying Eq. (3.10) again, we calculated a new potential value at this point and latitude. Our approach involves an iterative process wherein we gradually adjust the new radius by comparing the newly calculated potential with the reference. This adjustment iterates until the potential associated with the new radius converges sufficiently close to the reference potential. Convergence is determined when the difference between the newly calculated potential and the reference potential falls below a certain threshold value, chosen considering the achievable accuracy of the gravitational potential itself. The entire algorithm is executed iteratively across the entire latitude window of the planet, which we have set from 90° to −90° with bins of 0.025°. To assess the correctness and accuracy of the obtained result, we compared it with the study done by Dustin R Buccino et al. (2020), as presented in Figure 4.1:

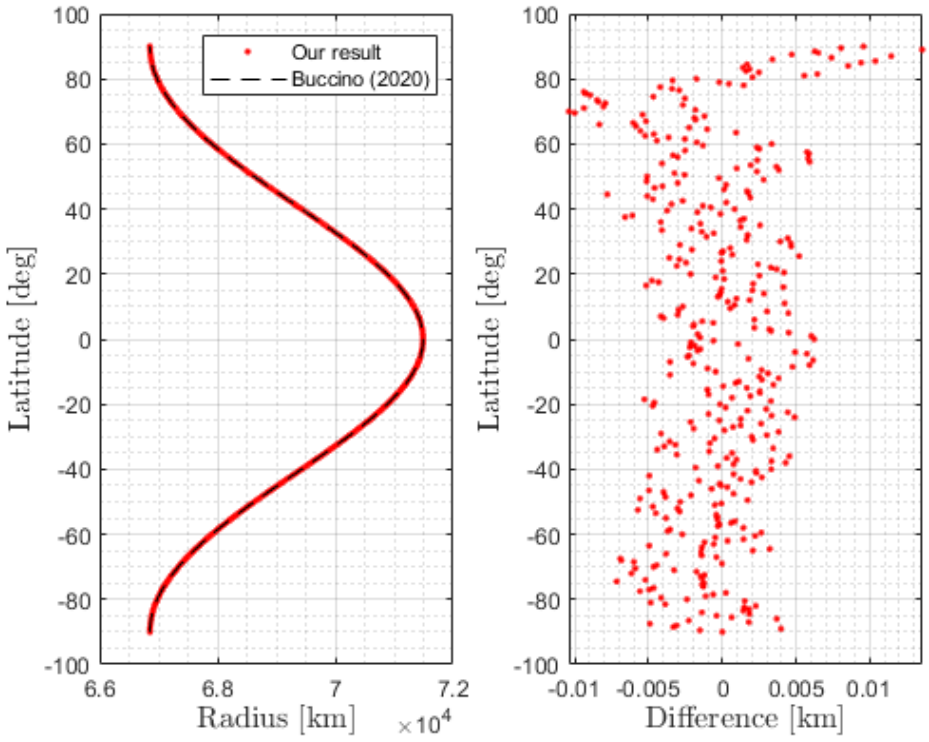

Figure 4.1. The 1-bar equipotential shape of Jupiter obtained in our study and by Dustin R Buccino et al. (2020) in the approximation of a rotating solid body (left) and the corresponding residuals (right). The average difference is of the order of the meter over 10^4 km, corresponding to a relative difference of 10^{-6}. This discrepancy arises from digit approximation choices. Overall, this comparison affirms the correctness of our computational method.

Throughout this process, we utilized the zonal coefficients listed in Table 4.2, which represent a significant advancement in accuracy compared to the previously available data. Before proceeding with the implementation of the algorithm, we deemed it valuable to investigate the contribution of these zonal coefficients to the overall shape. This involved studying the impact of various gravitational coefficient combinations, considering both even and odd terms. This analysis is presented in the following subsection.

4.1.1 Effects of Gravitational Harmonics

Following Juno's arrival at Jupiter on July 4, 2016, significant advancements were made in our understanding of the planet's gravitational field. In the initial two orbits alone, the knowledge of the gravitational field improved, according to Folkner et al. (2017), by a factor of five. Subsequently, with the addition of three more orbits, this improvement escalated to approximately a hundredfold, marking the first-time detection of odd zonal harmonics, as presented in Luciano Iess et al. (2018). To evaluate the impact of gravitational harmonics on the shape, we ran the algorithm described in Section 4.1 selecting the following set of coefficients:

Combination	Gravitational coefficients
1	J_2 and J_4
2	J_2, J_4, and J_6
3	J_2, J_4, J_6, and J_8
4	J_2, J_4, J_6, J_8, J_{10}, and J_{12}
5	J_3, J_5, J_7, J_9, and J_{11}

Table 4.3: Gravitational coefficients' combinations chosen for our analysis.

Aside from the dominant ellipsoidal effect produced by J_2 [3], the greatest effect is that of J_4 which pulls the equipotential surface inward in mid-latitude regions by ~ 37 km, as shown in Figure 4.2:

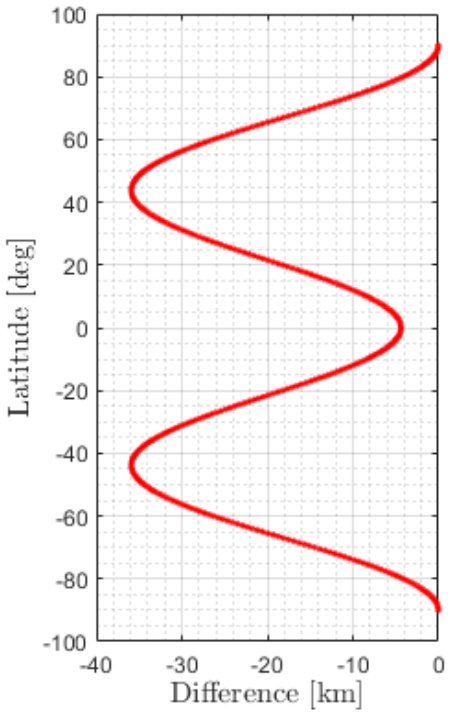

Figure 4.2. Difference between the shape computed including J_4 and that of a reference ellipsoid. We can appreciate the symmetry relative to the equator, a characteristic of the even-numbered gravity coefficients greater than J_2.

[3] All Solar System planets, and the Sun, are oblate due to their rotation and exhibit a significant J_2 coefficient. Jupiter, in particular, with a rotation period of 9 hours, 55 minutes, and 29.71 seconds, is one of the most oblate planets in the Solar System, along with Saturn. J_2 is also valuable for modeling the behavior of a ring system.

The impact of the J_6 coefficient is approximately one order of magnitude smaller, resulting in a change of about 4 km, as shown in Figure 4.3:

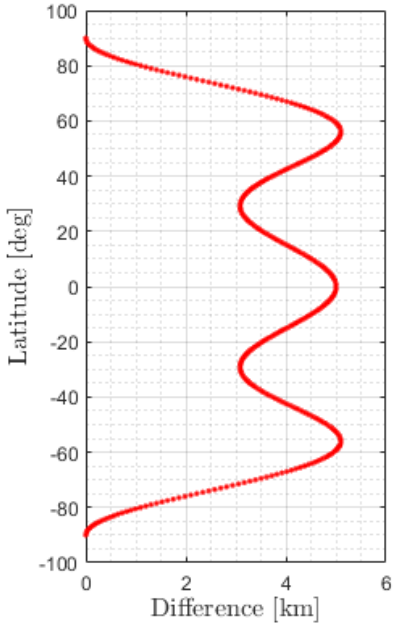

Figure 4.3. Effects of J_6. The difference is between the shape up to J_6 and the shape up to J_4.

Considering the highest order terms, the influence of the J_8, J_{10}, and J_{12} coefficients on the shape is minimal, with changes of less than 1 km, as shown in Figure 4.4:

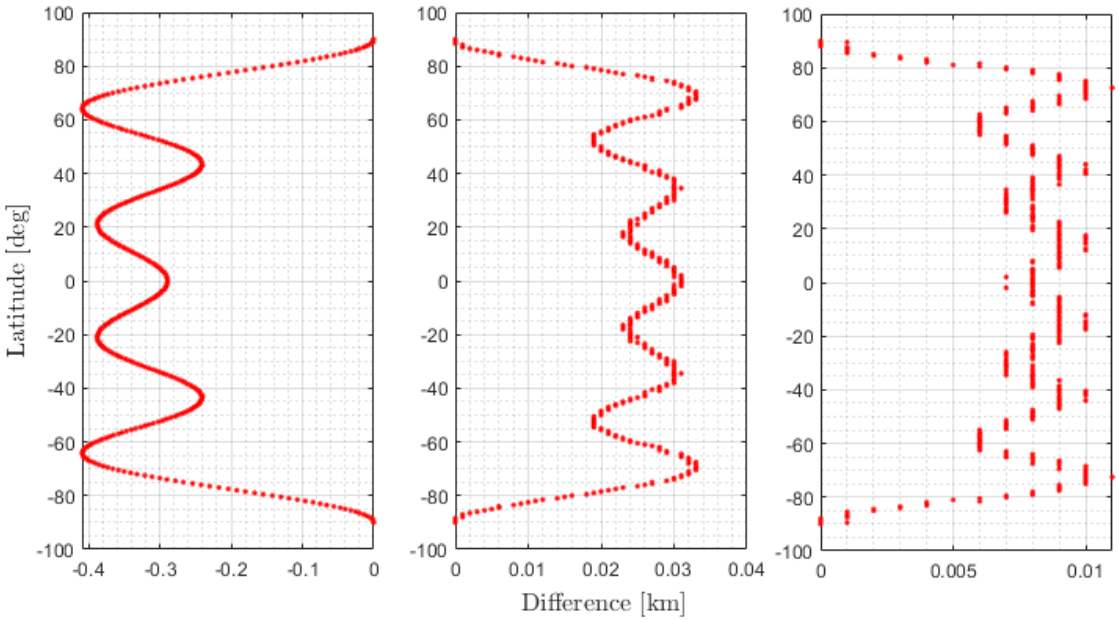

Figure 4.4. Effects of J_8 (left), J_{10} (centre), and J_{12} (right). For each panel, the difference is computed between the shape up to the J_n term and that up to the term J_{n-2}.

Finally, concerning the odd zonal harmonics $J3$, $J5$, $J7$, $J9$, and $J11$, their combined contribution to the shape is minimal, even smaller than the effect of $J8$.

4.2 Shape Computation - Effect of Cloud-Level Winds

We proceed with our main study, to obtain an estimation of the dynamical height, which essentially quantifies the effects on the shape due to zonal winds. To achieve this, we run again the algorithm presented in Section 4.1 introducing, instead of the solid rotation rate ω_0, the full rotation rate ω defined as in Eq. (3.5), and performing the computation using Eq. (3.3), (3.4), and (3.6). As a wind model, we selected the zonal wind profile measured on 9 and 10 April, 2019 using HST's WFC3, and presented in Wong et al. (2020). The corresponding zonal wind profile is illustrated in Figure 4.5:

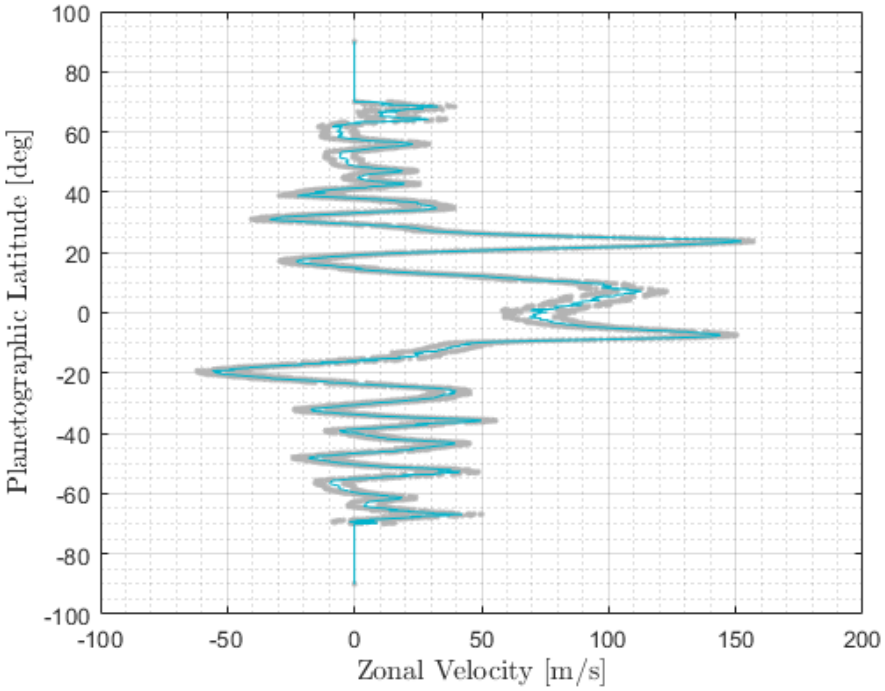

Figure 4.5. Jupiter's 2019 zonal wind profile as measured by Hubble's Wide Field Camera 3 (azure) and its associated uncertainty (light grey).

The output of this computation is a second shape, this time including also the effects of cloud-level winds. We hence subtract to this second shape the one we calculated in Section 4.1, obtaining the dynamical height. This quantifies the perturbations on the shape associated with a rotating rigid body due to the effects of the zonal winds. The result is shown in Figure 4.6 and is consistent with the study performed by Eli Galanti, Yohai Kaspi, and Tristan Guillot (2023).

In the upcoming section, we investigate the extent to which the parameters involved in the equations contribute to the obtained results.

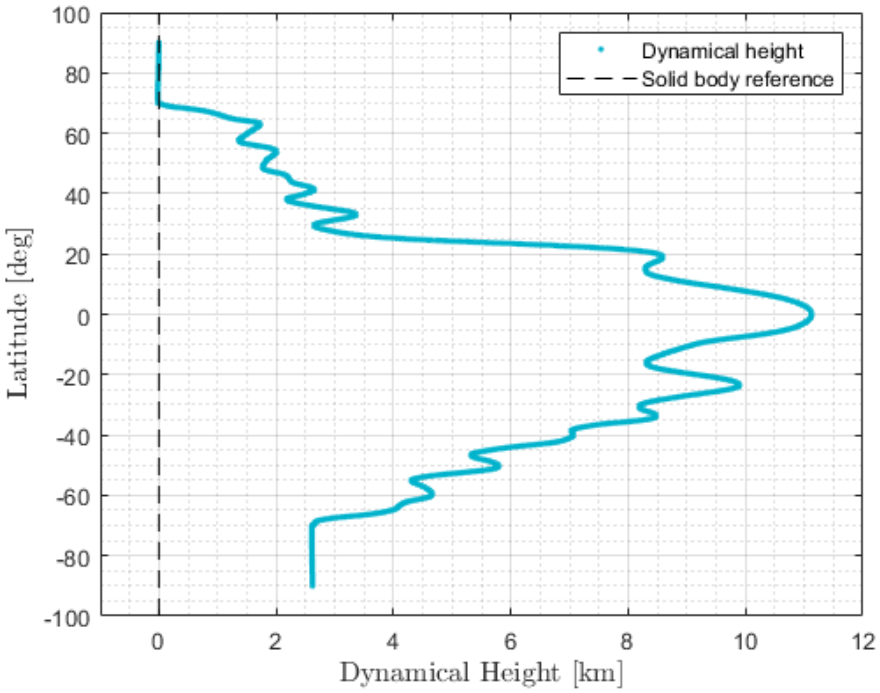

Figure 4.6. Our obtained dynamical height considering Hubble's 2019 zonal wind profile.
The black dashed line represents the reference level which corresponds to the shape computed assuming rigid body rotation only.

4.3 Sources of Uncertainty

In this first part of the computation, the main sources of uncertainty are associated with the polar radius and the zonal wind profile, both quantities not accurately known. In this section, we present how these uncertainties affect the result concerning the shape and the dynamical height.

4.3.1 Polar Radius

The polar radius is known to be within an uncertainty of ± 10 km, according to Lindal, Sweetnam, and V. Eshleman (1985). To analyze how this may affect the shape, we ran the algorithm two additional times, setting the polar radius equal to R_p - 10 km and R_p + 10 km, respectively, and compared the obtained shapes with the one we obtained in Section 4.2. We found that the uncertainty in the polar radius translates into a maximum variation in the shape of 11.7 kilometers, realized at the equatorial radius, and an average variation in the dynamical height within a range of 6 meters, as illustrated in Figures 4.7 and 4.8, respectively:

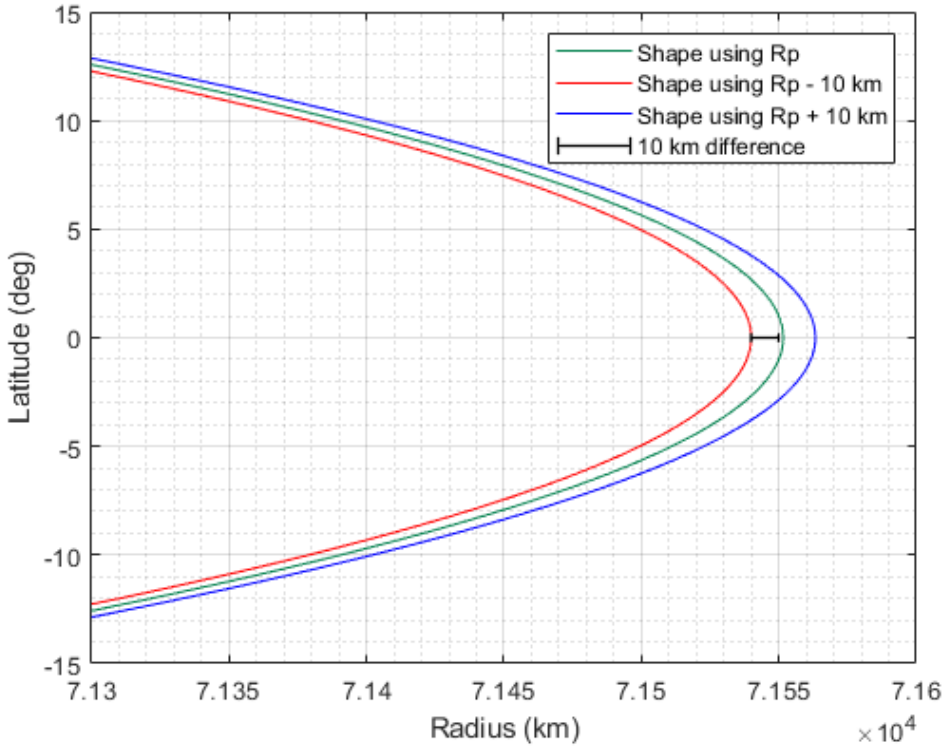

Figure 4.7. Resulting shapes considering the average polar radius R_p (green), and a polar radius equal to R_p - 10 km and R_p + 10 km, red and blue, respectively; black horizontal line represents a difference of 10 km.

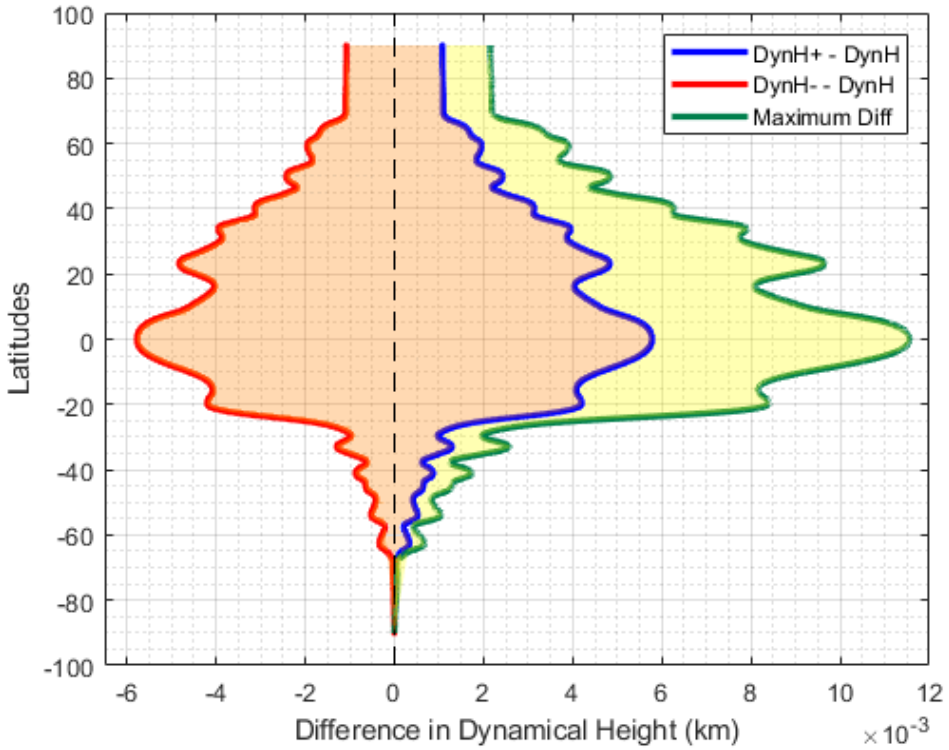

Figure 4.8. Differences in dynamical heights due to the uncertainty associated with the polar radius. The black dashed line represents the reference level, derived using the average value of R_p. This value is subtracted from the results obtained with R_p - 10 km (red) and R_p + 10 km (blue), respectively. The green curve represents the maximum difference between the two dynamical heights calculated using R_p + 10 km and R_p - 10 km.

4.3.2 Cloud-level Winds

The observed cloud-level winds carry an uncertainty which, according to Fletcher et al. (2020) and J. Tollefson et al. (2017), is estimated to be up to ± 20 m s^{-1}. To analyze the effects of these uncertainties, we ran the algorithm considering our selected zonal wind profile ± the RMSE associated with each latitude. This information is properly included in the Hubble's 2019 dataset openly accessible at Mikulski Archive Space Telescope database[4]. The obtained result, presented in Figure 4.9, shows that the zonal wind profile's RMSE may translate into an uncertainty in the dynamical height up to 5 kilometers. Afterward, we pondered the extent of variability in the dynamical height range between consecutive observations. To investigate this, we considered the entire database presented in Section 3.3 and calculated the dynamical height for each of the zonal wind profiles. The obtained results are presented in Figure 4.10. We can observe that, among all the obtained dynamical heights, the one computed using the zonal wind profiles measured by Voyager 2 in 1979 appears to deviate the most from the others. This might suggest a systematic uncertainty in the data, stemming from a hypothetical higher measurement uncertainty associated with the Voyager probes. The same feature reflects, naturally, in the shapes, as shown in Figure 4.11 which represents the difference between a reference shape, obtained by averaging all the obtained shapes, and the lower and upper limits respectively. The upper limit is represented by the shape obtained from Hubble observations taken on February 02, 2017, while the lower limit is represented by the shape obtained from the zonal wind profiles measured by Voyager 2.

[4]cf. https://archive.stsci.edu/hlsp/wfcj.

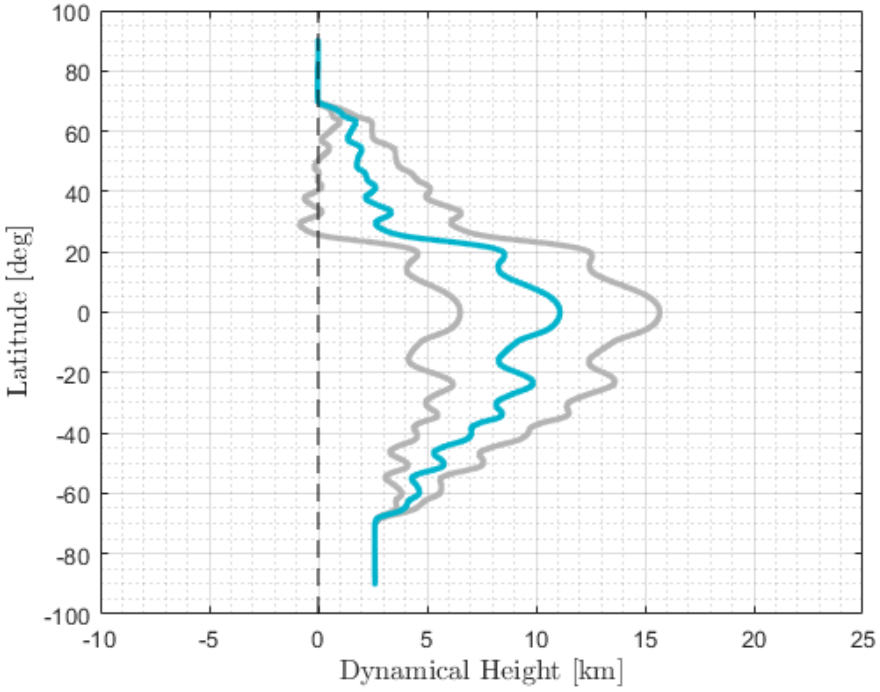

Figure 4.9. Dynamical height computed in Section 4.2 (azure) with its associated uncertainty (light grey).

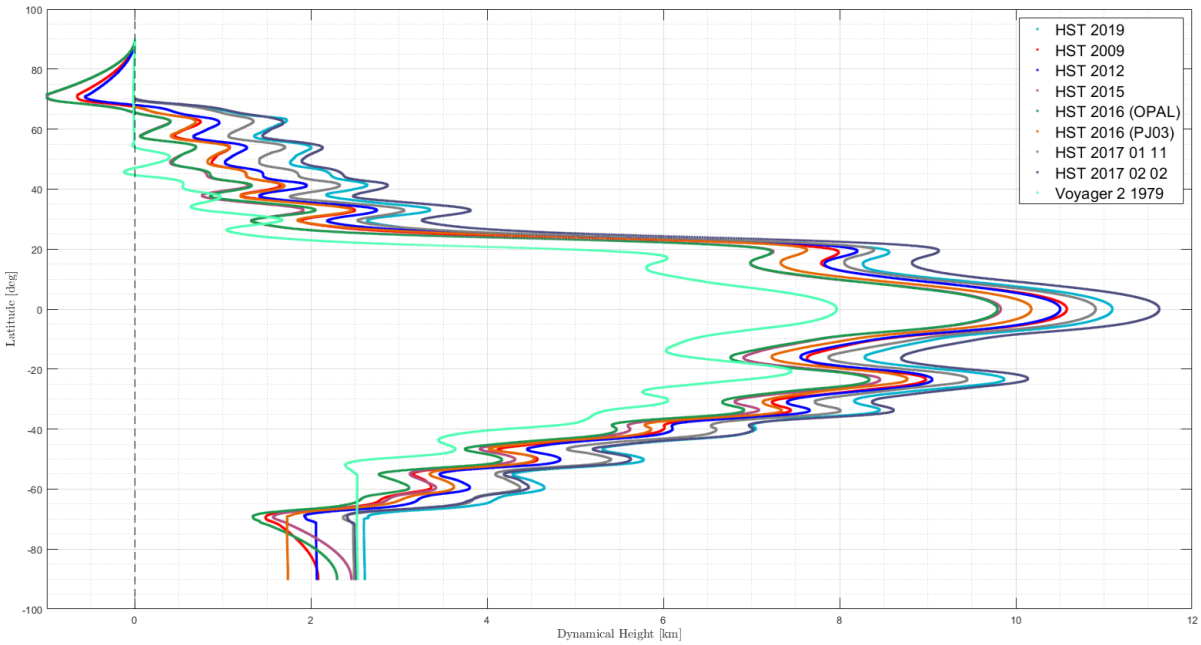

Figure 4.10. Results on the dynamical heights obtained by considering all the zonal wind profiles presented in Section 3.3.2. We can observe that the dynamical height associated with Voyager 2 deviates more significantly from the others.

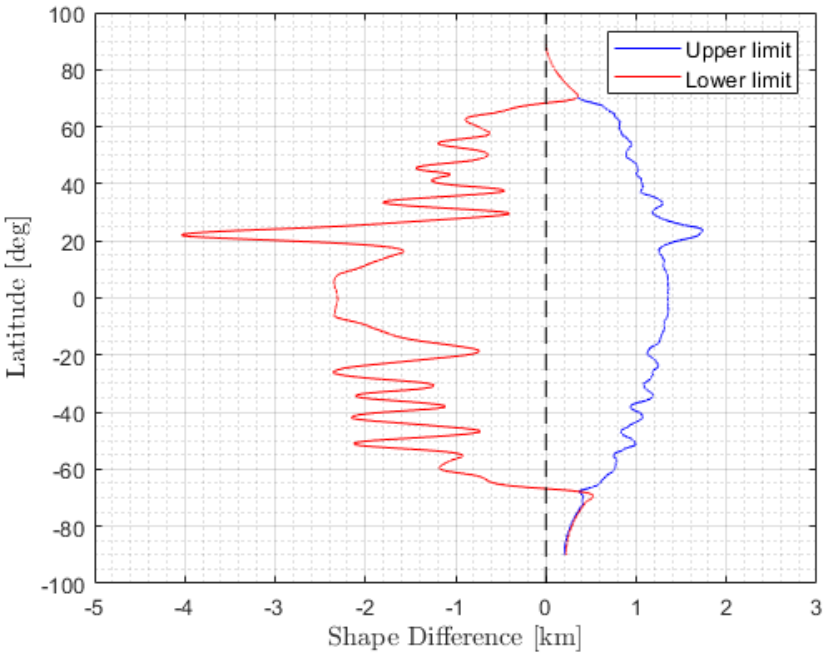

Figure 4.11. Differences in shape considering the wind models presented in Section 3.3.2.
The dashed black line represents the reference profile obtained by averaging all the calculated shapes

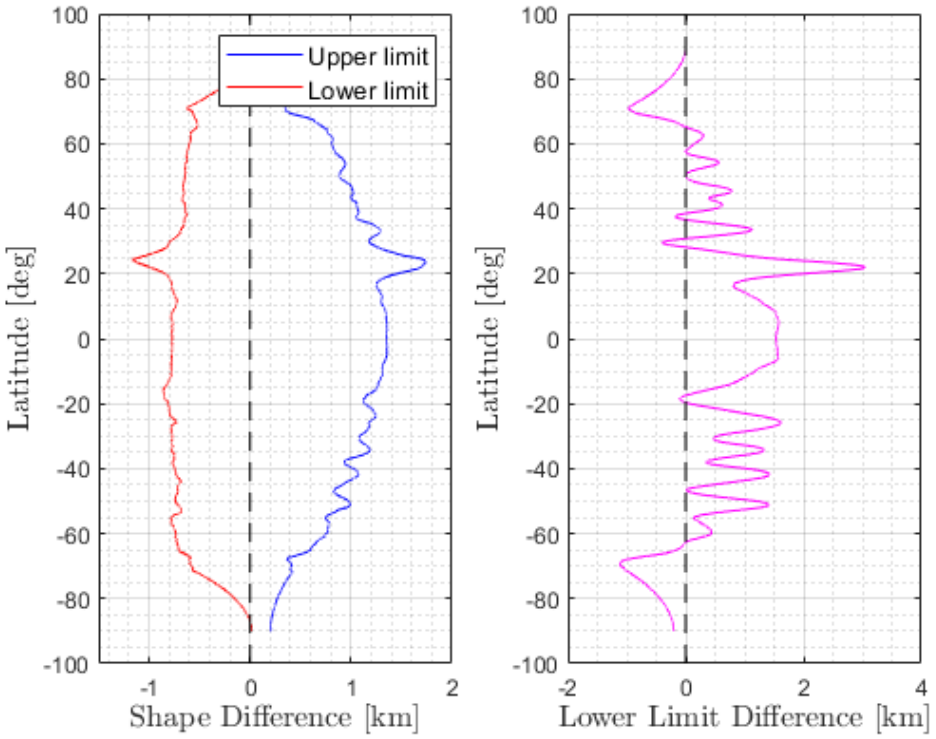

Figure 4.12. Left: Same as Figure 4.11, but considering only Hubble dataset.
Right: Difference between lower and upper limit discrepancies.

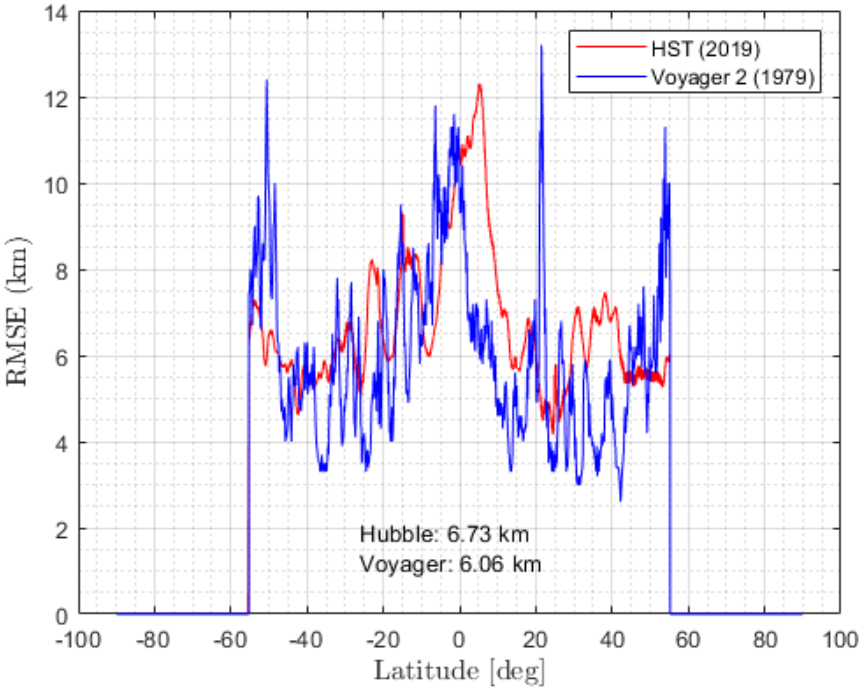

Figure 4.13. Analysis of the RMSE profiles associated with Voyager 2 (blue) and HST (red) datasets. The two RMSE profiles are similar. On the bottom-mid are reported the average RMSE values.

Indeed, upon recalculating the shapes while excluding data from Voyager 2, we observe a discrepancy towards the lower end that better aligns with the one observed for the upper end, as depicted in Figure 4.10. Consequently, we proceeded to examine the RMSE profiles associated with data from both Voyager 2 and the Hubble Space Telescope. The results, shown in Figure 4.13, indicate that the two spacecraft share a similar RMSE profile. Hence, the larger observed discrepancy shouldn't be attributed to differing RMSE capabilities but may genuinely reflect characteristics of Jupiter's atmosphere. From our analysis, we can infer that the uncertainty in the shape, and therefore in the dynamical height, derived from zonal wind data is within 5 km.

4.3.3 Rotation Rate

Extensive ground-based radio observations allowed, as detailed by Dessler (1983), the determination of Jupiter's rotation rate to high precision, yielding a value of 9 hr 55 min 29.71 s. This value is commonly accepted as the planet's internal rotation period. In 1997, Higgins et al. (1997) suggested a slight deviation of 0.025 seconds to this rotation rate, but magnetic field data from Galileo did not support this claim [Russell, Yu, and Kivelson (2001)]. Given this, we opted to explore how this potential additional uncertainty might impact the results. To do so, we re-ran the algorithm, setting a rotation rate that accounts for the aforementioned hypothesized uncertainty. The analysis revealed a variation in the dynamical height of the order of 10^{-6} km, as shown in Figure 4.14:

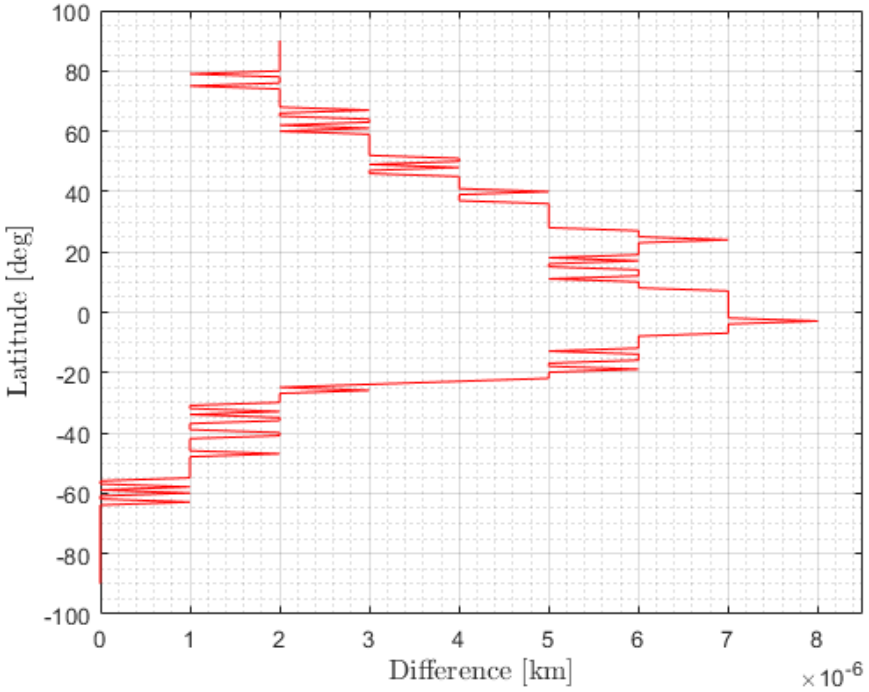

Figure 4.14. Difference in the dynamical height due to the hypothetical uncertainty in the rotation rate. The red curve is obtained by subtracting the dynamical height profile obtained considering the nominal rotation rate from the dynamical height profile obtained considering the hypothetical rotation rate.

As expected, considering a rotation rate 0.025 seconds lower implies a slightly higher value for the shape radius, but such uncertainty corresponds to a fraction of just 1 over 10^4. This, added to the fact that the existence of such uncertainty remains subject to debate, leads us to conclude that this (hypothetic) source of uncertainty may be considered negligible, hence it will not be considered in the remaining part of our work.

4.4 Shape Update including Radio Occultations

The final step involves comparing the overall shape with the results obtained through radio occultation experiments. These experiments measure atmospheric refraction by transmitting a radio signal from a spacecraft to Earth. The signal scans the atmosphere at a specific geographic location and provides a vertical profile of density, pressure, and temperature as a function of distance from the planet's center. This information can be exploited to estimate the radius at which the equipotential condition is met and derive a shape that optimizes the fit between gravity and radio occultation measurements. To do this, we implemented an algorithm based on the Levenberg–Marquardt method[5] using Matlab's function *fsolve()*[6], specifically useful to solve non-linear least squares problems. The available radio occultation data, reported in Table 4.4, were collected by Pioneer 10, Pioneer 11, Voyager 1, and Voyager 2. Additionally, we included the new preliminary results gathered by Juno and presented in Caruso et al. (2023). Note the very few radio occultation data available up to now: just two for Pioneer 10, one for Pioneer 11, two for Voyager 1, one for Voyager 2, and three for Juno. Figure 4.15 shows the overall shape at 100 mbar which best fits the occultation data:

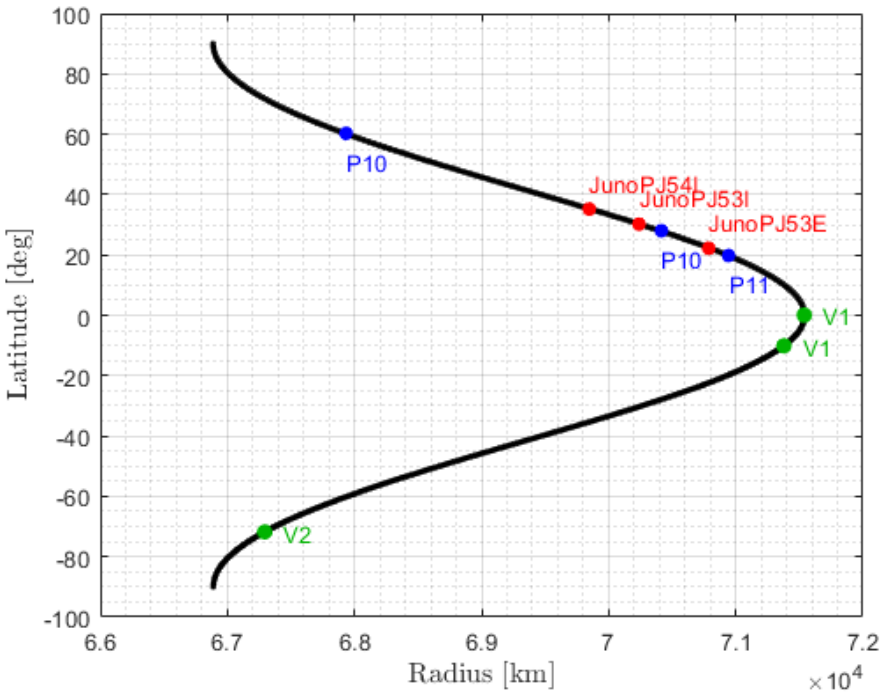

Figure 4.15. Overall shape inferred from radio occultations. Colored dots represent the radii obtained from occultation measurements of Pioneer 10 (P10), Pioneer 11 (P11), Voyager 1 (V1), Voyager 2 (V2) and Juno at 100 mbar. The 'PJ53' and 'PJ54' flags for Juno mark perijove 53 and perijove 54, respectively.

Now, the polar radius no longer represents the starting point of our algorithm but rather the endpoint, as it is estimated as the last point of the shape that best fits the radio occultation results. The obtained estimated polar radii at 100 mbar[7] amount to 66,887 km and 66,890 km considering the northern and the southern hemispheres, respectively. On the other side, the polar radius derived from radio occultations amounts to 66,896 ±5 km; This, including the uncertainty

[5] cf. https://people.duke.edu/~hpgavin/ExperimentalSystems/lm.pdf.
[6] cf. https://it.mathworks.com/help/optim/ug/fsolve.html.
[7] The 100 mbar value now is due to its assumption as a common reference value in radio occultation experiments. As long as the assumption illustrated in Section 4.1 holds, this does not produce any inconsistency.

associated with the polar radius, ensures that our result falls within the confidence interval.

Mission	Latitude	Radius at 100 mbar
Pioneer 10	60.3°	67,933.93 ± 5 km[1]
	28.0°	70,415.08 ± 5 km[1]
Pioneer 11	19.8°	70,943.95 ± 5 km[1]
Voyager 1	0.07°	71,538.61 ± 5 km[1]
	-10.1°	71,378.73 ± 5 km[1]
Voyager 2	-71.8°	67,293.64 ± 5 km[1]
Juno	35.2°	69,847.7 km^2
	30.2°	70,238.8 km^2
	22.2°	70,787.4 km^2

[1] (Eli Galanti, Yohai Kaspi, and Tristan Guillot, 2023).
[2] No uncertainties available yet.

Table 4.4: Radio occultation data available for this study.

Figure 4.16 shows our results concerning the dynamical height:

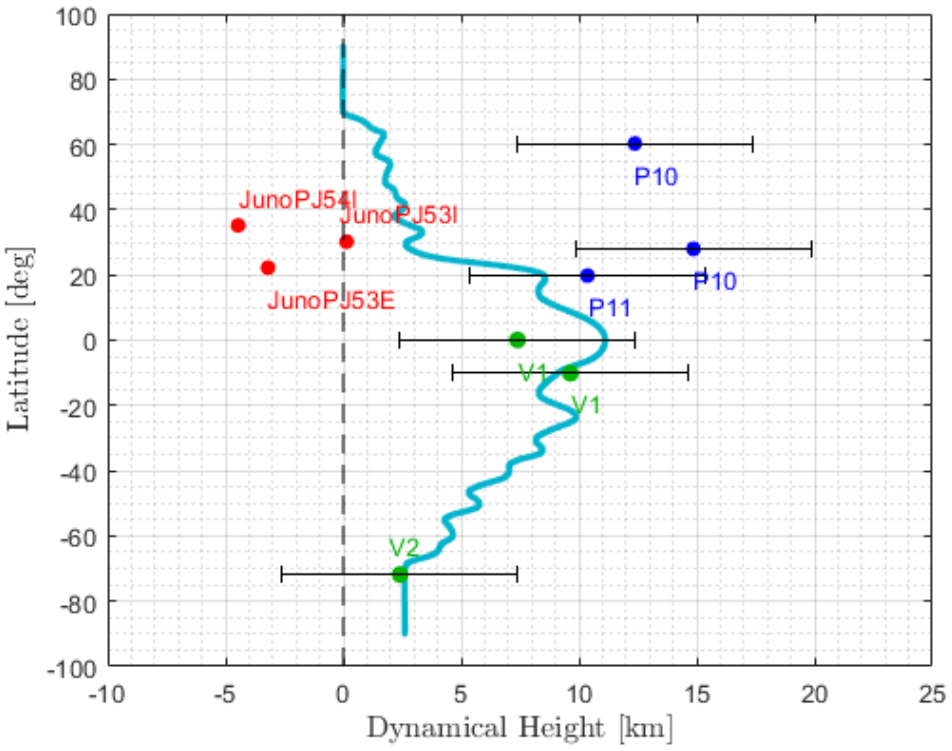

Figure 4.16. Dynamical height considering Hubble 2019 results.
Colored points represent radio occultation data. Horizontal bars represent the uncertainties associated with radio occultations, as reported in Table 4.4.

4.5 Sources of Uncertainty

As a last step, we evaluate the effects on the total shape that best fits the radio occultations, due to the effects of the uncertainties regarding the gravitational harmonics and the cloud-level winds. When including radio occultation measurements, our algorithm adjusts the shape obtained in Section 4.2 through the method described in Section 4.4, and provides an estimate of the polar radius that is the most possible consistent with both gravity and radio occultation results. If the gravitational coefficients or zonal winds change, the shape changes, affecting the dynamical height, and this, in turn, leads to a different estimate of the polar radius, hence to a different estimated shape and dynamical height.

4.5.1 Effects of Gravitational Harmonics

We now quantify the effects of the uncertainties associated with the gravity harmonics into the corresponding shape and dynamical height, in particular into the polar radius estimate. Given that, as we showed in subsection 4.1.1, the contributions of J_2 and J_4 are significantly larger compared to the other gravitational coefficients, we focus solely on these two performing two separate analyses, the first one including only the uncertainties related to J_2, and the second one by fixing J_2 to its average value and considering only the uncertainties related to J_4. This allows us to isolate the individual contributions and assess the uncertainties associated with each of the two gravitational terms separately. The results of our analysis are presented in Figure 4.17:

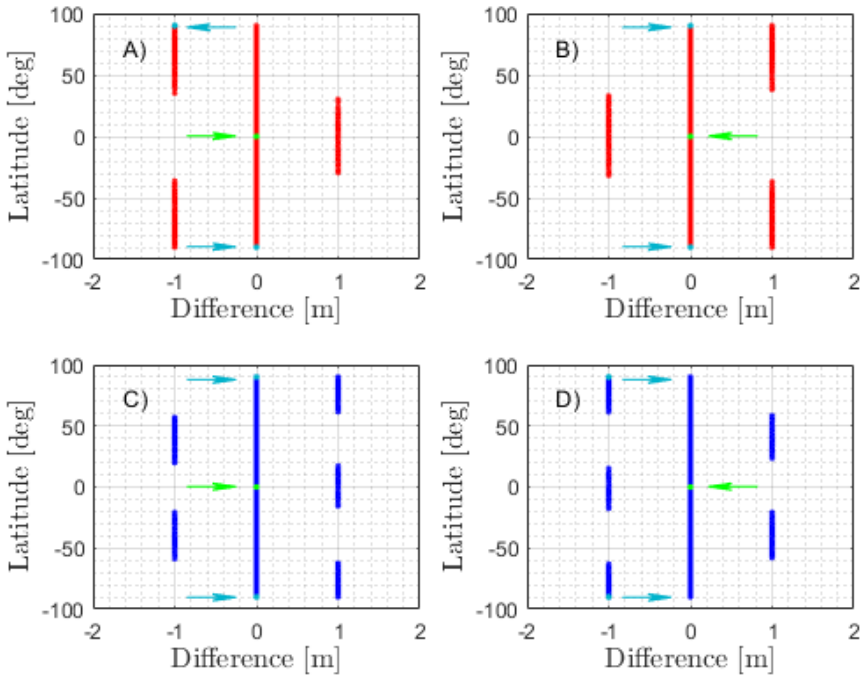

Figure 4.17. Variations in the shape considering the uncertainties on the gravity coefficients listed in Table 4.2. Panel A): Shape computed using $J_2 + \Delta J_2$ minus the shape obtained considering the average J_2. Panel B): Same as A), except we used $J_2 - \Delta J_2$ instead of $J_2 + \Delta J_2$. Panel C): Shape computed using $J_4 + \Delta J_4$ minus the shape obtained considering the average J_4. The J_2 coefficient is set to its average value. Panel D): Same as C), except we used $J_4 - \Delta J_4$ instead of $J_4 + \Delta J_4$. Points corresponding poles equator are highlighted in azure and green, respectively, and flagged with arrows of the same color.

.

As we can see, the uncertainties on both J_2 and J_4 produce a difference in the estimated polar radius of just 1 meter, which can be considered negligible. This underscores the remarkable precision of the gravitational measurements obtained from the Juno orbiter. We can appreciate the harmonic behavior originating from spherical harmonics.

4.5.2 Effect of Cloud-level Winds

To evaluate the effects of the uncertainties associated with the selected zonal wind profile, we ran the algorithm including the uncertainties listed in Wong et al. (2020).
The result is shown in Figure 4.18:

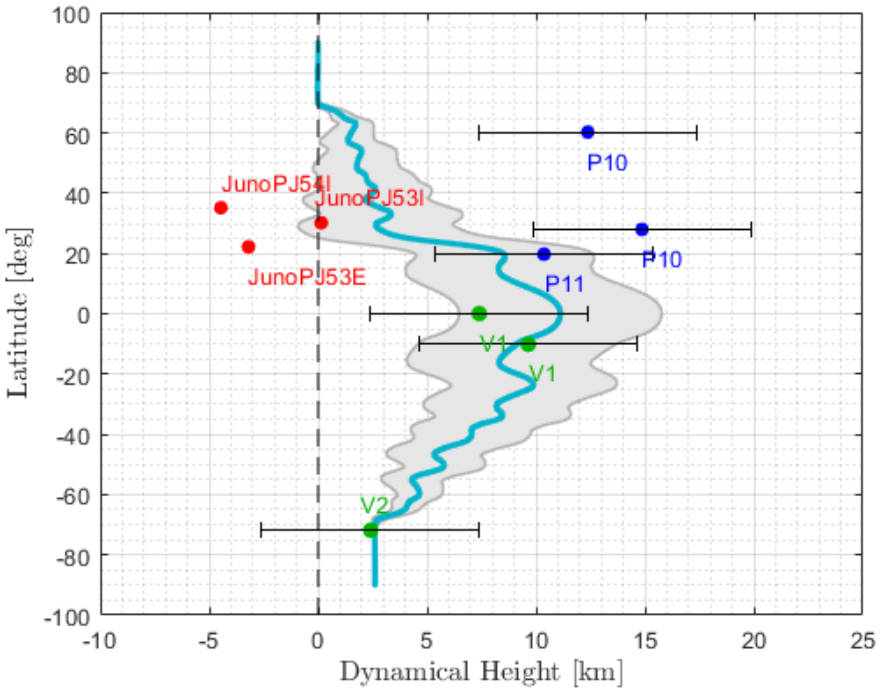

Figure 4.18. Dynamical height considering Hubble 2019 results (azure) and total RMSE associated with each latitude (light gray region). Colored points represent radio occultation data. Horizontal bars represent the uncertainties associated with radio occultations, as reported in Table 4.4.

It appears to be an improvement in the correlation between the computed dynamical height and the radio occultations, concerning the current results in literature. The most recent findings on this topic, as outlined in the study of Eli Galanti, Yohai Kaspi, and Tristan Guillot (2023), showed that only two out of the six radio occultation measurements were in good agreement with the results of gravity experiments. Notably, four out of six radio occultation measurements fell completely outside the estimated dynamical height value, exhibiting an opposite sign, indicating that other factors might have contributed to the discrepancy. The result of our study suggests that four out of the six prior Juno measurements are now consistent with the estimated dynamical height, and all six now exhibit the same sign. Additionally, the computed RMSE improved, dropping from $\sim$ 9 km to $\sim$ 5.6 km. However, it should be noted that the uncertainties related to the radio occultations are still significant, of the same order of magnitude as the values characterizing the dynamical height and the uncertainty related to the polar radius. Furthermore, the three new Juno results, which have certainly contributed to improving the estimates, are still in the preliminary phase and lack the associated uncertainty. Therefore, further studies on future radio occultations are necessary, to both reduce the uncertainties and better constrain the results.

CHAPTER 5

Conclusions

We have presented a methodology to compute the precise shape of Jupiter, taking into account the up to date gravity experiment results from Juno and radio occultation measurements performed with Pioneer 10, Pioneer 11, Voyager 1, and Voyager 2 probes, including the most recent preliminary findings from Juno itself. Additionally, we included the 2019 cloud-level winds measurement obtained through HST Wide Field Camera 3, along with data from previous years (2009, 2012, 2015, 2016, and 2017) as well as measurements from the Voyager 2 probe collected in 1979. In the first part of our work, we provided a precise estimation of the perturbation effect of cloud-level winds on the shape, known as the dynamical height. To achieve this, we implemented an algorithm that computed two shapes: a first shape considering rotating rigid body approximation and a second shape including the effects of zonal winds. By subtracting the former from the latter, we obtained the dynamical height. Subsequently, we proceeded to evaluate the effects on the computed shape and dynamical height due to the gravitational harmonics, the uncertainty of the polar radius, the zonal wind profiles, and the rotation rate of the planet.

The effects related to the gravitational harmonics were assessed under the rotating rigid body approximation, to isolate their contribution from other sources of uncertainty. Our analysis revealed that after the ellipsoidal effect caused by the J_2 coefficient, the gravitational coefficient J_4 produces the largest effect, pulling the equipotential surface inward by approximately 37 km at mid-latitude regions. In comparison, the influence of the J_6 coefficient is substantially smaller, with an effect we quantify within 5 kilometers. Moreover, the effects of J_8, J_{10}, and J_{12} coefficients are minimal, contributing less than 1 kilometer to the overall shape. Regarding the odd zonal harmonics, J_3, J_5, J_7, and J_9, their combined effect is even smaller than that of J_8, indicating their relatively minor influence on Jupiter's shape.

Regarding the polar radius, the uncertainty currently assumed in literature is $\pm$ 10 km.
Our analysis found that the uncertainties in the polar radius produce a variation in the shape up to 12 km at the equator, and a variation in the dynamical height up to 6 meters.

To understand the effects due to the cloud-level winds, we ran the algorithm considering the zonal wind profiles presented in Section 3.3.2. We found that variations in the cloud-level winds produce an effect on the shape within 5 km prevalently in the mid-latitudes of the northern hemisphere. This effect is more pronounced for the measurements taken by Voyager 2, but the subsequent comparison between the RMSE of Voyager 2 and Hubble seems to exclude a lower precision of Voyager 2 measurements compared to those collected by Hubble and could genuinely be due to dynamic differences arising from Jupiter's atmosphere.

Jupiter's rotation rate has been determined with high accuracy, thanks to decades of ground-based observations. Its value is assumed to be 9 hr 55 min 29.71 s, although previous studies suggested that this value might be overestimated by 0.025 s. This claim does not find support from magnetic field data collected from the Galileo probe. Nevertheless, we opted to analyze the potential effect that a shift of 0.025 s in the rotation rate may have on the obtained shape of Jupiter. Our result shows that an eventual shift in the rotation rate of that entity would produce a variation in the dynamical height up to around 30 meters, hence it can be considered negligible.

The second part of our work involved comparing the overall shape with the results obtained from radio occultation measurements. We coded an algorithm that, by utilizing Matlab's fsolve() function, solves a nonlinear least squares problem to estimate a new polar radius to be used to update the shape in order to fit radio occultations. This problem incorporates the available occultation data, listed in Table 4.4, and the shape calculated in the initial part of our study, accounting for both gravitational and cloud-level wind effects. We then proceeded to analyze the uncertainties, addressing the effects arising from the gravitational harmonics and the zonal wind profile chosen for the computation. Regarding the gravitational harmonics, according to the results obtained in subsection 4.1.1, we focused on the J_2 and J_4 gravity coefficients only and found an effect on the shape within 1 meter, thus negligible. Considering the zonal winds, we found a contribution to the overall result within 5 km, which represents the uncertainty we propose regarding the dynamical height. Our estimation of Jupiter's polar radius at 100 mbar stands at 66,887 $\pm$ 10 km for the northern hemisphere and 66,890 $\pm$ 10 km for the southern hemisphere, respectively. These values are consistent with the result of 66,896 $\pm$ 5 km derived from radio occultations. Similarly, our estimation of the equatorial radius at 100 mbar is 71,542 $\pm$ 4.6 km, which closely aligns with the literature value of 71,541 $\pm$ 4 km. The slight difference between the two polar radii stems from the asymmetry of Jupiter's winds across the equator, leading to varying dynamical heights and consequently a minor fluctuation in the polar radius. Furthermore, four out of six pre-Juno radio occultation measurements now align consistently with the estimated dynamical height. The additional three Juno radio occultations are still at the preliminary stage and lack uncertainty estimates, but do not set too far from the calculated dynamical height, showing promising potential. The RMSE sets below 6 km, 3 km less than the one reported in recent literature. Results pertaining to the entire latitude window of the planet are listed in Appendix B.

5.1 Future assessments

In this study, we have been able to provide an updated estimate of the shape of Jupiter, incorporating the latest measurements in terms of gravity, radio occultations, and zonal wind profiles. Although the results obtained seem to better fit observational constraints compared to previous efforts, the uncertainties involved are still too significant. In particular, the uncertainty associated with the polar radius is comparable to that associated with radio occultation measurements and to the values characterizing the dynamical height. Matching Jupiter's calculated shape with radio occultations poses two primary challenges. Firstly, the accuracy of radio occultation radii may deviate from the reported uncertainty of $\pm$5 km. Despite advancements in shape knowledge since the Pioneer and Voyager missions, technical glitches and inherent uncertainties persist. Re-analyzing these radio occultations in the future may yield improved agreement with calculated shapes. Secondly, Jupiter's atmosphere between 100 mbar and 1 bar pressure levels may exhibit baroclinic behavior; in such a scenario, proper modifications to this analysis would be required. Fortunately, the Juno mission plans to conduct numerous radio occultation measurements, offering a promising opportunity to refine our understanding of Jupiter's shape and the underlying atmospheric dynamics.

Acknowledgements

Ringrazio il Professor Paolo Tortora, per la disponibilità e per avermi dato la possibilità di lavorare con il suo gruppo di ricerca a un progetto stimolante e in linea con la passione che mi anima fin da bambino.

Ringrazio Andrea Caruso, per avermi saputo accompagnare con professionalità e pazienza durante l'intero lavoro di tesi.

Dedico questa tesi:
Alla mia famiglia, per essermi sempre vicina e avermi permesso di intraprendere e portare a termine questo percorso.
A Valentina, per essermi stata sempre accanto e avere sempre creduto in me.
Alla memoria del mio amato cugino Filippo, con il quale tanto avrei condiviso di ció che studio.
A me stesso, che ho saputo trovare il coraggio e la determinazione per realizzare un traguardo così importante.

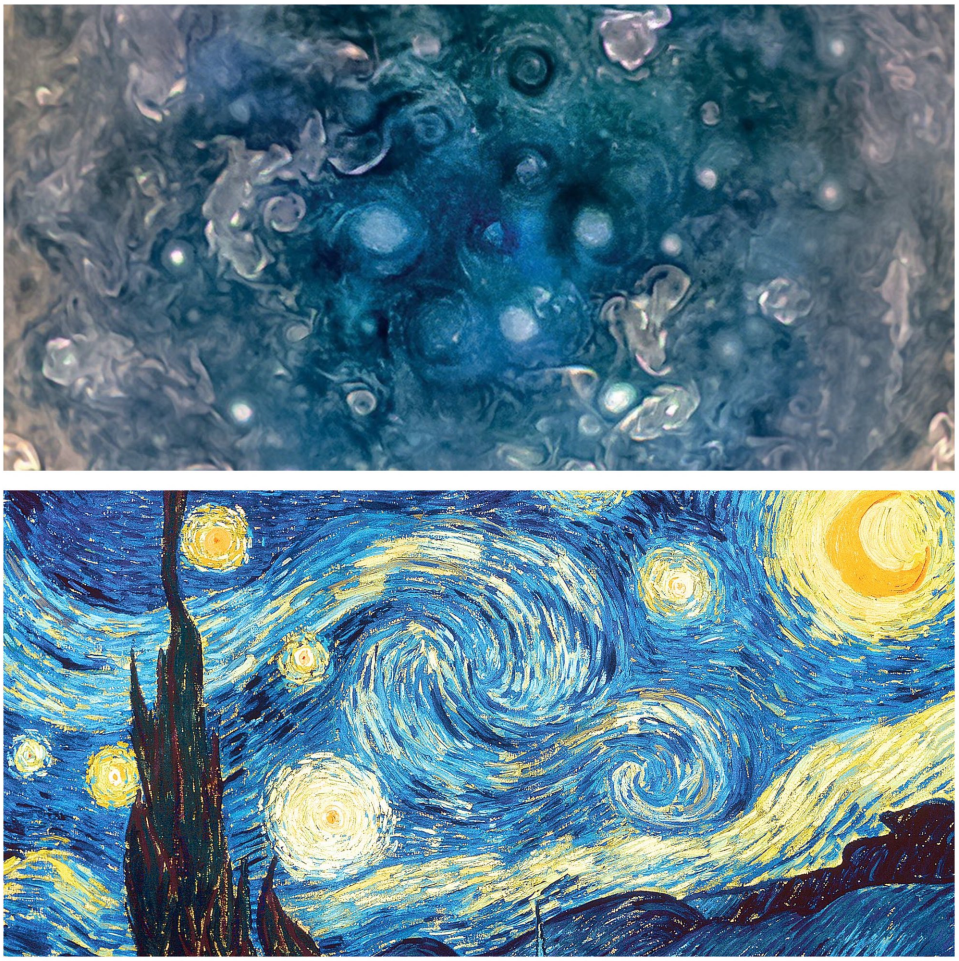

Figure 5.1. Jupiter's South Pole and Vincent Van Gogh Starry Night.

APPENDIX A

Derivation of the Taylor-Proudman Theorem

We present the derivation of the Taylor-Proudman Theorem based on the MIT's Lecture Notes on Fluid Dynamics available at this source.

Let us consider a steady rotating flow in a homogeneous fluid.
We now show that if the Rossby number is small then the flow is essentially two dimensional.
The momentum equation can be written as

$$2\boldsymbol{\Omega} \times \mathbf{q} = -\frac{\nabla p}{\rho} \tag{A.1}$$

which, by taking the curl of both sides, becomes

$$\nabla(\boldsymbol{\Omega} \times \mathbf{q}) = 0 \tag{A.2}$$

Given the identity

$$\nabla \times (\mathbf{A} \times \mathbf{B}) = \mathbf{A}\nabla \cdot \mathbf{B} - \mathbf{B}\nabla \cdot \mathbf{A} + \mathbf{B} \cdot \nabla \mathbf{A} - \mathbf{A} \cdot \nabla \mathbf{B} \tag{A.3}$$

Eq. (A.1) can be rewritten as

$$\boldsymbol{\Omega}\nabla \cdot \mathbf{q} - \mathbf{q}\nabla \cdot \boldsymbol{\Omega} + \mathbf{q} \cdot \nabla \boldsymbol{\Omega} - \boldsymbol{\Omega} \cdot \nabla \mathbf{q} = 0 \tag{A.4}$$

and by assuming continuity and consistency of Ω we get

$$\boldsymbol{\Omega} \cdot \nabla \mathbf{q} = 0 \tag{A.5}$$

hence the velocity field does not vary in the direction of Ω.

We now put

$$\zeta = \nabla \times \mathbf{q} \tag{A.6}$$

and consider the identity

$$\zeta \times \mathbf{q} = \mathbf{q} \cdot \nabla \mathbf{q} - \nabla \left(\frac{|\mathbf{q}|^2}{2} \right). \tag{A.7}$$

The momentum equation can be written as

$$\frac{\partial \mathbf{q}}{\partial t} + \zeta \times \mathbf{q} + 2\boldsymbol{\Omega} \times \mathbf{q} = -\frac{\nabla p}{\rho} + \nabla \left(\phi - \frac{|\mathbf{q}|^2}{2} \right) \tag{A.8}$$

which by taking the curl and using identity (A.3) becomes

$$\nabla \times [(2\boldsymbol{\Omega} + \zeta) \times \mathbf{q}] = -\mathbf{q} \nabla \cdot (2\boldsymbol{\Omega} + \zeta) + (2\boldsymbol{\Omega} + \zeta) \nabla \cdot \mathbf{q} + \mathbf{q} \cdot \nabla (2\boldsymbol{\Omega} + \zeta) - (2\boldsymbol{\Omega} + \zeta) \cdot \nabla \mathbf{q} \tag{A.9}$$

where both terms on the right-hand side vanish because Ω is constant, resulting in a zero divergence of the curl, and because the fluid is assumed to be incompressible, respectively.

By now defining *absolute vorticity* the quantity

$$\zeta_a = \zeta + 2\boldsymbol{\Omega} \tag{A.10}$$

we obtain

$$\frac{D\zeta}{Dt} = \frac{\partial \zeta}{\partial t} + \mathbf{q} \cdot \nabla \zeta = \zeta_a \cdot \nabla \mathbf{q} + \frac{\nabla \rho \times \nabla p}{\rho^2}. \tag{A.11}$$

In a fluid of constant density and steady flow, the Rossby number

$$Ro = \frac{u}{2\Omega L} << 1 \tag{A.12}$$

hence

$$\frac{\zeta}{2\Omega} \approx \frac{u}{2\Omega L} << 1 \tag{A.13}$$

and Eq. A.11 reduces to Eq. A.5, which represents the Taylor-Proudman Theorem.

APPENDIX B

Our Results

In Table B.12, the reader can find our results regarding Jupiter's shape and dynamical height. The first column lists the planetocentric latitudes in degrees. The second column lists the overall shape in kilometers, including both the effects of the gravitational coefficients and the zonal winds. The third column lists the dynamical heights in kilometers. The fourth column lists the considered zonal wind profile with the associated RMSE, in meters per second. The fifth column lists the gravity acceleration at 100 mbar, computed using the equation in Lindal, Sweetnam, and V. Eshleman (1985):

$$\sqrt{g_r^2 + g_\phi^2} \tag{B.1}$$

with g_r and g_ϕ defined as in Eq. (3.3) and (3.4).

For improved visualization, we present the results using a latitude bin of 0.5°in the interval $[90° \leq \phi \leq 4°] \cup [-4° \geq \phi \geq -90°]$, and of 0.25°in the interval $[4° \geq \phi \geq -4°]$, where the effect of the zonal winds is more prominent. We also highlighted some reference points, in particular:

- The equatorial latitude, has been marked in green;
- The Great Red Spot's latitude, has been marked in orange;
- The 24°N prograde jet, has been marked in cyan.

corresponding to the positions indicated in the map below

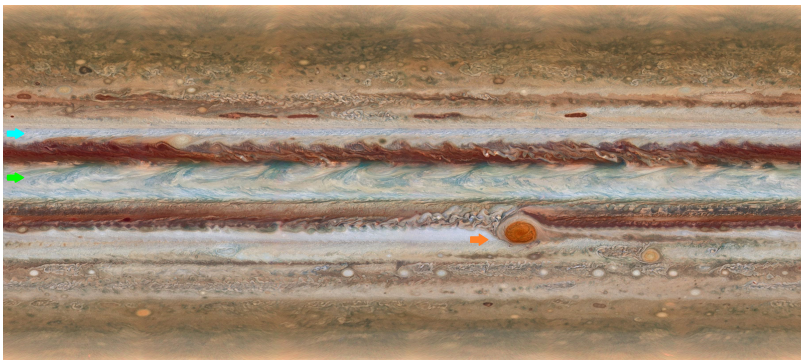

Latitude (deg)	Shape (km)	Dynamical Height (km)	v eastward (m s^{-1})	g (m s^{-2})
90.00	6.688987×10^4	2.61	0	27.0
89.50	6.689018×10^4	2.61	0	26.99
89.00	6.689112×10^4	2.61	0	26.99
88.50	6.689268×10^4	2.61	0	26.99
88.00	6.689486×10^4	2.61	0	26.99
87.50	6.689766×10^4	2.61	0	26.98
87.00	6.690109×10^4	2.61	0	26.98
86.50	6.690514×10^4	2.61	0	26.98
86.00	6.690981×10^4	2.61	0	26.97
85.50	6.6915010×10^4	2.61	0	26.97
85.00	6.692100×10^4	2.61	0	26.96
84.50	6.692753×10^4	2.61	0	26.96
84.00	6.693467×10^4	2.61	0	26.95
83.50	6.694243×10^4	2.61	0	26.95
83.00	6.695079×10^4	2.61	0	26.94
82.50	6.695977×10^4	2.61	0	26.93
82.00	6.696936×10^4	2.61	0	26.92
81.50	6.697956×10^4	2.61	0	26.92
81.00	6.699036×10^4	2.61	0	26.91
80.50	6.700177×10^4	2.61	0	26.90
80.00	6.701377×10^4	2.61	0	26.89
79.50	6.702638×10^4	2.61	0	26.88
79.00	6.703958×10^4	2.61	0	26.87
78.50	6.705338×10^4	2.61	0	26.86
78.00	6.706776×10^4	2.61	0	26.84
77.50	6.708273×10^4	2.61	0	26.83
77.00	6.709829×10^4	2.61	0	26.82
76.50	6.711443×10^4	2.60	0	26.81
76.00	6.713114×10^4	2.60	0	26.79
75.50	6.714843×10^4	2.60	0	26.78
75.00	6.716629×10^4	2.60	0	26.76

Table B.1: Our results.

Latitude (deg)	Shape (km)	Dynamical Height (km)	v eastward (m s^{-1})	g (m s^{-2})
74.50	6.718471×10^4	2.60	0	26.75
74.00	6.720370×10^4	2.60	0	26.73
73.50	6.722325×10^4	2.60	0	26.72
73.00	6.724335×10^4	2.60	0	26.70
72.50	6.726400×10^4	2.60	0	26.68
72.00	6.728520×10^4	2.60	0	26.67
71.50	6.730694×10^4	2.60	0	26.65
71.00	6.732922×10^4	2.60	0	26.63
70.50	6.735203×10^4	2.60	0	26.61
70.00	6.737536×10^4	2.61	0	26.59
69.50	6.739927×10^4	2.66	0	26.57
69.00	6.742364×10^4	2.66	0	26.55
68.50	6.744856×10^4	2.70	0	26.53
68.00	6.747407×10^4	2.81	0	26.51
67.50	6.750013×10^4	2.99	0	26.49
67.00	6.752676×10^4	3.23	14.2 ± 8.12	26.47
66.50	6.755390×10^4	3.50	11.8 ± 7.68	26.44
66.00	6.758145×10^4	3.70	10.2 ± 7.49	26.42
65.50	6.760942×10^4	3.84	9.74 ± 7.69	26.40
65.00	6.763783×10^4	3.96	1.45 ± 7.26	26.38
64.50	6.766667×10^4	4.03	26.1 ± 7.16	26.35
64.00	6.769591×10^4	4.06	26.7 ± 6.39	26.33
63.50	6.772561×10^4	4.09	17.2 ± 5.95	26.31
63.00	6.775576×10^4	4.13	18.7 ± 5.48	26.28
62.50	6.778634×10^4	4.17	-2.99 ± 5.33	26.26
62.00	6.781740×10^4	4.25	-7.95 ± 5.02	26.23
61.50	6.784892×10^4	4.38	-5.20 ± 5.37	26.20
61.00	6.788085×10^4	4.51	-5.67 ± 5.32	26.18
60.50	6.791315×10^4	4.60	-5.79 ± 5.52	26.15
60.00	6.794582×10^4	4.65	-5.94 ± 5.62	26.13

Table B.2: Our results.

Latitude (deg)	Shape (km)	Dynamical Height (km)	v eastward (m s^{-1})	g (m s^{-2})
59.50	6.797883×10^4	4.66	-5.07 ± 5.80	26.10
59.00	6.801220×10^4	4.65	-5.02 ± 6.00	26.07
58.50	6.804593×10^4	4.62	-6.44 ± 6.50	26.04
58.00	6.808001×10^4	4.58	-3.78 ± 6.50	26.02
57.50	6.811445×10^4	4.54	2.13 ± 6.60	25.99
57.00	6.814924×10^4	4.49	7.30 ± 6.45	25.96
56.50	6.818434×10^4	4.43	1.85 ± 6.49	25.93
56.00	6.821978×10^4	4.37	2.30 ± 6.22	25.90
55.50	6.825555×10^4	4.31	1.96 ± 6.16	25.87
55.00	6.829167×10^4	4.30	1.24 ± 5.94	25.84
54.50	6.832817×10^4	4.36	6.12 ± 5.96	25.81
54.00	6.836502×10^4	4.48	1.93 ± 5.76	25.78
53.50	6.840221×10^4	4.65	-3.17 ± 5.42	25.74
53.00	6.843974×10^4	4.89	-5.67 ± 5.30	25.71
52.50	6.847757×10^4	5.16	-5.18 ± 5.51	25.68
52.00	6.851562×10^4	5.41	-5.86 ± 5.44	25.65
51.50	6.855389×10^4	5.62	-5.39 ± 5.60	25.62
51.00	6.859229×10^4	5.73	-3.43 ± 5.43	25.59
50.50	6.863085×10^4	5.78	-2.35 ± 5.58	25.56
50.00	6.866958×10^4	5.78	-3.46 ± 5.46	25.53
49.50	6.870848×10^4	5.74	-2.95 ± 5.60	25.50
49.00	6.874753×10^4	5.68	-1.21 ± 5.51	25.47
48.50	6.878675×10^4	5.59	2.35 ± 5.68	25.44
48.00	6.882611×10^4	5.48	6.83 ± 5.44	25.40
47.50	6.886565×10^4	5.38	1.53 ± 5.68	25.37
47.00	6.890538×10^4	5.33	1.88 ± 5.57	25.33
46.50	6.894529×10^4	5.32	1.35 ± 5.62	25.30
46.00	6.898538×10^4	5.38	6.05 ± 5.36	25.26
45.50	6.902566×10^4	5.49	3.47 ± 5.48	25.23
45.00	6.906606×10^4	5.64	1.92 ± 5.41	25.19
44.50	6.910659×10^4	5.82	2.49 ± 5.66	25.16
44.00	6.914722×10^4	6.02	4.31 ± 5.35	25.12

Table B.3: Our results.

Latitude (deg)	Shape (km)	Dynamical Height (km)	v eastward (m s^{-1})	g (m s^{-2})
43.50	6.918795×10^4	6.26	9.90 ± 5.56	25.09
43.00	6.922874×10^4	6.51	18.8 ± 5.57	25.06
42.50	6.926954×10^4	6.71	18.2 ± 5.91	25.02
42.00	6.931029×10^4	6.85	8.87 ± 6.06	24.99
41.50	6.935101×10^4	6.94	3.79 ± 6.80	24.96
41.00	6.939171×10^4	7.0	-6.43 ± 7.07	24.93
40.50	6.943238×10^4	7.04	-12.2 ± 7.02	24.89
40.00	6.947301×10^4	7.06	-15.7 ± 6.89	24.86
39.50	6.951357×10^4	7.05	-17.8 ± 6.78	24.83
39.00	6.955407×10^4	7.03	-20.7 ± 7.00	24.79
38.50	6.959454×10^4	7.02	-11.8 ± 7.33	24.76
38.00	6.963499×10^4	7.08	$(5.88 \times 10^{-1}) \pm 7.39$	24.72
37.50	6.967541×10^4	7.18	12.0 ± 7.11	24.69
37.00	6.971577×10^4	7.34	17.8 ± 6.78	24.65
36.50	6.975604×10^4	7.51	25.2 ± 6.80	24.62
36.00	6.979627×10^4	7.76	25.4 ± 6.77	24.58
35.50	6.983638×10^4	8.04	29.5 ± 7.03	24.54
35.00	6.987828×10^4	8.27	31.5 ± 6.93	24.51
34.50	6.991792×10^4	8.40	30.6 ± 6.64	24.48
34.00	6.995731×10^4	8.46	23.2 ± 6.13	24.45
33.50	6.999646×10^4	8.47	10.0 ± 5.74	24.42
33.00	7.003536×10^4	8.43	-2.0 ± 5.87	24.39
32.50	7.007401×10^4	8.36	-15.1 ± 6.18	24.36
32.00	7.011242×10^4	8.29	-24.2 ± 6.54	24.33
31.50	7.015059×10^4	8.22	-30.0 ± 6.92	24.30
31.00	7.018853×10^4	8.19	-33.3 ± 7.04	24.26
30.50	7.022624×10^4	8.18	-25.9 ± 7.01	24.23
30.00	7.026368×10^4	8.21	-14.7 ± 6.64	24.20
29.50	7.030087×10^4	8.27	-2.67 ± 6.25	24.16
29.00	7.033777×10^4	8.37	7.94 ± 5.54	24.13
28.50	7.037439×10^4	8.50	18.5 ± 5.33	24.10
28.00	7.041068×10^4	8.66	24.8 ± 5.12	24.06

Table B.4: Our results.

Latitude (deg)	Shape (km)	Dynamical Height (km)	v eastward (m s^{-1})	g (m s^{-2})
27.50	7.044663×10^4	8.82	28.2 ± 5.14	24.03
27.00	7.048223×10^4	8.99	33.1 ± 4.93	24.00
26.50	7.051746×10^4	9.17	44.0 ± 4.75	23.97
26.00	7.055229×10^4	9.35	57.9 ± 4.51	23.94
25.50	7.058671×10^4	9.53	76.6 ± 5.19	23.91
25.00	7.062070×10^4	9.68	101.0 ± 5.38	23.89
24.50	7.065421×10^4	9.80	126.0 ± 4.39	23.86
24.00	7.068724×10^4	9.86	150.0 ± 4.44	23.84
23.50	7.071976×10^4	9.89	149.0 ± 4.93	23.81
23.00	7.075177×10^4	9.87	138.0 ± 4.83	23.79
22.50	7.078328×10^4	9.83	125.0 ± 4.87	23.77
22.00	7.081579×10^4	9.74	108.0 ± 4.66	23.74
21.50	7.084620×10^4	9.62	84.6 ± 4.77	23.72
21.00	7.087607×10^4	9.48	62.9 ± 5.13	23.70
20.50	7.090538×10^4	9.32	43.4 ± 5.64	23.67
20.00	7.093414×10^4	9.13	22.3 ± 5.88	23.65
19.50	7.096374×10^4	8.94	9.01 ± 6.53	23.62
19.00	7.099136×10^4	8.77	-1.89 ± 6.47	23.60
18.50	7.101843×10^4	8.62	-10.3 ± 6.72	23.58
18.00	7.104493×10^4	8.49	-16.6 ± 6.81	23.55
17.50	7.107087×10^4	8.40	-21.5 ± 6.56	23.52
17.00	7.109623×10^4	8.33	-22.4 ± 6.15	23.50
16.50	7.112101×10^4	8.31	-20.0 ± 6.08	23.48
16.00	7.114518×10^4	8.30	-14.6 ± 5.73	23.45
15.50	7.116874×10^4	8.32	-7.57 ± 5.67	23.43
15.00	7.119167×10^4	8.36	-5.38 ± 5.71	23.41
14.50	7.121396×10^4	8.42	7.81 ± 5.98	23.39
14.00	7.123559×10^4	8.49	7.40 ± 5.67	23.37
13.50	7.125655×10^4	8.55	17.2 ± 5.88	23.35
13.00	7.127682×10^4	8.62	27.9 ± 6.32	23.33
12.50	7.129641×10^4	8.70	41.2 ± 6.91	23.31
12.00	7.131530×10^4	8.78	52.6 ± 6.96	23.30

Table B.5: Our results.

Latitude (deg)	Shape (km)	Dynamical Height (km)	v eastward (m s^{-1})	g (m s^{-2})
11.50	7.133348×10^4	8.87	59.4 ± 7.05	23.28
11.00	7.135095×10^4	8.96	65.9 ± 6.95	23.26
10.50	7.136770×10^4	9.05	79.1 ± 7.34	23.25
10.00	7.138293×10^4	9.13	89.4 ± 7.47	23.23
9.50	7.139826×10^4	9.23	98.0 ± 7.97	23.22
9.00	7.141287×10^4	9.37	99.4 ± 8.32	23.19
8.50	7.142678×10^4	9.55	97.5 ± 8.69	23.17
8.00	7.143995×10^4	9.75	101.0 ± 8.86	23.15
7.50	7.145237×10^4	9.96	108.0 ± 9.31	23.14
7.00	7.146401×10^4	10.16	110.0 ± 9.99	23.13
6.50	7.147485×10^4	10.34	108.0 ± 11.0	23.13
6.00	7.148489×10^4	10.49	104.0 ± 11.8	23.13
5.50	7.149413×10^4	10.62	102.0 ± 12.2	23.12
5.00	7.150255×10^4	10.72	95.2 ± 12.1	23.11
4.50	7.151017×10^4	10.81	94.0 ± 11.8	23.11
4.00	7.151699×10^4	10.88	93.2 ± 11.6	23.11
3.75	7.152009×10^4	10.91	89.6 ± 11.5	23.11
3.50	7.152299×10^4	10.94	88.2 ± 11.4	23.10
3.25	7.152569×10^4	10.97	87.1 ± 11.1	23.10
3.00	7.152819×10^4	10.99	87.0 ± 10.8	23.10
2.75	7.153048×10^4	11.01	89.3 ± 10.8	23.10
2.50	7.153258×10^4	11.03	88.2 ± 10.9	23.10
2.25	7.153447×10^4	11.05	84.7 ± 11.1	23.10
2.00	7.153615×10^4	11.06	79.0 ± 10.9	23.09
1.75	7.153764×10^4	11.08	80.1 ± 10.7	23.09
1.50	7.153892×10^4	11.09	79.4 ± 10.8	23.09
1.25	7.153999×10^4	1.11	77.4 ± 10.7	23.09
1.00	7.154087×10^4	11.10	70.7 ± 10.7	23.09
0.75	7.154154×10^4	11.11	69.2 ± 10.7	23.09
0.50	7.154201×10^4	11.11	74.0 ± 10.6	23.09
0.25	7.154227×10^4	1.11	75.8 ± 10.6	23.09
0.00	7.154233×10^4	1.11	72.4 ± 10.7	23.09

Table B.6: Our results.

Latitude (deg)	Shape (km)	Dynamical Height (km)	v eastward (m s^{-1})	g (m s^{-2})
0.00	7.154233×10^4	1.11	72.4 ± 10.7	23.09
-0.25	7.154219×10^4	11.11	71.6 ± 10.9	23.09
-0.50	7.154185×10^4	11.11	70.0 ± 10.8	23.09
-0.75	7.154130×10^4	11.11	71.1 ± 10.7	23.09
-1.00	7.154054×10^4	11.10	71.5 ± 10.3	23.09
-1.25	7.153959×10^4	11.09	70.7 ± 9.98	23.09
-1.50	7.153843×10^4	11.08	68.9 ± 9.76	23.09
-1.75	7.153707×10^4	11.07	72.6 ± 9.62	23.09
-2.00	7.153550×10^4	11.05	73.2 ± 9.30	23.09
-2.25	7.153373×10^4	11.03	73.1 ± 9.01	23.09
-2.50	7.153176×10^4	11.01	75.7 ± 8.96	23.09
-2.75	7.152958×10^4	10.99	77.2 ± 9.05	23.09
-3.00	7.152720×10^4	10.96	77.3 ± 9.07	23.10
-3.25	7.152462×10^4	10.94	78.7 ± 9.01	23.10
-3.50	7.152184×10^4	10.91	81.4 ± 9.07	23.10
-3.75	7.151885×10^4	10.87	82.8 ± 9.12	23.10
-4.00	7.151567×10^4	10.84	86.0 ± 9.05	23.10
-4.50	7.150869×10^4	10.76	91.1 ± 9.05	23.11
-5.00	7.150091×10^4	10.67	99.7 ± 7.90	23.12
-5.50	7.149233×10^4	10.57	111.0 ± 7.34	23.12
-6.00	7.148295×10^4	10.45	122.0 ± 6.87	23.13
-6.50	7.147277×10^4	10.32	133.0 ± 6.64	23.13
-7.00	7.146180×10^4	10.17	141.0 ± 6.35	23.14
-7.50	7.145005×10^4	10.01	144.0 ± 6.12	23.15
-8.00	7.143753×10^4	9.85	135.0 ± 5.98	23.17
-8.50	7.142425×10^4	9.69	117.0 ± 6.09	23.18
-9.00	7.141020×10^4	9.52	88.4 ± 6.18	23.19
-9.50	7.139539×10^4	9.35	61.4 ± 6.56	23.20
-10.00	7.137985×10^4	9.17	47.5 ± 7.22	23.22
-10.50	7.136274×10^4	8.99	45.6 ± 7.88	23.24
-11.00	7.134571×10^4	8.85	41.5 ± 8.22	23.26
-11.50	7.132798×10^4	8.71	38.1 ± 8.36	23.28

Table B.7: Our results.

Latitude (deg)	Shape (km)	Dynamical Height (km)	v eastward (m s^{-1})	g (m s^{-2})
-12.00	7.130954×10^4	8.58	35.6 ± 8.24	23.29
-12.50	7.129041×10^4	8.47	32.6 ± 8.17	23.31
-13.00	7.127061×10^4	8.39	27.3 ± 8.17	23.34
-13.50	7.125014×10^4	8.33	24.0 ± 8.35	23.36
-14.00	7.122902×10^4	8.30	24.1 ± 8.20	23.38
-14.50	7.120724×10^4	8.28	22.8 ± 8.09	23.40
-15.00	7.118480×10^4	8.28	17.7 ± 9.12	23.42
-15.50	7.116172×10^4	8.29	4.28 ± 8.02	23.44
-16.00	7.113802×10^4	8.31	-3.21 ± 7.24	23.46
-16.50	7.111370×10^4	8.36	-6.65 ± 6.83	23.48
-17.00	7.108876×10^4	8.42	-20.8 ± 6.46	23.51
-17.50	7.106322×10^4	8.48	-27.5 ± 5.99	23.53
-18.00	7.103705×10^4	8.54	-38.9 ± 5.96	23.55
-18.50	7.101028×10^4	8.57	-45.2 ± 5.89	23.57
-19.00	7.098290×10^4	8.58	-47.5 ± 5.87	23.59
-19.50	7.095491×10^4	8.55	-53.0 ± 6.08	23.61
-20.00	7.092776×10^4	8.49	-54.0 ± 6.37	23.63
-20.50	7.089857×10^4	8.36	-50.6 ± 6.67	23.65
-21.00	7.086878×10^4	8.15	-42.1 ± 7.03	23.66
-21.50	7.083837×10^4	7.85	-34.6 ± 7.99	23.68
-22.00	7.080735×10^4	7.46	-28.3 ± 7.84	23.70
-22.50	7.077733×10^4	7.01	-17.1 ± 7.99	23.72
-23.00	7.074520×10^4	6.48	-10.7 ± 8.23	23.75
-23.50	7.071252×10^4	5.88	-1.57 ± 7.98	23.77
-24.00	7.067933×10^4	5.24	9.02 ± 7.40	23.80
-24.50	7.064574×10^4	4.65	18.3 ± 6.36	23.84
-25.00	7.061181×10^4	4.17	31.9 ± 5.64	23.87
-25.50	7.057756×10^4	3.79	37.7 ± 5.40	23.91
-26.00	7.054297×10^4	3.49	40.1 ± 5.17	23.94
-26.50	7.050806×10^4	3.27	38.4 ± 5.82	23.98
-27.00	7.047280×10^4	3.09	38.7 ± 5.54	24.01
-27.50	7.043720×10^4	2.96	34.3 ± 5.94	24.04

Table B.8: Our results.

Latitude (deg)	Shape (km)	Dynamical Height (km)	v eastward (m s^{-1})	g (m s^{-2})
-28.00	7.040125×10^4	2.83	32.9 ± 6.41	24.07
-28.50	7.036497×10^4	2.73	28.9 ± 6.75	24.11
-29.00	7.032838×10^4	2.66	21.7 ± 6.60	24.14
-29.50	7.029153×10^4	2.64	15.6 ± 6.68	24.17
-30.00	7.025441×10^4	2.68	6.82 ± 6.45	24.21
-30.50	7.021707×10^4	2.78	1.25 ± 6.21	24.24
-31.00	7.017948×10^4	2.93	-5.29 ± 6.11	24.28
-31.50	7.014163×10^4	3.09	-11.2 ± 6.34	24.31
-32.00	7.010351×10^4	3.27	-17.1 ± 6.38	24.34
-32.50	7.006509×10^4	3.32	-16.0 ± 6.17	24.37
-33.00	7.002639×10^4	3.36	-11.8 ± 5.97	24.40
-33.50	6.998741×10^4	3.34	-4.01 ± 5.75	24.43
-34.00	6.994815×10^4	3.24	4.90 ± 5.65	24.45
-34.50	6.990864×10^4	3.08	15.9 ± 5.43	24.49
-35.00	6.986894×10^4	2.90	31.4 ± 5.70	24.52
-35.50	6.983107×10^4	2.73	46.6 ± 5.89	24.55
-36.00	6.979107×10^4	2.58	47.4 ± 5.57	24.59
-36.50	6.975096×10^4	2.43	33.4 ± 5.52	24.62
-37.00	6.971073×10^4	2.31	26.2 ± 5.51	24.66
-37.50	6.967043×10^4	2.22	21.5 ± 5.41	24.69
-38.00	6.963008×10^4	2.18	12.8 ± 5.28	24.73
-38.50	6.958971×10^4	2.21	2.84 ± 5.37	24.76
-39.00	6.954935×10^4	2.31	-3.57 ± 5.49	24.80
-39.50	6.950893×10^4	2.42	-5.01 ± 5.47	24.83
-40.00	6.946844×10^4	2.50	3.57 ± 5.47	24.87
-40.50	6.942791×10^4	2.58	3.97 ± 5.70	24.90
-41.00	6.938733×10^4	2.63	7.24 ± 5.72	24.93
-41.50	6.934670×10^4	2.64	10.9 ± 5.32	24.96
-42.00	6.930603×10^4	2.60	16.4 ± 4.79	25.0
-42.50	6.926533×10^4	2.51	27.1 ± 4.70	25.03
-43.00	6.922462×10^4	2.39	37.1 ± 5.03	25.06
-43.50	6.918399×10^4	2.30	39.4 ± 5.64	25.10

Table B.9: Our results.

Latitude (deg)	Shape (km)	Dynamical Height (km)	v eastward (m s^{-1})	g (m s^{-2})
-44.00	6.914345×10^4	2.26	34.0 ± 5.86	25.13
-44.50	6.910300×10^4	2.23	5.76 ± 5.76	25.17
-45.00	6.906264×10^4	2.22	5.65 ± 5.65	25.20
-45.50	6.902236×10^4	2.20	5.76 ± 5.76	25.23
-46.00	6.898218×10^4	2.17	5.74 ± 5.74	25.27
-46.50	6.894207×10^4	2.10	5.76 ± 5.76	25.30
-47.00	6.890204×10^4	1.99	5.87 ± 5.87	25.33
-47.50	6.886214×10^4	1.88	6.03 ± 6.03	25.36
-48.00	6.882244×10^4	1.80	6.09 ± 6.09	25.40
-48.50	6.878293×10^4	1.77	6.20 ± 6.20	25.43
-49.00	6.874362×10^4	1.77	6.45 ± 6.45	25.47
-49.50	6.8704514×10^4	1.78	-8.28 ± 6.57	25.50
-50.00	6.866560×10^4	1.80	-3.34 ± 6.46	25.53
-50.50	6.862689×10^4	1.81	3.00 ± 6.01	25.56
-51.00	6.858839×10^4	1.83	9.89 ± 5.79	25.60
-51.50	6.855013×10^4	1.86	24.9 ± 6.36	25.63
-52.00	6.851211×10^4	1.90	34.7 ± 6.70	25.66
-52.50	6.847434×10^4	1.93	36.0 ± 7.00	25.69
-53.00	6.843682×10^4	1.97	39.5 ± 7.07	25.72
-53.50	6.839956×10^4	2.0	31.4 ± 7.28	25.75
-54.00	6.836255×10^4	2.0	18.5 ± 7.16	25.78
-54.50	6.832578×10^4	1.97	11.1 ± 6.99	25.81
-55.00	6.828928×10^4	1.90	4.26 ± 6.44	25.84
-55.50	6.825302×10^4	1.79	-5.30 ± 6.15	25.87
-56.00	6.821705×10^4	1.63	-9.19 ± 5.85	25.90
-56.50	6.818140×10^4	1.49	-9.57 ± 5.63	25.93
-57.00	6.814614×10^4	1.39	-8.76 ± 5.51	25.96
-57.50	6.811128×10^4	1.36	-5.99 ± 5.61	25.99
-58.00	6.807681×10^4	1.37	-6.19 ± 5.44	26.02
-58.50	6.804272×10^4	1.40	-5.25 ± 5.20	26.05
-59.00	6.80090×10^4	1.44	-2.95 ± 5.03	26.07
-59.50	6.797565×10^4	1.48	-46.3 ± 4.99	26.10

Table B.10: Our results.

Latitude (deg)	Shape (km)	Dynamical Height (km)	v eastward (m s^{-1})	g (m s^{-2})
-60.00	6.794268×10^4	1.51	3.23 ± 5.03	26.13
-60.50	6.791012×10^4	1.56	8.87 ± 5.33	26.15
-61.00	6.787794×10^4	1.59	13.7 ± 5.45	26.18
-61.50	6.784617×10^4	1.63	18.6 ± 5.42	26.21
-62.00	6.781482×10^4	1.68	14.2 ± 5.50	26.23
-62.50	6.778389×10^4	1.72	7.73 ± 5.61	26.26
-63.00	6.775335×10^4	1.72	4.87 ± 5.75	26.28
-63.50	6.772321×10^4	1.69	4.36 ± 5.89	26.30
-64.00	6.769339×10^4	1.54	3.75 ± 6.01	26.33
-64.50	6.766397×10^4	1.34	6.00 ± 6.11	26.35
-65.00	6.763508×10^4	1.21	12.9 ± 6.13	26.38
-65.50	6.760670×10^4	1.12	16.9 ± 6.43	26.40
-66.00	6.757880×10^4	1.05	21.5 ± 6.84	26.42
-66.50	6.755136×10^4	9.64×10^{-1}	31.1 ± 7.32	26.45
-67.00	6.752440×10^4	8.68×10^{-1}	36.6 ± 7.82	26.47
-67.50	6.749788×10^4	7.35×10^{-1}	26.0 ± 14.2	26.49
-68.00	6.747181×10^4	5.55×10^{-1}	20.0	26.51
-68.50	6.744621×10^4	3.44×10^{-1}	9.70	26.53
-69.00	6.742114×10^4	1.55×10^{-1}	4.83	26.55
-69.50	6.739667×10^4	5.98×10^{-2}	-1.18	26.57
-70.00	6.737274×10^4	-1.49×10^{-2}	4.87	26.59
-70.50	6.734941×10^4	-1.64×10^{-2}	0	26.61
-71.00	6.732660×10^4	-1.66×10^{-2}	0	26.63
-71.50	6.730433×10^4	-1.67×10^{-2}	0	26.65
-72.00	6.728259×10^4	-1.67×10^{-2}	0	26.67
-72.50	6.726139×10^4	-1.67×10^{-2}	0	26.68
-73.00	6.724074×10^4	-1.67×10^{-2}	0	26.70
-73.50	6.722064×10^4	-1.65×10^{-2}	0	26.72
-74.00	6.720109×10^4	-1.64×10^{-2}	0	26.73
-74.50	6.718210×10^4	-1.62×10^{-2}	0	26.75

Table B.11: Our results.

Latitude (deg)	Shape (km)	Dynamical Height (km)	v eastward (m s^{-1})	g (m s^{-2})
-75.00	6.716368×10^4	-1.59×10^{-2}	0	26.76
-75.50	6.714582×10^4	-1.55×10^{-2}	0	26.78
-76.00	6.712853×10^4	-1.51×10^{-2}	0	26.79
-76.50	6.711181×10^4	-1.47×10^{-2}	0	26.81
-77.00	6.709568×10^4	-1.42×10^{-2}	0	26.82
-77.50	6.708012×10^4	-1.37×10^{-2}	0	26.83
-78.00	6.706515×10^4	-1.31×10^{-2}	0	26.84
-78.50	6.705077×10^4	-1.25×10^{-2}	0	26.86
-79.00	6.703697×10^4	-1.18×10^{-2}	0	26.87
-79.50	6.702377×10^4	-1.11×10^{-2}	0	26.88
-80.00	6.701117×10^4	-1.04×10^{-2}	0	26.89
-80.50	6.699916×10^4	-9.69×10^{-3}	0	26.90
-81.00	6.698776×10^4	-8.94×10^{-3}	0	26.91
-81.50	6.697696×10^4	-8.19×10^{-3}	0	26.92
-82.00	6.696676×10^4	-7.44×10^{-3}	0	26.93
-82.50	6.695717×10^4	-6.70×10^{-3}	0	26.93
-83.00	6.694819×10^4	-5.97×10^{-3}	0	26.94
-83.50	6.693983×10^4	-5.25×10^{-3}	0	26.95
-84.00	6.693207×10^4	-4.56×10^{-3}	0	26.95
-84.50	6.692493×10^4	-3.90×10^{-3}	0	26.96
-85.00	6.691841×10^4	-3.28×10^{-3}	0	26.96
-85.50	6.691250×10^4	-2.69×10^{-3}	0	26.97
-86.00	6.690721×10^4	-2.15×10^{-3}	0	26.97
-86.50	6.690254×10^4	-1.67×10^{-3}	0	26.98
-87.00	6.689850×10^4	-1.24×10^{-3}	0	26.98
-87.50	6.689507×10^4	-8.67×10^{-4}	0	26.98
-88.00	6.689226×10^4	-5.58×10^{-4}	0	26.99
-88.50	6.689008×10^4	-3.16×10^{-4}	0	26.99
-89.00	6.688852×10^4	-1.41×10^{-4}	0	26.99
-89.50	6.688759×10^4	-3.53×10^{-5}	0	26.99
-90.00	6.688728×10^4	0	0	27.0

Table B.12: Our results.

References

Atreya, SK et al. (2003). "Composition and origin of the atmosphere of Jupiter—an update, and implications for the extrasolar giant planets". In: *Planetary and Space Science* 51.2, pp. 105–112.

Bertotti, Bruno, Paolo Farinella, and David Vokrouhlicky (2012). *Physics of the solar system: dynamics and evolution, space physics, and spacetime structure*. Vol. 293. Springer Science & Business Media.

Buccino, Dustin R et al. (2020). "Updated equipotential shapes of Jupiter and Saturn using Juno and Cassini grand finale gravity science measurements". In: *Journal of Geophysical Research: Planets* 125.8, e2019JE006354.

Caruso, Andrea et al. (2023). "Analysis of the First Juno Radio Occultation Experiment of Jupiter's Atmosphere". In: *AGU23*.

Dessler, AJ (1983). "Coordinate systems". In: *Physics of the Jovian magnetosphere*, pp. 498–504.

Durante, D et al. (2020). "Jupiter's gravity field halfway through the Juno mission". In: *Geophysical Research Letters* 47.4, e2019GL086572.

Eshleman, Von R (1973). "The radio occultation method for the study of planetary atmospheres". In: *Planetary and Space Science* 21.9, pp. 1521–1531.

Evans, Scott et al. (2018). "MONTE: the next generation of mission design and navigation software". In: *CEAS Space Journal* 10, pp. 79–86.

Fimmel, Richard O, James Alfred Van Allen, and Eric Burgess (1980). *Pioneer, First to Jupiter, Saturn, and Beyond*. Vol. 446. Scientific, Technical Information Office, National Aeronautics, and Space ...

Fletcher, Leigh N et al. (2020). "Jupiter's equatorial plumes and hot spots: Spectral mapping from Gemini/TEXES and Juno/MWR". In: *Journal of Geophysical Research: Planets* 125.8, e2020JE006399.

Folkner, WM et al. (2017). "Jupiter gravity field estimated from the first two Juno orbits". In: *Geophysical Research Letters* 44.10, pp. 4694–4700.

Galanti, Eli, Hao Cao, and Yohai Kaspi (2017). "Constraining Jupiter's internal flows using Juno magnetic and gravity measurements". In: *Geophysical Research Letters* 44.16, pp. 8173–8181.

Galanti, Eli, Yohai Kaspi, and Tristan Guillot (2023). "The shape of Jupiter and Saturn based on atmospheric dynamics, radio occultations and gravity measurements". In: *Geophysical research letters* 50.6, e2022GL102321.

Guillot, Tristan et al. (2018). "A suppression of differential rotation in Jupiter's deep interior". In: *Nature* 555.7695, pp. 227–230.

Hansen, Candice J et al. (2004). "The Cassini–Huygens flyby of jupiter". In: *Icarus* 172.1, pp. 1–8.

Heimpel, Moritz, Jonathan Aurnou, and Johannes Wicht (2005). "Simulation of equatorial and high-latitude jets on Jupiter in a deep convection model". In: *Nature* 438.7065, pp. 193–196.

Higgins, Charles A et al. (1997). "A redefinition of Jupiter's rotation period". In: *Journal of Geophysical Research: Space Physics* 102.A10, pp. 22033–22041.

Hinson, David P et al. (1999). "Initial results from radio occultation measurements with Mars Global Surveyor". In: *Journal of Geophysical Research: Planets* 104.E11, pp. 26997–27012.

Hubbard, WB (1982). "Effects of differential rotation on the gravitational figures of Jupiter and Saturn". In: *Icarus* 52.3, pp. 509–515.

— (1999). "Gravitational signature of Jupiter's deep zonal flows". In: *Icarus* 137.2, pp. 357–359.

Hubbard, William B and B Militzer (2016). "A preliminary Jupiter model". In: *The Astrophysical Journal* 820.1, p. 80.

Iess, Luciano et al. (2018). "Measurement of Jupiter's asymmetric gravity field". In: *Nature* 555.7695, pp. 220–222.

Ingersoll, Andrew P and Jeffrey N Cuzzi (1969). "Dynamics of Jupiter's cloud bands". In: *Journal of Atmospheric Sciences* 26.5, pp. 981–985.

Ingersoll, Andrew P, Timothy E Dowling, et al. (2004). "Dynamics of Jupiter's atmosphere". In: *Jupiter: The planet, satellites and magnetosphere* 105.

Kaspi, Y ea et al. (2018). "Jupiter's atmospheric jet streams extend thousands of kilometres deep". In: *Nature* 555.7695, pp. 223–226.

Kaspi, Yohai (2013). "Inferring the depth of the zonal jets on Jupiter and Saturn from odd gravity harmonics". In: *Geophysical research letters* 40.4, pp. 676–680.

Kaspi, Yohai et al. (2010). "Gravitational signature of Jupiter's internal dynamics". In: *Geophysical research letters* 37.1.

Kliore, AJ et al. (2004). "Cassini radio science". In: *The cassini-huygens mission: Orbiter remote sensing investigations*, pp. 1–70.

Kliore, Arvydas et al. (1965). "Occultation experiment: Results of the first direct measurement of Mars's atmosphere and ionosphere". In: *Science* 149.3689, pp. 1243–1248.

Kong, Dali et al. (2018). "Origin of Jupiter's cloud-level zonal winds remains a puzzle even after Juno". In: *Proceedings of the National Academy of Sciences* 115.34, pp. 8499–8504.

Lanzano, Paolo (1974). "The equilibrium of a rotating body of arbitrary density". In: *Astrophysics and Space Science* 29, pp. 161–178.

Limaye, Sanjay S (1986). "Jupiter: New estimates of the mean zonal flow at the cloud level". In: *Icarus* 65.2-3, pp. 335–352.

Limaye, Sanjay S and Lawrence A Sromovsky (1991). "Winds of Neptune: Voyager observations of cloud motions". In: *Journal of Geophysical Research: Space Physics* 96.S01, pp. 18941–18960.

Lindal, Gunnar F, DN Sweetnam, and VR Eshleman (1985). "The atmosphere of Saturn-an analysis of the Voyager radio occultation measurements". In: *Astronomical Journal (ISSN 0004-6256), vol. 90, June 1985, p. 1136-1146. NASA-supported research.* 90, pp. 1136–1146.

Qin, Songhe et al. (2020). "Interpreting the equatorially antisymmetric gravitational field of Saturn measured by the Cassini Grand Finale". In: *The Astrophysical Journal* 890.1, p. 26.

Russell, CT, ZJ Yu, and MG Kivelson (2001). "The rotation period of Jupiter". In: *Geophysical research letters* 28.10, pp. 1911–1912.

Sanchez-Lavega, Agustin (2010). *An introduction to planetary atmospheres*. Taylor & Francis.

Sanders, Robert (2012). "Helium rain on Jupiter explains lack of neon in atmosphere". In: *University of Berkeley. Retrieved* 24.

Serra, Daniele et al. (2019). "A solution of Jupiter's gravitational field from Juno data with the ORBIT14 software". In: *Monthly Notices of the Royal Astronomical Society* 490.1, pp. 766–772.

Simon, Marvin K and Joseph H Yuen (1983). "Receiver design and performance characteristics". In: *Deep space telecommunications systems engineering*. Springer, pp. 49–121.

Smith, EJ, K-P Wenzel, and DE Page (1992). "Ulysses at Jupiter: An overview of the encounter". In: *Science* 257.5076, pp. 1503–1507.

Stern, S Alan (2009). "The New Horizons Pluto Kuiper belt mission: an overview with historical context". In: *New Horizons: Reconnaissance of the Pluto-Charon System and the Kuiper Belt*, pp. 3–21.

Strom, Robert G and NM Schneider (1982). "Volcanic eruption plumes on Io". In: *Satellites of Jupiter*, pp. 598–633.

Tinto, Massimo (2002). "Spacecraft radio occultations using multiple Doppler readouts". In: *Radio Science* 37.3, pp. 1–8.

Tollefson, Joshua et al. (2017). "Changes in Jupiter's Zonal Wind Profile preceding and during the Juno mission". In: *Icarus* 296, pp. 163–178.

Vasavada, Ashwin R and Adam P Showman (2005). "Jovian atmospheric dynamics: An update after Galileo and Cassini". In: *Reports on Progress in Physics* 68.8, p. 1935.

Von Zahn, U, DM Hunten, and G Lehmacher (1998). "Helium in Jupiter's atmosphere: Results from the Galileo probe helium interferometer experiment". In: *Journal of Geophysical Research: Planets* 103.E10, pp. 22815–22829.

Withers, Paul (2010). "Prediction of uncertainties in atmospheric properties measured by radio occultation experiments". In: *Advances in Space Research* 46.1, pp. 58–73.

Withers, Paul et al. (2014). "How to process radio occultation data: 1. From time series of frequency residuals to vertical profiles of atmospheric and ionospheric properties". In: *Planetary and Space Science* 101, pp. 77–88.

Wong, Michael H et al. (2020). "High-resolution UV/optical/IR imaging of Jupiter in 2016–2019". In: *The Astrophysical Journal Supplement Series* 247.2, p. 58.

Xiao, Z et al. (2009). "Physical mechanism of the inverse energy cascade of two-dimensional turbulence: a numerical investigation". In: *Journal of Fluid Mechanics* 619, pp. 1–44.